Study of Ferromagnetim in Nanostructured Nonmagnetic Inorganic Materials

A thesis submitted

in partial fulfillment for the degree of

Master of Science

as a part of the

Integrated Ph.D. Programme

(Materials Science)

by

Nitesh Kumar

Chemistry and Physics of Materials Unit

Jawaharlal Nehru Centre for Advanced Scientific Research

(A Deemed University)

Bangalore, India.

May 2010

Dedicated
to my family

DECLARATION

I hereby declare that the matter embodied in the thesis entitled "**Study of Ferromagnetim in Nanostructured Nonmagnetic Inorganic Materials**" is the result of investigations carried out by me at the Chemistry and Physics of Materials Unit, Jawaharlal Nehru Centre for Advanced Scientific Research, India under the supervision of Dr. A. Sunadersan and that it has not been submitted elsewhere for the award of any degree or diploma.

In keeping with the general practice in reporting the scientific observations, due acknowledgement has been made whenever the work described is based on the findings of other investigators. Any omission that might have occurred due to oversight or error in judgement is regretted.

Nitesh Kumar

CERTIFICATE

I hereby certify that the work described in this thesis entitled "**Study of Ferromagnetim in Nanostructured Nonmagnetic Inorganic Materials**" has been carried out by Mr. Nitesh Kumar under my supervision at the Chemistry and Physics of Materials Unit, Jawaharlal Nehru Centre for Advanced Scientific Research, India and that it has not been submitted elsewhere for the award of any degree or diploma.

Dr. A. Sundaresan

(Research Supervisor)

ACKNOWLEDGEMENT

I am very pleased to thank my research supervisor Dr. A. Sundaresan who gave an opportunity to work on the fascinating field of magnetism. His simple way of thinking about a problem always inspires me a lot. I shall remain ever thankful to him for giving me enough freedom to work on my own area of interests.

I thank our collaborator Prof. D. Sanyal for doing positron annihilation measurements.

I am very grateful to my labmates Dr. Vengadesh, Shipra, Pranab, Madhu, Sundarayya, Rana and all summer and POCE students for creating a wonderful working environment in the lab.

I especially thank Pranab and Shipra for their valuabe suggestions during my research work.

I shall be ever thankful to Prof. G. U. Kulkarni, Prof. S**.** Balasubramanian**,** Prof. A. Sundaresan, Prof. S. M. Shivaprasad, Prof. Chandrabhas Narayan, Dr. T. K. Maji, Dr. Eswaramoorthy, Prof. K. S. Narayan, Prof. S. K. Pati, Prof. U. V. Waghmare, Dr. S. Narasimhan, Dr. N. S. Vidhyadhiraja, Prof. S. Ranganathan (Materials Engineering, IISc), Prof. T. N. G. Rao (S. S. C. U, IISc.) for their valuable courses.

I thank all my batchmates of Int. Ph.D 2007 for their support during my MS programme.

PREFACE

This thesis consists of five chapters presenting magnetic properties of otherwise nonmagnetic inorganic nanomaterials which include nanoparticles, hollow spheres and doped nanoparticles.

Chapter 1 gives a brief introduction of magnetism and magnetic materials. It includes important concepts and theories of magnetism. A brief review of recent developments of magnetism in nanoparticles of nonmagnetic materials has been given.

Chapter 2 discusses the magnetic properties of MgO nanoparticles. Positron annihilation and photoluminescence spectroscopy were used to get the nature and concentration of defects. Effect of Li doping in the magnetic properties of MgO nanoparticles has also been studied.

Chapter 3 discusses about the ferromagnetic properties of inorganic hollow spheres of otherwise nonmagnetic materials. Magnetism in these hollow spheres has been compared with those of nanoparticles and thin films.

Chapter 4 contains the multiferroic properties of $Bi_4Ti_3O_{12}$ nanoparticles. The chapter discusses how a ferroelectric material can be made multiferroic by decreasing the size in nono range.

Chapter 5 presents the magnetic properties of CaF_2 nanoparticles. Ferromagnetic properties of CaF_2 nanoparticles prepared by two different methods have been compared.

Miscellaneous section describes the artefacts related to negative magnetization observed under zero field cooled conditions and the ways they can be avoided in the context of $CoCr_2O_4$. Negative magnetization in $CoCr_{2-x}Fe_xO_4$ ($0 \leq x \geq 1$) has been shown to due to negative trapped field in the sample space of superconducting magnet.

Table of Contents

MISCELLANEOUS: ***Negative magnetization in Zero Field Cooled (ZFC) Conditions: Is it Intrinsic?***

CHAPTER 1

Introduction to Magnetism and Magnetic Materials

Magnetic material in the form of magnetite (Fe_3O_4) has been known to mankind since centuries ago. It took almost 2400 years to understand the basic principles of magnetism and its application in our daily life. The rich physics and the wide range of applications which it entails still lure scientists to work in this field. Many theories have been put forward in order to explain the properties shown by different magnetic materials. In the last century several kinds of materials have been discovered showing interesting magnetic properties. It is interesting to note that almost all of them contain either transition metal or rare earth metal. A simple way to understand magnetism would be to understand first why transition metals or rare earth metals are required to impart magnetism to a material. Before addressing this question one must know the different kinds of magnetic materials known. Magnetic materials actually can be broadly divided into the following .

1.1 Types of Magnetic Materials:

1.1.1 Diamagnetic Materials:

When an atom has a closed shell electronic configuration then its spin and orbital moments orient in such a way that the net moment is zero. He, Ne, Ar, O_2, N_2, NaCl etc;

are all diamagnetic. In case of diatomic gases like O_2 and N_2, sharing of electrons results in closed shell for each atom. In the lattice, NaCl exists as Na^+ and Cl^-. So, NaCl as a whole is also diamagnetic. Actually diamagnetism is a property of all materials because they contain at least some electrons in the closed shell.

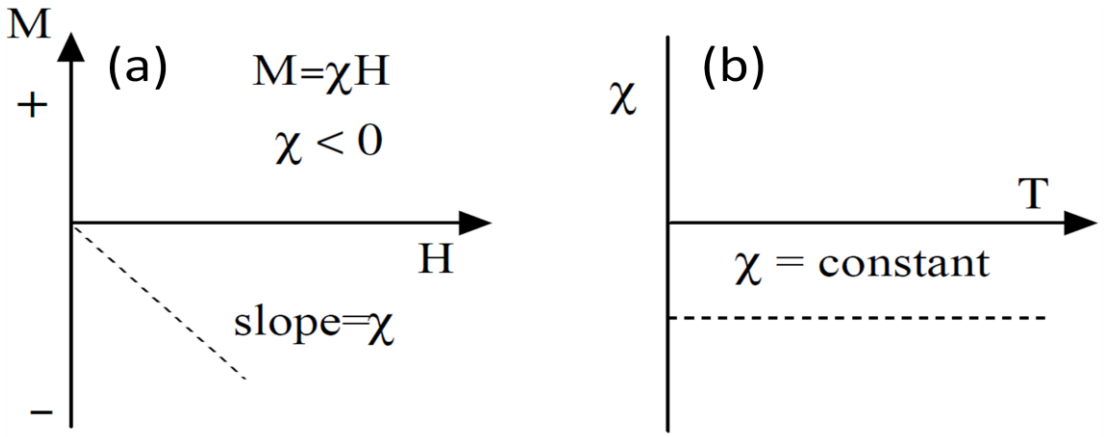

Figure 1(a) Dashed line shows variation of magnetization versus applied field, (b) variation of susceptibility with temperature for diamagnetic materials.

In the presence of magnetic field the planes of the orbitals are tipped slightly so that a net orbital moment is created in opposite direction to the applied magnetic field. Diamagnetism is independent of temperature.

1.1.2 Paramagnetic Materials:

An electron has two types of moments: the inherent spin moment and orbital moment resulting from the motion of the electron around the nucleus. Magnetic moment is expressed in units called Bohr magnetons (B. M.).

$$1\ \text{B. M.} = \frac{eh}{4\pi mc} \qquad \text{in CGS units}$$

$$1\ \text{B. M.} = \frac{eh}{4\pi m} \qquad \text{in SI units}$$

For a material to show paramagnetism it is necessary to have one or more unpaired electrons. In the paramagnetic state individual moments are independent to each

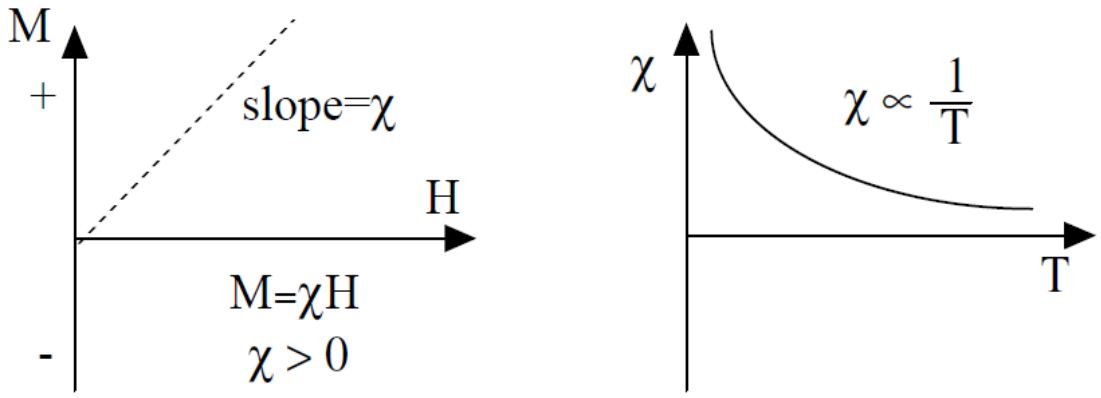

Figure 2(a) Variation of magnetization with applied field, (b) variation of susceptibility with temperature.

other and do not couple. Hence the moments are randomly oriented to give net zero magnetization in the absence of applied magnetic field. Most of the materials with unpaired electrons at very high temperature show paramagnetic behaviour because thermal energy doesn't allow individual moments to interact to each other.

In 1885, Pierre Cuire reported that in paramagnetic materials magnetic susceptibility varies inversely with temperature

$$\chi = \frac{C}{T}$$

This relation is called Curie law and C is called Curie constant. According to this relation for a paramagnetic material susceptibility versus temperature graph will always pass through origin but this is not always true. Later Weiss modified this relation to give a more general equation

$$\chi = \frac{C}{T - \theta}$$

This relation is called Curie-Weiss law and θ is called Weiss constant with the dimension of temperature. θ is zero for substances which obey Curie law but its value can be negative or positive for other paramagnetic materials depending on whether the molecular field applies in the same or in the opposite direction with respect to applied magnetic field.

1.1.3. Ferromagnetic materials:

Unlike paramagnetic materials, individual moments are not independent to each other. The moments are coupled by something called exchange forces. Exchange forces are very strong forces and are of the order of 1000 T, which produce spontaneous magnetization even in the absence of applied magnetic field.

The fact that net magnetization of a ferromagnetic material is zero in the absence of magnetic field led to the concept of magnetic domains. Magnetic domains are regions where all the moments are aligned in one direction. Figure 3 explains nicely how domains expand due to domain wall movement in the presence of applied magnetic field and eventually get magnetized in the same direction.

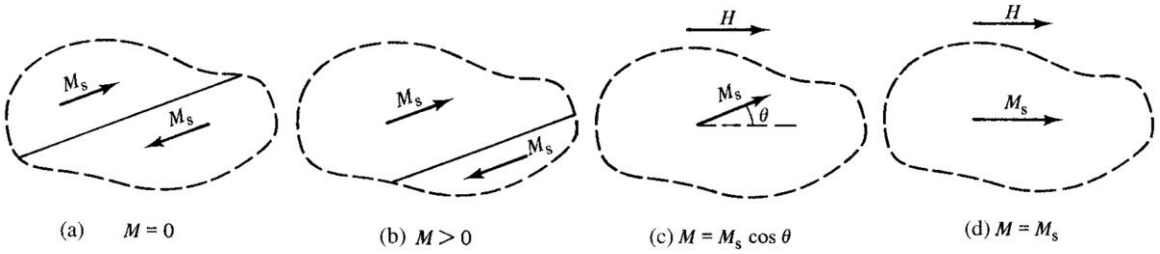

Figure 3 Domain wall movement and eventually magnetization saturation in the applied field direction.

With the application of magnetic field, the domains in which the spontaneous magnetization direction is closer to the applied magnetic field, grow by domain wall

movement. When it becomes single domain then magnetization flips in the applied magnetic direction. Further increase in applied magnetic field does not increase the value of magnetization. This particular value is called saturation magnetization (M_s). Ferromagnets have the property of retaining memory of the applied field even after its removal. The curve one gets on plotting magnetization versus magnetic field for a ferromagnetic material is called hysteresis loop. Figure 4 shows a typical hysteresis loop.

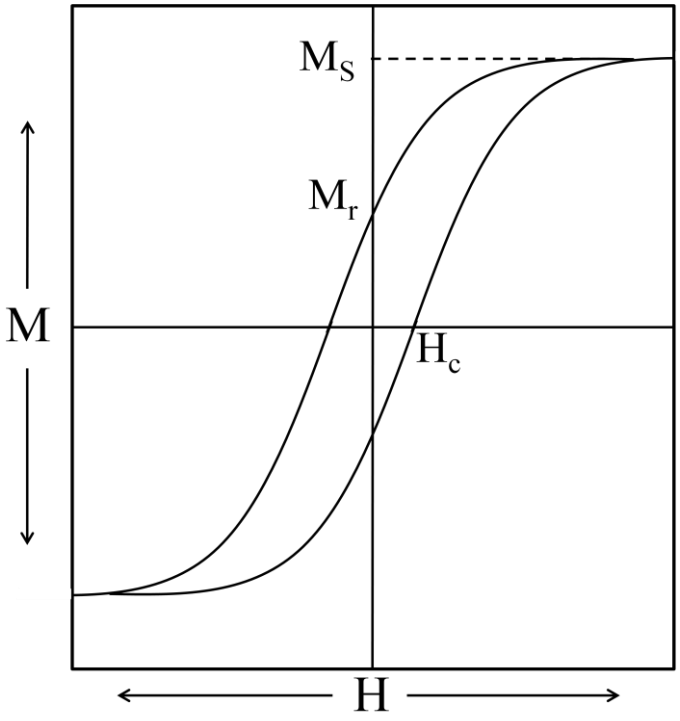

Figure 4 Hysteresis loop of a typical ferromagnetic material

H_c = Coercive field

M_r = Remanent magnetization

M_s = Saturation magnetization

A ferromagnetic material is not ferromagnetic for all temperature range. Even in the presence of molecular field, at high enough temperature thermal effect destroys the exchange interaction to randomize the moments. The particular temperature at which a ferromagnetic material becomes paramagnetic is called Curie temperature (T_C). Below T_C, the material is magnetically ordered and above T_C it obeys Curie-Weiss law with a positive value of Weiss constant.

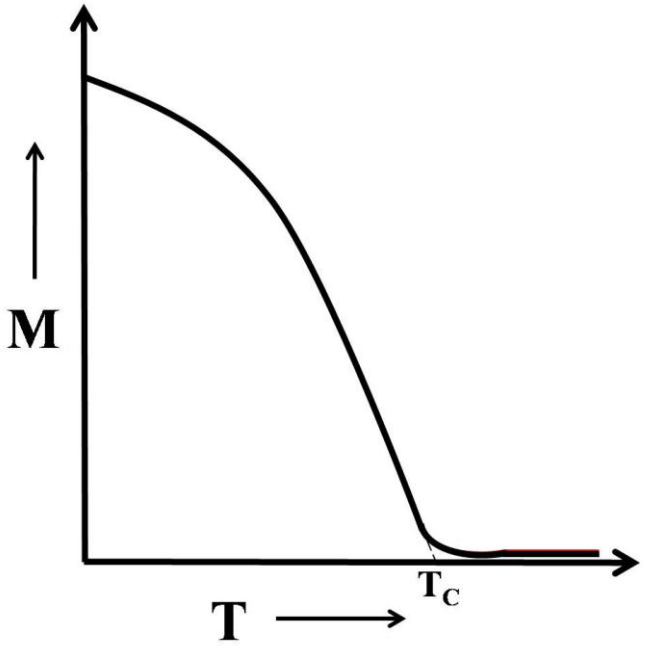

Figure 5 M vs. T plot for a typical ferromagnetic material.

1.1.4. Antiferromagnetic Materials:

Materials which exhibit antiferromagnetism have ordered magnetic moments with neighbouring moments aligned anti-parallel. The lattice constituting moments aligned in the same direction is said to be one sublattice. Hence the net moment of individual sublattices are same in magnitude but opposite in direction.

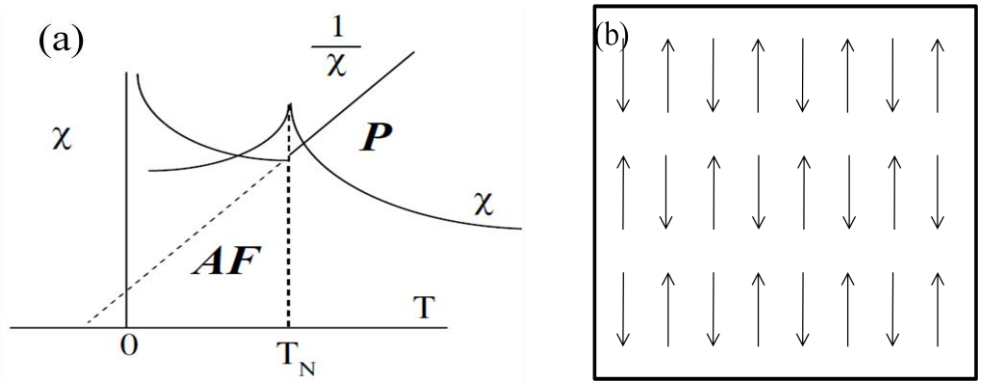

Figure 6(a) Variation of susceptibility and inverse of susceptibility with temperature, (b) arrangement of moments in an antiferromagnetic material.

An antiferromagnetic material (AFM) remains in the ordered magnetic state below T_N which is called Neel's temperature. Above T_N, it shows paramagnetic behaviour due to thermal effect. The paramagnetic state can be fitted to Curie-Weiss law with negative value of Weiss constant.

1.1.5. Ferrimagnetic Materials:

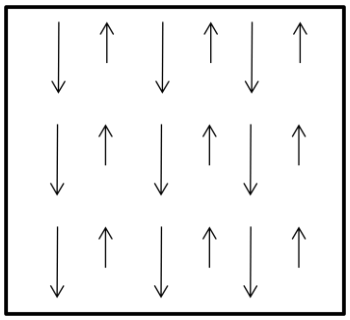

These materials were thought to be ferromagnetic until Neel postulated the theory of ferrimagnetism. Ferrimagnetic materials are similar to AFM in a way that they also contain at least two sublattices with moments aligned anti-parallel but unlike AFM, magnitude of moments are different. Ferrimagnetic materials show properties like spontaneous magnetization, Curie temperature, hysteresis and remanence which are characteristics of a ferromagnetic material. Magnetite is a very familiar example of a ferrimagnetic material.

1.2. Classification of ferromagnetic materials:

Among all the magnetic materials, ferromagnetic materials are the most widely studied and exploited for application point of view. Following are the important classes of ferromagentic materials which have been studied extensively in the past:

1.2.1 Metallic ferromagnets:

Fe, Co and Ni are ferromagnetic with very high values of T_C. The origin of ferromagnetism can be understood using Stoner's band theory.[1] Foundation of band theory is in the concept of exchange energy. Figure 7(b) shows valence band of transition

metals. 4s and 3d bands overlap with each other and together form valence band. For all these metals 4s band contain only 0.6 electrons, which can be envisaged from the fact that 4s band is very broad with very less density of state. On the other hand, 3d band is narrow with large density of states hence containing remaining of the valence band which is 9.40 in number in the case of Ni. This is the reason why Fermi level of Ni is slightly below the edge of the valence band. Similarly, other lower transition metals also have their Fermi level inside the 3d band. Exchange energy provides the required force to align the

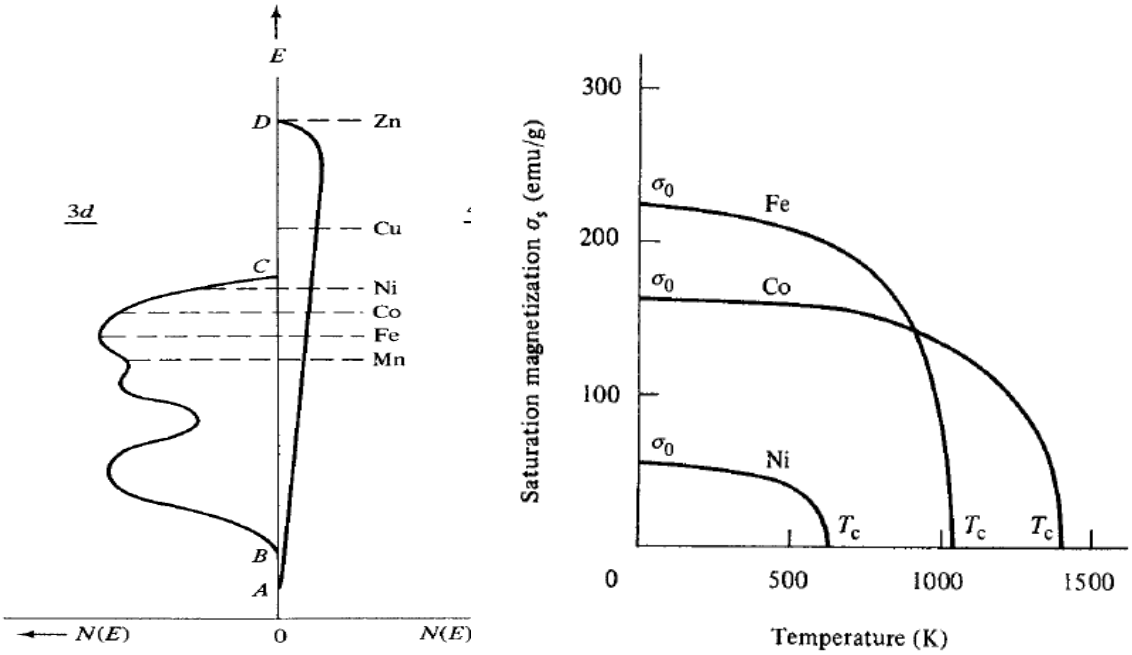

Figure 7 Band structure of first row transition metals, (b) magnetization vs. temperature plot ferromagnetic transition metals.

spins in net upward or downward fashion to result in ferromagnetism. Cu has 3d band full and 4s band cannot contribute towards ferromagnetism because exchange energy is not sufficient enough to promote the electrons to higher energy levels due to large interstates energy difference. Zn has both 3d as well as 4s band full. It has been observed that exchange energy cannot keep one band full of electron if the other band is less than

half filled. In case of Mn and lower transition metals for saturation magnetization the other band should be less than half filled.

1.2.2 Ferromagnetism in transition metal oxides:

Binary oxides like MnO, CoO etc are antiferromagnetic due to superexchange[2, 3] interactions but oxides like $La_{1-x}M_xMnO_3$ (M=Ca, Sr etc) more popular for their magnetoresistance have ferromagnetic ordering. Due to doping of divalent alkaline earth metals manganese exists as Mn^{3+} and Mn^{4+}. Hybridization with the intermediate 2p orbital of O^{2-} in these manganites results in ferromagnetic interaction between Mn^{3+} and Mn^{4+} and such interaction is called double exchange interaction.[4, 5] There are some exceptions where superexchange can also lead to ferromagnetic ordering for example in the case of EuO and $CrBr_3$. The general mechanism for superexchange in insulators involves hybridization of 2p orbital of oxygen with 3d orbital of transition metals which have been shown in Figure

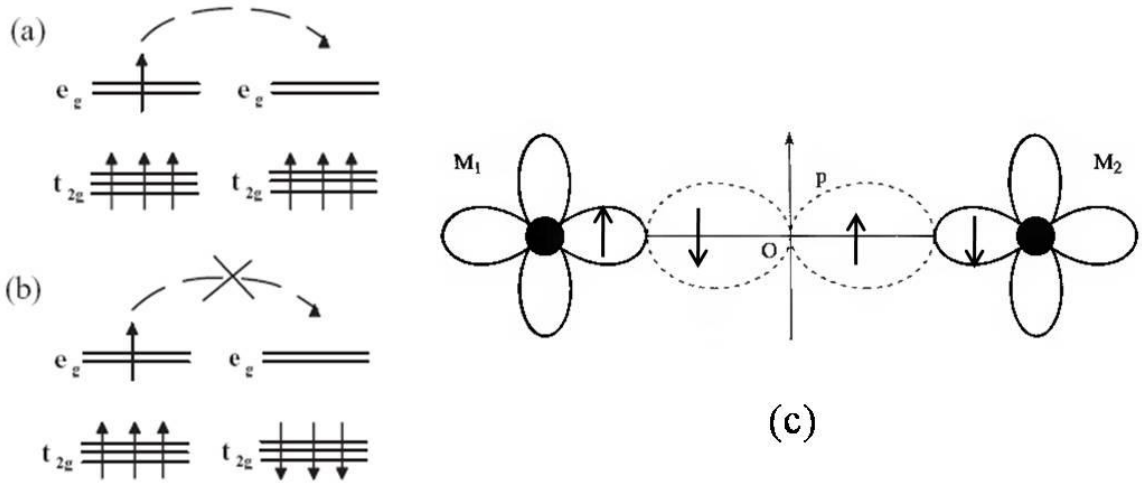

Figure 8 Following Hund's rule, the extra electron of the Mn3+ ion can delocalize onto the site of a neighbouring Mn4+ only if the spins are parallel [configuration (a)]. In the case of configuration (b), the extra electron remains localized on Mn3+. (c) superexchange mechanism favouring antiferromagnetism. M_1 and M_2 are 3d orbitals of transition metal.

1.2.3 Dilute Magnetic semiconductors (DMS):

Ferromagnetism in dilute magnetic semiconductors created intense interest in research in such materials due to its potential application in spintronics.[6] Transition metal ions are doped in semiconductors like TiO_2, ZnO, GaN etc. After a theoretical prediction of ferromagnetism in 5 % Mn doped ZnO by Dietl *et al.*[7] first experimental report of DMS was published by Matsumoto *et al.* where they doped 7% cobalt in anatase (TiO_2) thin film by pulsed-laser deposition method.[8] They reported moment of 0.32 μ_B per Co^{2+} and Curie temperature more than 400 K. Following this discovery many other semiconductors like ZnO, GaN were doped with transition metal ions doped with Mn, Co, Fe, Ni and Cu.[9-13] In $Ga_{1-x}Mn_xAs$, Mn provides both electronic doping as well as magnetic substitution while in the case of $Zn_{1-x}Mn_xO$ separate electronic dopant is needed. Provided that magnetic ions are homogenously distributed in the semiconducting matrix, interactions like double exchange and superexchange cannot operate because they vanish exponentially with distance. The long range ferromagnetic exchange between localized moments can be mediated by hole (electron) in the valence (conduction) band. There are many reports of paramagnetism in doped semiconductor systems and they that origin of ferromagnetism in such materials are purely nonintrinsic in nature and can be attributed to the clustering of magnetic ions.[14, 15]

1.3. Magnetic Anisotropies:

Magnetic hysteresis loops can have variety of shapes. The main factor on which it strongly depends is magnetic anisotropy.[16, 17] In a very simple word it means that magnetic properties depend on the direction in which they are measured.

1.3.1 Crystalline Anisotropy:

Ease of magnetizing of a crystalline substance is not same in all the crystallographic directions. It is easier to magnetize a magnetic crystal in certain direction (easy axis) than other directions called (hard directions). For Fe and Ni which have cubic symmetry easy direction is <111>, while <110> and <100> are medium and hard directions as shown in Figure 9.

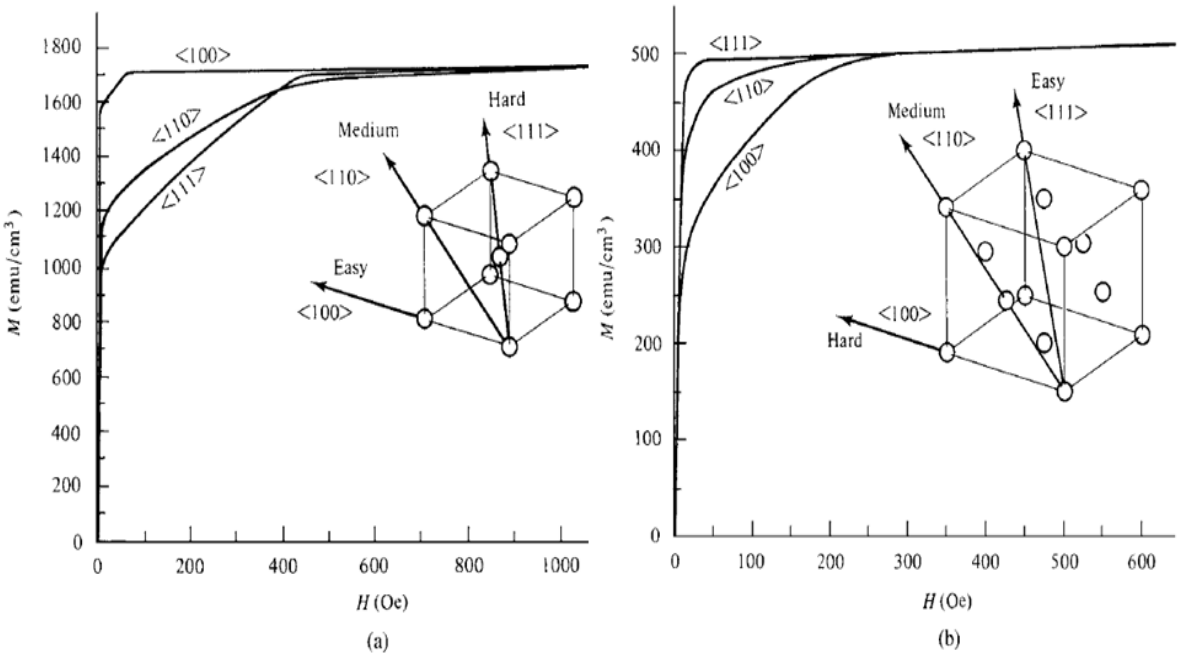

Figure 9 Magnetization curves for single crystals of iron (a) and nickel (b).*(ref. 18)*

The direction of easy magnetization of a crystal is the direction of spontaneous domain magnetization in the demagnetized state. Magnetization curves of cobalt, which has a hexagonal close-packed structure at room temperature, are shown in Figure 10. The hexagonal c axis is the direction of easy magnetization, all other directions in the basal plane are found to be equally hard.

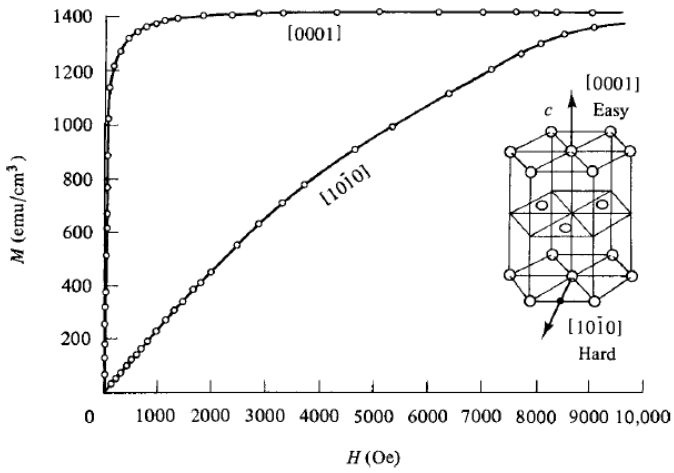

Figure 10 Magnetization curves for a single crystal of cobalt.

Crystal anisotropy is mainly due to spin-orbit coupling. When an external field tries to reorient the spin of an electron, the orbit of that electron also tends to be reoriented. But the orbit is strongly coupled to the lattice and therefore resists the attempt to rotate the spin axis. The energy required to rotate the spin system of a domain away from the easy direction, which we call the anisotropy energy, is just the energy to overcome the spin–orbit coupling. This coupling is relatively weak, because fields of a few hundred oersteds are usually strong enough to rotate the spins. The strength of the anisotropy in any particular crystal is measured by the magnitude of the anisotropy constants K_1, K_2, etc.

1.3.2 Shape Anisotropy:

The second type of anisotropy is due to the shape of a mineral grain. A magnetized body will produce magnetic charges or poles at the surface. This surface charge distribution, acting in isolation, is itself another source of a magnetic field, called the demagnetizing field. It is called the demagnetizing field because it acts in opposition to the magnetization that produces it. For example, take a long thin needle shaped grain.

The demagnetizing field will be less if the magnetization is along the long axis than if is along one of the short axes. This produces an easy axis of magnetization along the long axis. A sphere, on the other hand, has no shape anisotropy. The magnitude of shape anisotropy is dependent on the saturation magnetization. For magnetite, smaller than about 20 microns, shape anisotropy is the dominant form of anisotropy. In larger sized particles, shape anisotropy is less important than magnetocrystalline anisotropy. For hematite, because the saturation magnetization is so low, shape anisotropy is usually never important.

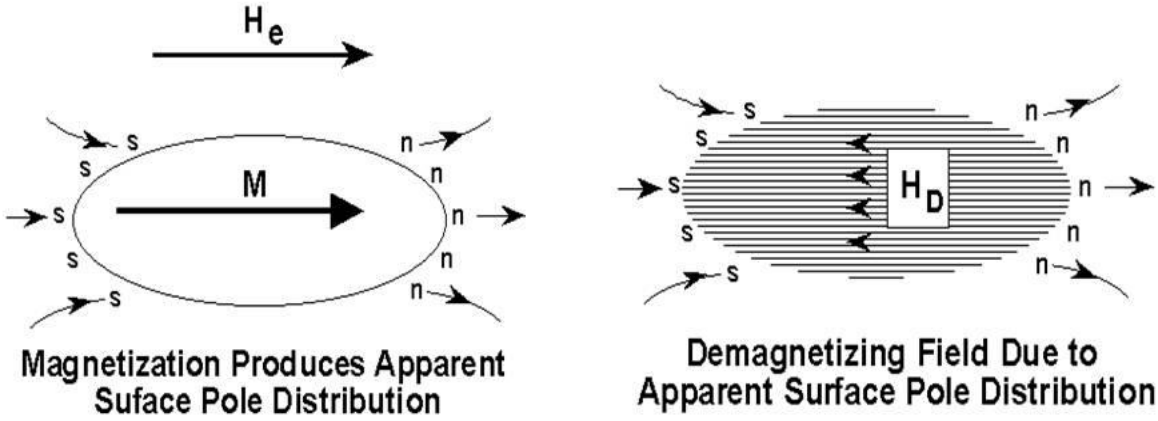

Figure 11 Demagnetizing field as the origin of shape anisotropy.

1.3.3 Stress Anisotropy:

In addition to magnetocrystalline anisotropy, there is another effect related to spin-orbit coupling called magnetostriction. Magnetostriction arises from the strain dependence of the anisotropy constants. Upon magnetization, a previously demagnetized crystal experiences a strain that can be measured as a function of applied field along the principal crystallographic axes. A magnetic material will therefore change its dimension when magnetized.

The inverse effect, or the change of magnetization with stress also occurs. A uniaxial stress can produce a unique easy axis of magnetization if the stress is sufficient to overcome all other anisotropies. The magnitude of the stress anisotropy is described by two more empirical constants known as the magnetostriction constants (λ_{111} and λ_{100}) and the level of stress.

1.4. Magnetism of Nanomaterials:

The main implication of working at the nano-scale is that the particle size becomes comparable or even less than that of the domain size and the magnetic material starts behaving as superparamagnet. This can be realized in many applications like magnetic storage media,[19] biosensing applications,[20] medical applications, such as targeted drug delivery,[21, 22] contrast agents in magnetic resonance imaging (MRI),[23–30] and magnetic inks for jet printing.[31] Like bulk ferromagnets, an array of single domain magnetic nanoparticles can exhibit hysteresis in the magnetization versus field dependence. A traditional bulk ferromagnet experiences an increase in magnetization with increase in field as the domains grow via domain wall to result in a net magnetization. However, in single domain particles, the moment of each particle interacts with its neighbours and the field to align in the field direction. The key difference between the magnetic behaviour of a bulk magnetic material and a collection of single domain ferromagnetic nanoparticles arises from the mechanism by which the magnetization is cycled through the hysteresis loop. In a bulk material, the magnetization increases in response to the field via domain wall nucleation and rotation as well as the rotation of the magnetization vector away from the easy axis of magnetization. In a single

domain nanoparticle, domain wall movement is not possible and only coherent magnetization rotation can be used to overcome the effective anisotropy (K) of the particle.[32] Thus the maximum coercivity of a given material as a function of particle diameter actually falls in the single domain range. The critical diameter for a magnetic particle to reach the single domain limit is equal to

$$R = \frac{36\sqrt{AK}}{\mu_0 M_S^2}$$

where A is the exchange constant, K is the effective anisotropy constant and Ms is the saturation magnetization.[33] For most magnetic materials, this diameter is in the range 10–100 nm, though for some high-anisotropy materials the single domain limit can be several hundred nanometres.[33]

For a single domain particle, the amount of energy required to reverse the magnetization over the energy barrier from one stable magnetic configuration to the other is proportional to KV/k_BT where V is the particle volume, k_B is Boltzmann's constant and T is temperature.[34] If the thermal energy is large enough to overcome the anisotropy energy, the magnetization is no longer stable and the particle is said to be superparamagnetic (SPM). That is, an array of nanoprticles each with its moment can be easily saturated in the presence of a field, but the magnetization returns to zero upon removal of the field as a result of thermal fluctuations (i.e. both M_r and H_C are zero). This behavior is analogous to conventional paramagnets, only instead of individual electronic spins displaying this fluctuating response, it is the collective moment of the entire particle, hence the term ''superparamagnetism''.[35] The temperature at which the thermal energy can overcome the anisotropy energy of a nanoparticle is referred to as the blocking

temperature, T_B.[34] For nanoparticles with a distribution in volume, T_B represents an average characteristic temperature and can be affected by inter-particle interactions as well as the timescale over which the measurement is performed due to the magnetic relaxation of the particles.[36] Keeping these things in mind, T_B as the general transition from ferromagnetism to superparamagnetism is one of the most important quantities that define the magnetic behaviour of an assembly of particles. Figure 12(a) shows a schematic of magnetization vs. temperature plot for single domain nanoparticles along with the schematic illustrating the difference in the magnetization versus field behavior of of single domain magnetic nanoparticles in the blocked state (Figure 1b) and of superparamagnetic nanoparticles (Figure 1c).

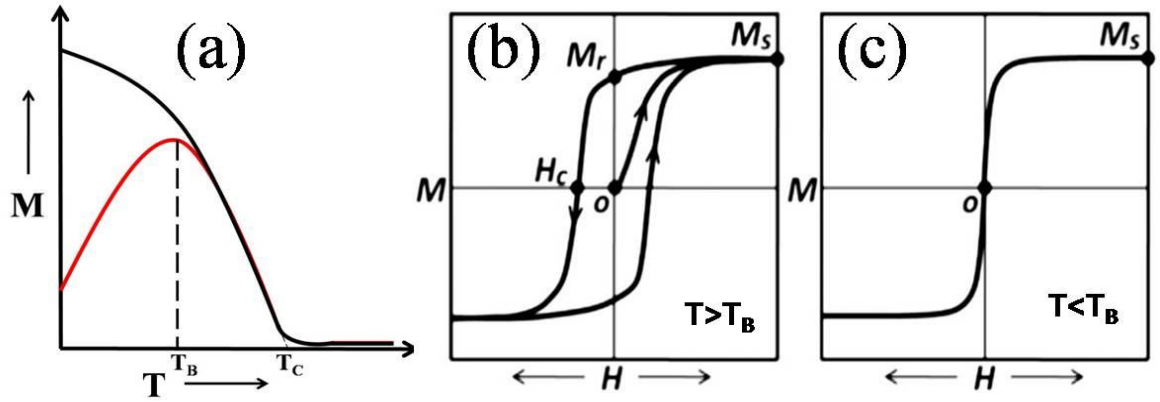

Figure 12 Schematic illustration of (a) magnetization vs. Temperature plot for single domain nanoparticles showing blocking temperature (T_B), (b) typical hysteresis loop of an array of single domain ferromagnetic nanoparticles for $T<T_B$ and (b) a typical curve for a superparamagnetic material at $T>T_B$.

1.5. Ferromagnetism as a universal property of inorganic nanoparticles

Ferromagnetism in otherwise nonmagnetic materials has emerged as a very interesting area of research in recent years.[37-57] 'Otherwise nonmagnetic materials' refer to the compounds in which the magnetism does not involve unpaired d or f electrons. 'd^o ferromagnetism' is sometimes used to define this phenomenon. In 2005 Venkatesan *et al*

observed ferromagnetic ordering in HfO_2 thin film.[58] This was the first report of ferromagnetism in a compound without any unpaired d or f electron. In the following years nanoparticles of many oxides ranging from insulators (CeO_2, Al_2O_3) to semiconductors (ZnO, In_2O_3, SnO_2) were reported to show ferromagnetism.[36] Nanoparticles of non oxide systems like CdS, GaN and NbN were also reported to be ferromagnetic at room temperature.[40, 59]

All such reports of ferromagnetism have been observed either in nanoparticles or thin film which itself can be considered as a nano system because one of its dimension is in the nano range. In both the cases surface contribution dominates over bulk. Surface shows many interesting physical and chemical properties which are very different from its bulk counterpart. In all the cases of ferromagnetism reported, magnetic contribution has been attributed to be coming from the surface while the bulk remains diamagnetic or paramagnetic depending on the system. Surface of nanoparticles has large concentration of point defects. Point defect as a reason of surface ferromagnetism has now been accepted. The question, how these point defects ultimately give rise to ferromagnetic ordering, is now driving this field forward.

1.6 Implications of Surface Ferromagnetism:

Surface ferromagnetism as a subject is not only interesting in Physics point of view but it can also have many implications. One of the most interesting examples is multiferroic behaviour of $BaTiO_3$ nanoparticles (Figure 13).[60] Bulk $BaTiO_3$ is a well known ferroelectric material but at nanoscale due to surface ferromagnetism it has been shown to behave as multiferroic with positive magnetocapcitance near the ferroelectric transition temperature. Hence, it shows both ferromagnetic as well as ferroelectric hysteresis loop at

room temperature. In a very similar work films of GaN grown within mica-4 channels have shown to be multiferroic.[61]

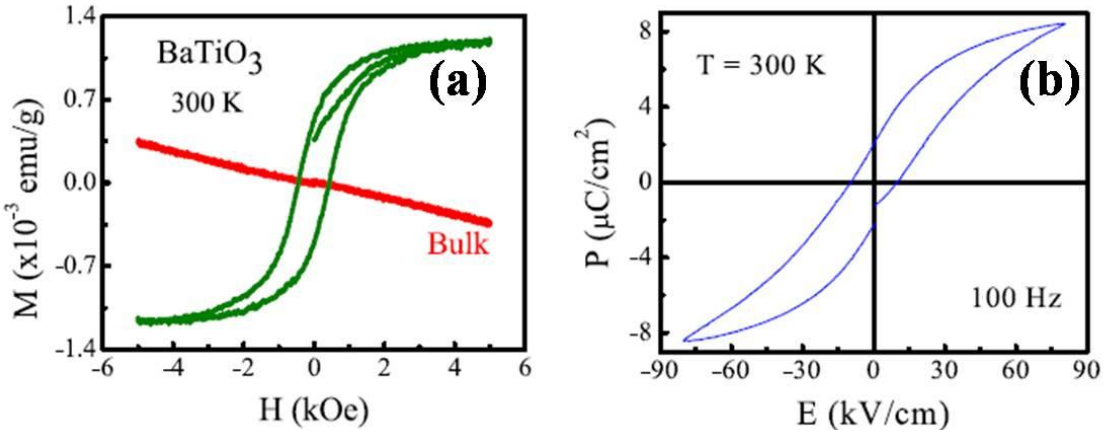

Figure 13(a) Magnetic and (b) ferroelectric hysteresis curves exhibited by nanocrystalline $BaTiO_3$ at room temperature. Bulk barium titanate is diamagnetic and ferroelectric.*(ref. 60)*

Superconductivity and magnetism are generally considered not to be present in the same phase. It has been shown by Sundaresan *et al.* that the nanoparticles of $YBa_2Cu_3O_{7-y}$ can be considered as superconducting core with ferromagnetic shell due to defects. The sample gives ferromagnetic hysteresis loop at 300 K and 91 K (Figure 14). Shape of the loop obtained at 90 K as shown in the inset of Figure 14, suggests the co-existence of superconducting core with ferromagnetic shell.[40]

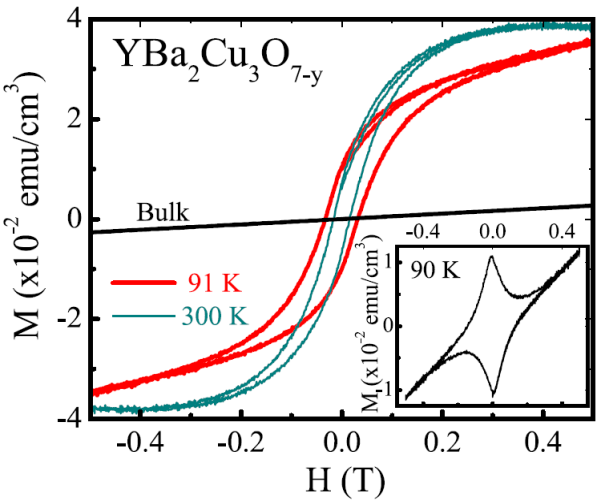

Figure 14 Magnetization curves of superconducting YBCO nanoparticles showing Magnetization curves of superconducting YBCO nanoparticles showing surface ferromagnetism. The inset shows the magnetization curve at thesuperconducting transition *(ref. 40)*

1.7 References:

(1) Stoner, E. C. *Philos. Mag.* **1933**, *15*, 1080.

(2) Anderson, P.W. *Phys. Rev.* **1950**, *79*, 350.

(3) Anderson, P.W. *Phys. Rev.* **1959**, *115*, 2.

(4) Anderson, P.W.; Hasegawa, H. *Phys. Rev.* **1955**, *100*, 675.

(5) Gannes, P. G. D. *Phys. Rev.* **1960**, *118*, 141.

(6) Wolf, S. A. *et al*. *Science* **2001**, *294*, 1488.

(7) Dietl et al., *Science*, **2000**, *287*, 1019.

(8) Matsumoto, Y.; Murakami, M.; Shono, T.; Hasegawa, T.; Fukumura, T.; Kawasaki, M.; Ahmet, P.; Chikyow, T.; Koshihara, S.; Koinuma, H. *Science* **2001**, *291*, 854.

(9) Ney, A.; Ollefs, K.; Ye, S.; Kammermeier, T.; Ney, V.; Kaspar, T. C.; Chambers, S. A.; Wilhelm, F.; Rogalev, A. *Phys. Rev. Lett.* **2008**, *100*, 157201.

(10) Barla, A. *et al. Phys. Rev. B* **2007**, *76*, 125201.

(11) Jayakumar, O. D.; Salunke, H. G.; Kadam, R. M.; Mohapatra, M.; Yaswant, G.; Kulshreshtha, S. K. *Nanotechnology* **2006**, *17*, 1278.

(12) Sarigiannidou, E.; Wilhelm, F.; Monroy, E.; Galera, R. M.; Bellet-Amalric, E.; Rogalev, A.; Goulon, J.; Cibert, J.; Mariette, H. *Phys. Rev.* B **2006**, *74*, 041306

(13) Mahadevan, P.; Mahalakshmi, S. *Phys. Rev.* B **2006**, *73*, 153201.

(14) Lawes, G. A.; Risbud, S.; Ramirez, A.P.; Seshadri, R. *Phys. Rev. B* **2006**,*71*, 045201.

(15) Rao, C.N.R.; Deepak, F.L.; *J. Mater. Chem.* **2005**, *15*, 573.

(16) Powell, F. C. *Proc. R. Soc. London*, **1930**, *130*, 167.

(17) Fowler, R. H.; Powell, F. C. *Proc. Cambridge Philos. Soc.* **1931**, *27*, 280.

(18) Honda, K.; Kaya, S. *Sci. Reports Tohoku Univ.* **1926**, *15*, 721.

(19) Sun, S.; Murray, C. B.; Weller, D.; Folks, L.; Moser, A. *Science* **2000**, *287*, 1989.

(20) Miller, M. M.; Prinz, G. A.; Cheng, S. F.; Bounnak, S. *Appl. Phys. Lett.* **2002**, *81*, 2211.

(21) Jain, T. K.; Morales, M. A.; Sahoo, S. K.; Leslie-Pelecky, D. L.; Labhasetwar, V. *Mol. Pharm.* **2005**, *2*, 194.

(22) Chourpa, I.; Douziech-Eyrolles, L.; Ngaboni-Okassa, L.; Fouquenet, J. F.; Cohen-Jonathan, S.; Souce, M.; Marchais, H.; Dubois, P. *Analyst* **2005**, *130*, 1395.

(23) Bulte´, J. W. *Methods Mol. Med.* **2006**, *124*, 419.

(24) Modo, M.; Bulte´, J. W. *Mol. Imaging* **2005**, *4* (3), 143. .

(25) Burtea, C.; Laurent, S.; Roch, A.; Vander Elst, L.; Muller, R. N. *J. Inorg. Biochem.* **2005**, *99*, 1135.

(26) Boutry, S.; Laurent, S.; Vander Elst, L.; Muller, R. N. *Contrast Med. Mol. Imaging* **2006**, *1*, 15.

(27) Babes, L.; Denizot, B.; Tanguy, G.; Le Jeune, J. J.; Jallet, P. *J. Colloid Interface Sci.* **1999**, *212*, 474.

(28) Sonvico, F.; Dubernet, C.; Colombo, P.; Couvreur, P. *Curr. Pharm. Des.* **2005**, *11*, 2091.

(29) Corot, C.; Robert, P.; Idee, J. M.; Port, M. *Ad*V. *Drug Deli*V*ery Re*V. **2006**, *58*, 1471.

(30) Modo, M. M. J.; Bulte´, J. W. M. *Molecular and Cellular MR Imaging*; CRC Press: Boca Raton, FL, 2007.

(31) Charles, S. W.; Popplewell, J. *Endea*V*our* **1982**, *6*, 153.

(32) Stoner, E.; C. Wohlfarth, E. P. *Philos. Trans. R. Soc.* **1948**, *240*, 599.

(33) Skomski R.; Coey, J. M. D. *Institute of Physics Publishing*, **1999**, Bristol and Philadelphia,

(34) Neel, L. *C. R. Acad. Sci.* **1949**, *228*, 664.

(35) Bean, C. P. *J. Appl. Phys.* **1955**, *26*, 1381.

(36) Majetich, S. A.; Sachan, M. *J. Phys. D: Appl. Phys.*, **2006**, *39*, R407.

(37) Sundaresan, A.; Bhargavi, R.; Rangarajan, N.; Siddesh, U.; Rao, C. N. R. *Phys. Rev.* B **2006,** *74*, 161306(R).

(38) Sundaresan, A.; Rao, C.N.R. *Nanotoday* **2009**, *4*, 96.

(39) Sundaresan, A.; Rao, C.N.R. *Solid State Commun.* **2009**, *149*, 1197.

(40) Shipra; Gomathi, A.; Sundaresan, A.; Rao, C.N.R. *Solid State Commun.* **2007**, *142*, 685.

(41) Li, M.; Ge, S.; Qiao, W.; Zhang, L.; Zuo, Y.; Yan, S. *Appl. Phys. Lett.* **2009**, 94, 152511.

(42) Panchakarla, L. S.; Sundarayya, Y.; Manjunatha, S.; Sundaresan, A.; Rao, C. N. R. *ChemPhysChem* **2010**, 00, 1.

(43) Mangalam, R.V.K.; Ray, N.; Waghmare, U.; Sundaresan, A.; Rao, C.N.R. *Solid State Commun.* **2009,** *149*, 1.

(44) Elfimov, I.S.; Yunoki, S.; Sawatzky, G.A. *Phys. Rev. Lett.* **2002**, *89*, 216403.

(45) Osorio-Guille´n, J.; Lany, S.; Barabash, S.V.; Zunger, A. *Phys. Rev. Lett.* **2006**, *96*, 107203.

(46) Gao, F.; Hu, J.; Yang, C.; Zheng, Y.; Qin, H.; Sun, L.; Kong, X.; Jiang, M. *Solid State Commun.* **2009**, *149*, 855.

(47) Wang, F.; Pang, Z.; Lin, L.; Fang, S.; Dai, Y.; Han, S. *Phys. Rev. B* **2009**, *80*, 144424.

(48) Ge, M. Y.; Wang, H.; Liu, E. Z. ; Liu, J. F.; Jiang, J. Z.; Li, Y. K.; Xu, Z. A.; Li, H. Y. *Appl. Phys. Lett.* **2008**, *93*, 062505.

(49) Stoneham, M. *J. Phys.: Condens. Matter* **2010**, *22*, 074211.

(50) Schoenhalz, A. L.; Arantes, J. T.; Fazzio, A.; Dalpian, G. M. *Appl. Phys. Lett.* **2009**, *94*, 162503.

(51) Wang, H.; Yan, Y.; Li, K.; Du, X.; Lan, Z.; Jin, H. *Phys. Status Solidi B* **2010**, *247*, 444.

(52) Hong, N. H.; Sakai, J. Poirot, N.; Brizé, V. *Phys. Rev. B* **2006**, *73*, 132404.

(53) Gao, D.; Zhang, Z.; Fu, J.; Xu, Y.; Qi, J.; Xue, D. *J Appl. Phys.* **2009**, *105*, 113928.

(54) Ma, Y. W. *et al. J Appl. Phys.* **2009**, *95*, 072501.

(55) Hong, N. H.; Poirot, N.; Sakai, J. Phys. Rev. B *2008*, *77*, 033205.

(56) Podila, R. *et al. Nano Lett.* DOI: 10.1021/nl1001444.

(57) Qin, S. *et al. J. Phys. Chem. Lett.* **2010**, *1*, 238.

(58) Venkatesan, M.; Fitzgerald, C. B.; Coey, J. M. D. *Nature* **2004**, *430*, 630.

(59) Madhu, C.; Sundaresan, A.; Rao, C.N.R. *Phys. Rev. B* **2008**, *77*, *201*,306.

(60) Mangalam, R. V .K.; Ray, N.; Waghmare, U.; Sundaresan, A.; Rao, C. N. R. *Solid State Commun.* **2009,** *149*, 1.

(61) Bhattacharya, S.; Datta, A.; Chakravorty, D. *Appl. Phys. Lett.* **2010**, *96*, 093109.

CHAPTER 2

Investigation of Ferromagnetism in MgO nanoparticles

Summary*

Positron annihilation spectroscopy has been used to explore the nature of defects and to estimate the defect concentrations in ferromagnetic MgO nanoparticles. Our experimental results show that Mg vacancies are present at the concentration of 3.4×10^{16} cm^{-3} in the nano-crystalline MgO which is halved in the bulk sample. This is in correlation with the decrease of the intensity of blue luminescence and the saturation magnetic moment with increasing particle size. These results clearly demonstrate that the ferromagnetism in MgO nanoparticles arises from Mg vacancies at the surface of the particles. In addition, effect of Li doping on the magnetic properties of MgO nanoparticles have been studied. The results show that 10 % Li doping in MgO nanoparticles almost doubles the value of saturation magnetization at room temperature.

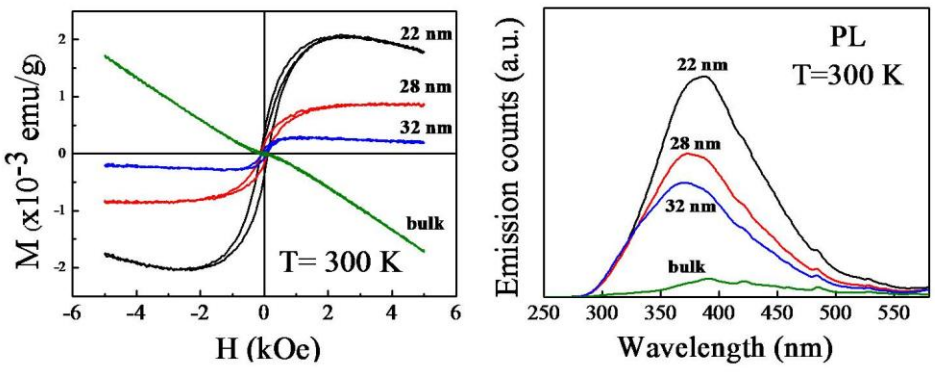

* Paper based on this work has appeared in *Chem. Phys. Lett.* ***2009****, 477, 360*.

2.1 Introduction:

Very many oxide systems have been reported to show ferromagnetism in nano scale in recent past. Among them, investigation of ferromagnetism in MgO nanoparticles is particularly interesting because of its very simple rock salt type structure. Moreover MgO is very ionic. Due to the same reason many theoretical work based on first principle calculations have been carried out in order to explain ferromagnetism in alkaline earth metal oxides like MgO and CaO.[1-5] In fact ferromagnetism in CaO with cation vacancies was predicted much earlier than its experimental verification.[1] It has been shown that ferromagnetism in MgO appears due to neutral Mg vacancies. One advantage in working with MgO nanoparticles is, unlike other alkaline earth metal oxides it does not absorb atmospheric CO_2. Synthesis and characterisation of MgO nanoparticles are hence not troublesome. In addition to the defects arising at the surface of the nanoparticles naturally, doping cations of different valancy can further increase the amount of defects. Effect of such doping on the ferromagnetic properties of MgO will improve our understanding of magnetism in otherwise nonmagnetic inorganic materials.

2.2 Understanding the Origin of Ferromagnetism in MgO:

MgO crystallizes in rock salt type structure with one Mg surrounded by six O atoms and vice-versa. Generally, there are two kinds of point defects in MgO, which are O vacancy (V_O) and Mg vacancy (V_{Mg}). Effect of 3.125 % V_o and V_{Mg} on magnetism has been shown in Figure 1. Figure 1(a) shows DOS of pure MgO (Mg32O32 supercell) where spin up and spin down bands are same to give net zero moment. Valence band is composed of 2p orbital of oxygen which is completely filled whereas conduction band is formed mainly by 3s of Mg is completely empty. Figure 1(d) is DOS of O 2p which is

essentially similar to DOS of pure MgO. The effect of one V_O (Mg32O31supercell) has been shown in Figure 1(b, e). It is clear that V_O creats no spin polarization and the total magnetic moment of the system remains zero. Figure 1(c, f) shows effect of one V_{Mg} (Mg31O32 supercell) on DOS. Due to the open cell of V_{Mg} it leads to triplet state which is found to be ground state in MgO.

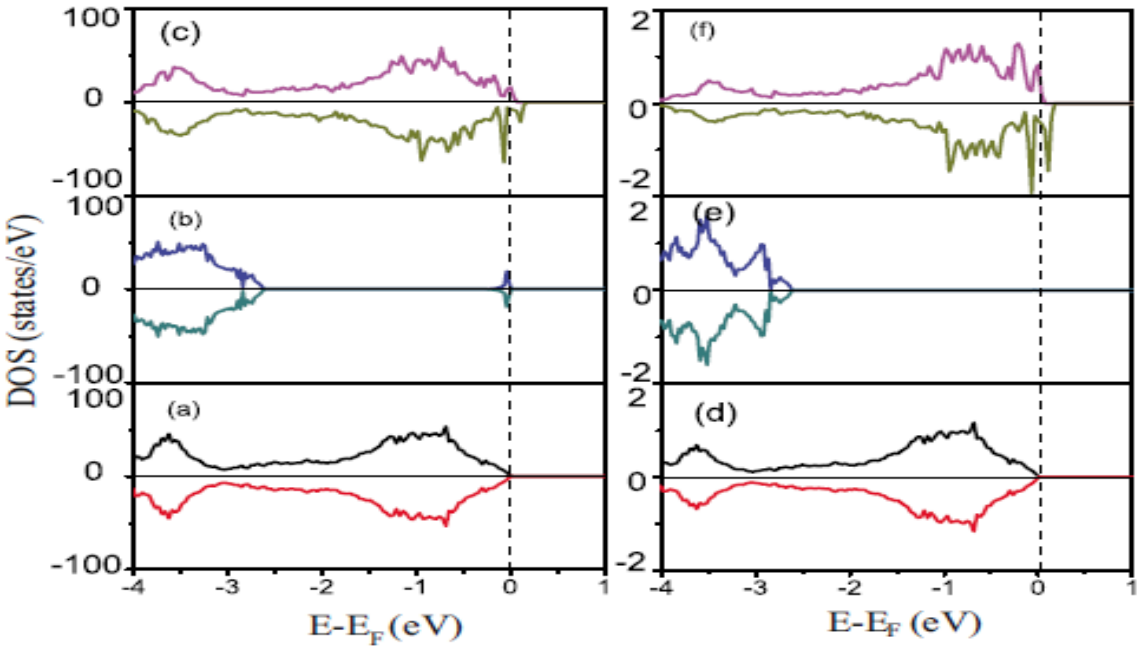

Figure 1 Total DOS and O 2p partial DOS of (a, d) the perfect MgO crystal (Mg32O32); (b, e) MgO bulk with one O vacancy (Mg32O31); (c, f) MgO bulk with one Mg vacancy (Mg31O32). In (b, e) and (c, f), the vertical dashed lines represent the Fermi energy, which is set to zero.*(ref. 4)*.

Unlike V_O, V_{Mg} leads to spin polarization. Fermi energy moves to lower energy with empty states at the top of valence band. Asymmetry in the spin up and spin down DOS results in local magnetic moments coming mainly from spin polarization of O 2p orbitals. One Mg vacancy creates two holes in the system and after outwards relaxation of six nearest O atoms calculated magnetic moment generated is 1.51 μ_B. The main contribution to the total magnetic moment arises from the six nearest six nearest

neighbour to the V_{Mg} and is absent on Mg atoms. This can be visualized from the isosurface plot of the spin density of Mg31O32 supercell with one Mg vacancy.

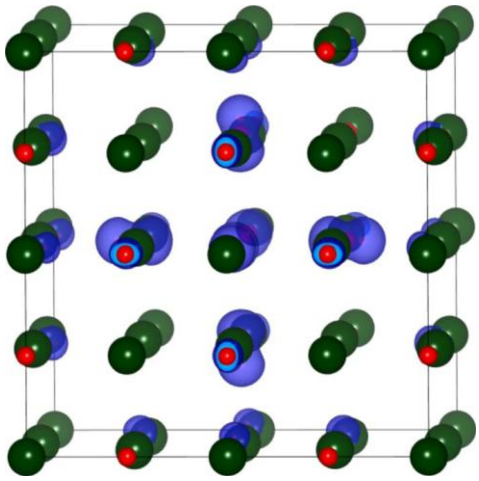

Figure 2 The isosurface plot of the spin density of Mg31O32 supercell with one Mg vacancy. The red small spheres represent O atoms, the large green spheres represent Mg atoms, and the blue isosurface shows the spin density.*(ref. 4)*.

2.3 An Overview of Positron Annihilation Spectroscopy:

The positron or antielectron is the antiparticle or the antimatter counterpart of the electron. The positron has an electric charge of +1, a spin of ½, and the same mass as an electron. The existence of positrons was first postulated in 1928 by Paul Dirac as a consequence of the Dirac equation.[6]The electromagnetic interaction between electrons and positrons makes possible annihilation of $e^+ - e^-$ pairs in which the total energy of the annihilating pair may be transferred to quanta of the electromagnetic field (annihilation photons g). Principal channel of this reaction is the two-photon annihilation:

$$e^+ + e^- \rightarrow g_1 + g_2$$

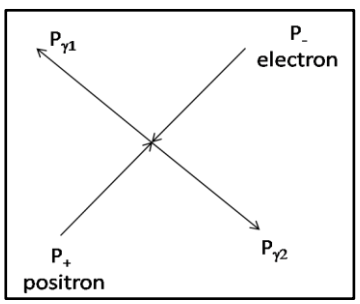

Figure 3 Annihilation of a positron.

The role of conservation of energy and momentum in process is illustrated in Figure 3. In the centre-of-mass frame of the $e+ - e-$ pair, the energies of the both annihilation photons are equal to the rest energy of the electron (positron), $E_0 = m_0c^2$ (511 keV), and the two photons are emitted in the strictly opposite directions. The electron (positron) rest mass is designated as m_0 and c is the light velocity.[7, 8]

This process is characterised also with annihilation rate λ which is which is related to the positron lifetime (t) as inverse ($t = g^{-1}$). It has been found that λ is proportional to the effective electron density ne sampled by positron.

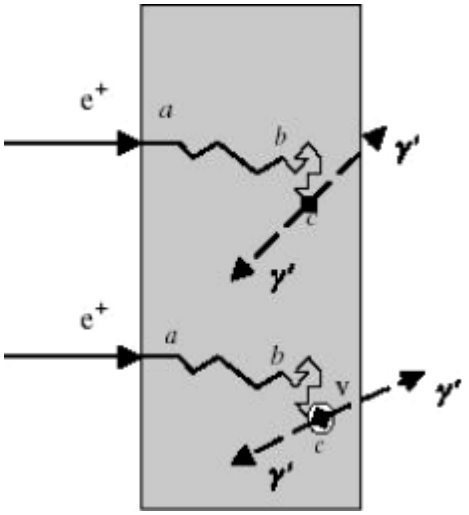

Figure 4 Schematic view of possible fates of positrons implanted in a solid. Upper track: implantation (a), slowing-down (*a* to *b*), thermal diffusion (*b* to *c*), annihilation at *c* with a bulk electron and emission of two photons (γ'). Lower track: same as above from *a* to *c*, trapping at *c* in a vacancy (v), annihilation in v

During diffusion, the positron interacts with its surroundings and eventually annihilates with an environmental electron. In homogeneous defect-free media all positrons annihilate with the same rate λ_b which is a characteristic of the given material. Due to the Coulomb repulsion by the positive-ion cores, positron in a condensed medium preferably resides in the inter-atomic space. At open-volume defects (monovacancies, larger vacancy clusters, dislocations etc.), the potential sensed by the positron is lowered due to reduction in the Coulomb repulsion. As a result, a localised positron state at the defect can have a lower energy than the state of delocalised (free) positron . The transition from the delocalised state to the localised one is called positron trapping. Positron binding

energies E_b to defects like, e.g., monovacancies are typically of a few eV. Thermal detrapping is impossible from such deep traps and positron remains trapped until annihilation. If a positron trap is shallow enough (Eb < 0.1 eV), phonon-assisted detrapping occurs. As local electron density at the defect site is lowered compared to that of the unperturbed regions, lifetime t_t of the trapped positrons is correspondingly longer than $t_b = \lambda_b^{-1}$. Positron trapping is characterised by trapping rate which is proportional to defect concentration Ct in the sample, $t = \mu \times C_t$. Trapping coefficient μ, called specific trapping rate, together with annihilation rate $\lambda_t = t_t^{-1}$, are specific for given kind of defects.[9]

When a positron is trapped, annihilation takes place with the characteristics determined by the local electron density, which is lower in the open-volume defect than in the bulk. The reduced electron density implies a reduced annihilation rate. Thus trapped positrons survive for more time in comparison to the free ones. In many insulators, the positron can form a bound state with a host electron, positronium (Ps), which is an analogue of the hydrogen atom.[7] Ps atom can exist in the singlet (parapositronium, pPs) or the triplet (orthopositronium, oPs) state.

2.3.1 Positron lifetime spectroscopy:

Positrons can have several states each of which gives a characteristic lifetime τi = 1/ λi. The positron lifetime spectrum, i.e. the probability of annihilation at time t, is thus the sum of exponential decay components with relative intensities I_i.

$$-\frac{dn(t)}{dt} = \sum_i I_i \lambda_i \exp[-\lambda_i t], \quad \sum_i I_i = 1$$

$$\tau_{av} = \sum_i I_i + \tau_i$$

Here n(t) is the probability that a positron is still alive at time t after its emission. Experimentally, the lifetime of a positron is time delay between the positron emission and annihilation.

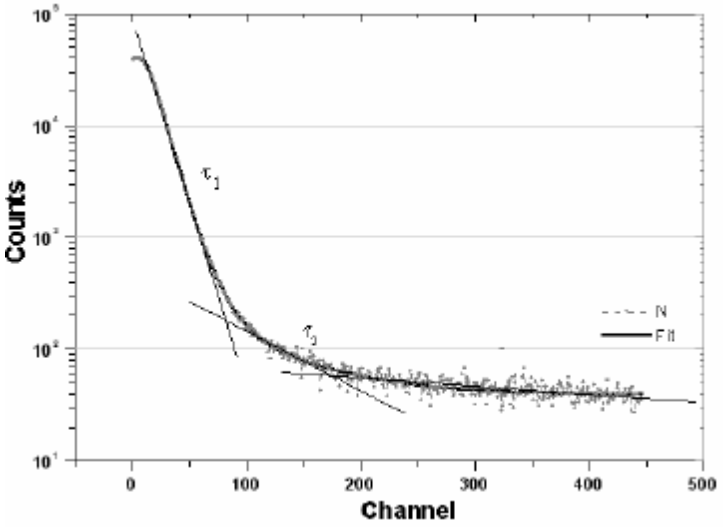

Figure 5 A positron lietime spectrum and its decomposition into two components.

2.4 Scope of the Present Work:

Origin of surface ferromagnetism in otherwise non-magnetic materials is one area which lacks a unified theory. However, defect related origin has been considering in most of the experimental and theoretical work done in recent past in this field. Present work is one further attempt to understand ferromagnetism in MgO nanoparticles which show diamagnetic behaviour in the bulk form. Nature and concentration of defects can give an insight to look at this problem in deeper a sense. For this regard, we have chosen two of the most potent tools namely photoluminescence and positron annihilation spectroscopy in order to investigate nature and the concentration of defects.

2.5 Experimental Procedure:

MgO nanoparticles were synthesized using high purity (99.99%) magnesium acetate tetrahydrate (CH3COO)$_2$Mg.4H2O, polyvinyl pyrrolidone (PVP) and ethylene glycol (EG, 99.5%) as reported earlier.[10] A simple scheme for the synthesis of MgO nanoparticles is shown in Figure 6.

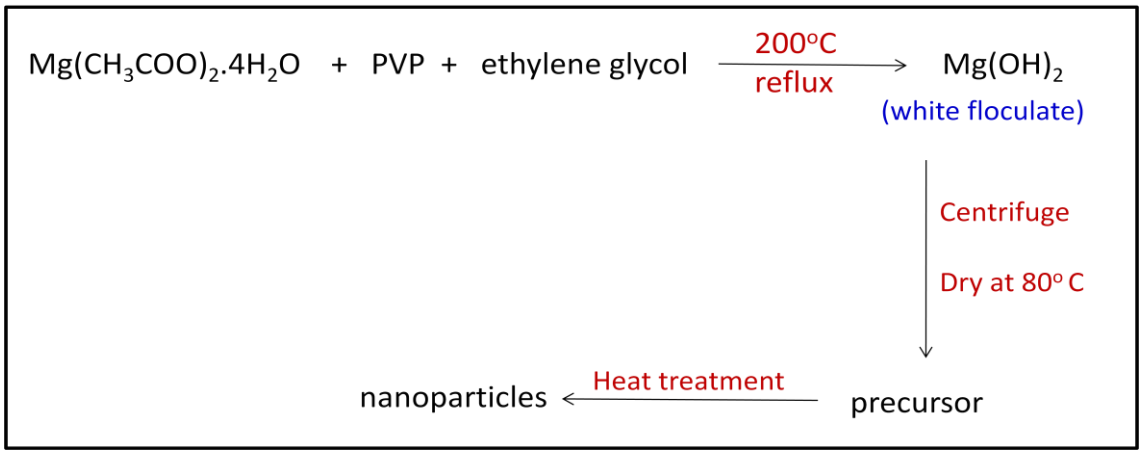

Figure 6 Scheme for MgO nanoparticles synthesis

0.05 mol of magnesium acetate tetrahydrate and 0.3 mmol of PVP as capping agent were dissolved in EG in a round bottom flask connected to condenser. The solution was refluxed at 200 ^{o}C with constant stirring for 2 h to get a white flocculate. The reaction mixture was allowed to cool down to room temperature. The flocculate was collected by centrifuging the reaction mixture at 6000 rpm followed by washing with distilled water and then ethanol to remove remaining PVP and EG. Final drying of the flocculate was done at 80 ^{o}C in an oven to get magnesium oxide precursor. Precursor was calcined at 650, 750 and 850 ^{o}C for 2 h in oxygen atmosphere to form magnesium oxide nanoparticles of different sizes in a tube furnace. Bulk magnesium oxide was prepared by palletizing the nanoparticles followed by sintering at 1450 ^{o}C in air in a box furnace. All the heat treatments of precursor were done in alumina boat. Precautions were taken to

avoid any metallic contacts with the sample in order to avoid extrinsic magnetic contamination. For the study of Li doping the samples were prepared as follows:

6.4102 g of $Mg(NO_3).6H2O$ was dissolved in 20 ml ethanol. A dilute aqueous solution of KOH (0.001 M) was added dropwise with constant stirring in order to precipitate magnesium nitrate. A thick gel was obtained which was centrifuged at the rate of 4000 rpm followed by several cycles of washing first with distilled water and then with ethanol. The white product (precursor) was dried at 80 ^{o}C for 4 h. Precursor was divided into two parts, the first part of which was mixed with stoichiometric amount (10 %) of $LiNO_3$. Second part was not mixed with anything. Both the parts were heated at 650 ^{o}C in oxygen atmosphere for 4 h.

2.6 Characterization:

For X-ray diffraction (XRD), samples were properly ground and levelled on a quartz sample holder in order to avoid any height mismatch within the sample space. XRD patterns were recorded with a Rigaku-99 Miniflex II diffractometer using Cu Ka radiation (k = 1.5406 Å).

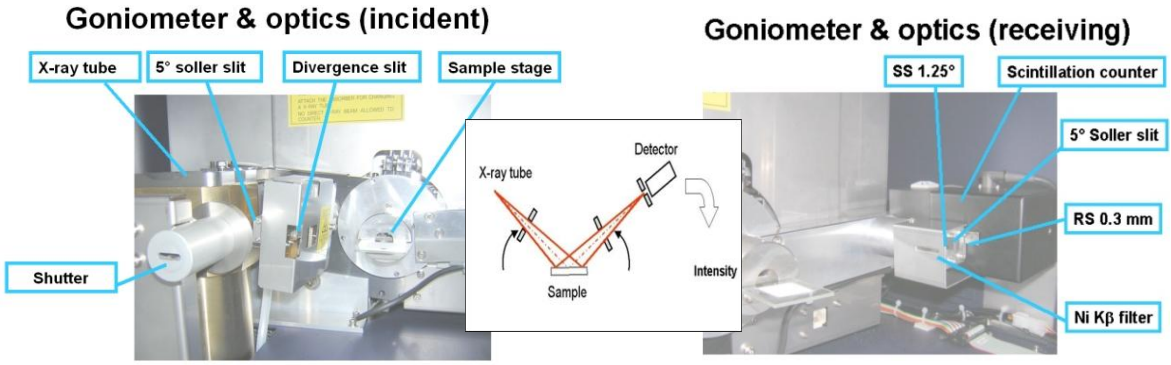

Fig. 4 Arrangement and optics of XRD instrument used.

X-ray tube remains stationary while the sample and detector move in order to do vary angle (2θ) and collecting diffracted X-rays. Detector moves twice the speed of sample holder. The arrangement and the optics of the instrument is shown in fig. 4. 1 h scan of all the nanoparticles and bulk sample were carried out. Crystallite size was calculated from Scherrer's formula

$$t = \frac{0.9\lambda}{B\cos\theta_B}$$

Where λ is wavelength of X-ray used, B is full width at half maxima of the peak considered and θ_B is the corresponding angle of the peak considered.

Photoluminescence (PL) spectra were recorded in PERKIN ELMER LS 55 Luminescence Spectrometer. All the PL measurements were carried out on solid samples without dispersing them in any solvent in order to avoid solvent effect in the spectra observed. 290 nm filter was used all the measurements to get rid of first harmonic effect in the spectra. Excitation and emission slits were kept 10 mm each.

Particle size and morphology were analyzed by Field Emission Scanning Electron Microscopy (FESEM) using NOVA NANOSEM 600 (FEI, Netherlands). For FESEM, small amount of sample was dispersed in alcohol and drops of this dispersion were taken on aluminium stub and then evaporated before irradiating it with electron beam. High vacuum mode was used for taking FESEM images to prevent air scattering.

Magnetic measurements were carried out with vibrating sample magnetometer in Physical Properties Measurement System (PPMS, Quantum Design, USA). Rectangular pellets of dimension 6 mm x 3 mm were hydraulically pressed. The pellet was mounted in quartz sample holder and wrapped with brown tape both provided by Quantum Design.

For background correction magnetic measurement of sample holder and brown tape only were carried out.

For positron annihilation studies, a 10 μCi ^{22}NaCl source of positrons (enclosed between 2 μm thin nickel foils) was sandwiched between two identical and plane faced pallets.[11, 13] The positron annihilation lifetime were measured with a fast-slow coincidence assembly. Detectors were 25-mm-diam x 25-mm-long cylindrical BaF_2 scintillators optically coupled to Philips XP2020Q photomultipliers tubes. The resolving time (full width at half maximum, FWHM) measured with a ^{60}Co source and with the windows of the slow channels of the fast-slow coincidence assembly set to select pulses corresponding to 300 keV to 550 keV in one channel and 700 keV to 1320 keV in the other, was 250 ps. For each positron annihilation lifetime spectrum about 10^6 coincidence counts were recorded. For each sample at least five to six positron annihilation lifetime spectra of about 10^6 coincidence counts were recorded to ensure the repeatability of the measurements. Measured positron annihilation lifetime was analyzed by computer programme PATFIT-88 with necessary source corrections (446 ps of 4 % intensity) to evaluate the possible lifetime component τ_i, and their corresponding intensities I_i.[14] For the coincidence Doppler broadening of annihilation γ-radiation (CDBAR) measurement, two identical HPGe detectors (Efficiency: 12 % ; Type : PGC1216sp of DSG, Germany) of energy resolution 1.1 keV at 514 keV of ^{85}Sr was used as two 511 keV γ-ray detectors.[15] The CDBAR spectrum was recorded in a dual ADC based multiparameter data acquisition system (MPA-3 of FAST ComTec, Germany). The peak to background ratio of this CDBAR measurement system, with ± ΔE selection, was ~10^5:1.[12, 16, 17] CDBAR spectra were also analyzed by constructing by constructing the ratio curve.

2.7 Results and Discussion:

XRD patterns of MgO particles annealed at different temperatures, as shown in Figure 7, confirm that the sample is single phase with cubic structure. Peaks become broader with the increase in size of nanoparticles. Scherrer formula was used to calculate crystallite size from peak broadening which comes about 22 nm for the sample annealed at 650^{o}C. The average particle size increases to 28, 32 nm for the sample annealed at 850 and 950^{o}C respectively. The sample sintered at 1450^{o}C shows sharp lines in XRD pattern which is typical of bulk crystalline sample. These results are in agreement with FESEM images as shown in Figure 8. FESEM images show that nanoparticles are agglomerated which is due to the annealing the precursor at high temperature. As the annealing temperature is increased agglomeration in the sample also increases. The bulk sample which is formed by heating the nanoparticles sample at 1450 ^{o}C for

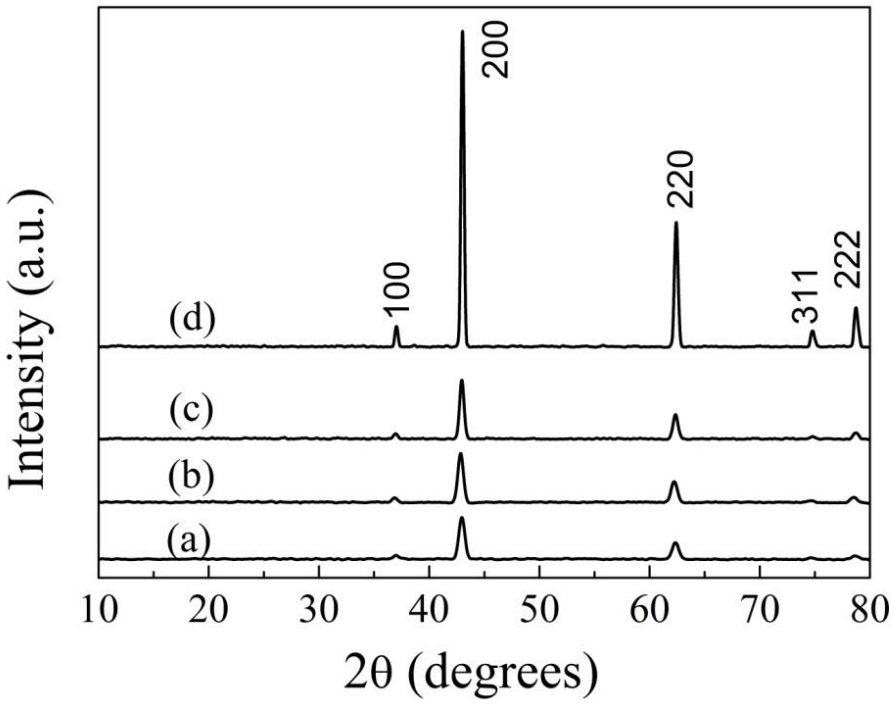

Figure 7 XRD patterns of MgO nanoparticles of size (a) 22 nm, (b) 28 nm, (c) 32

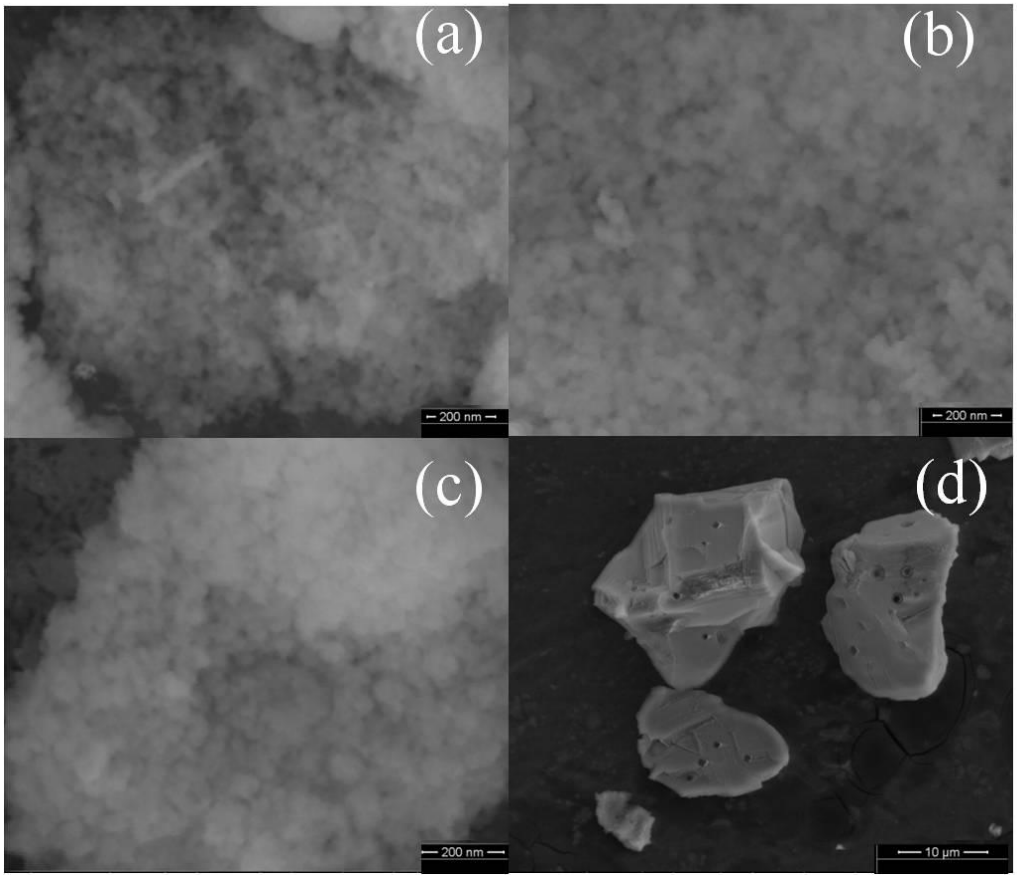

Figure 8 FESEM images of MgO nanoparticles of size (a) 22 nm, (b) 28 nm, (c) 32 nm and (d) bulk.

24 hours is micron sized annealing the precursor at high temperature. As the annealing temperature is increased agglomeration in the sample also increases. The bulk sample which is formed by heating the nanoparticles sample at 1450 ^{o}C for 24 hours is micron sized.

The results of magnetization measurements performed at 300 K on the three nanoparticles and bulk MgO are shown in Figure 9. All the nanoparticles show ferromagnetic hysteresis at room temperature. The saturation magnetization (0.00204 emu/g) is higher for the 22 nm sample. As the average particle size increases, the value of saturation magnetization decreases which is consistent with the earlier suggestion that magnetism comes from surface defects which decreases with increase of particles size due to decrease in surface to volume ratio.[18]

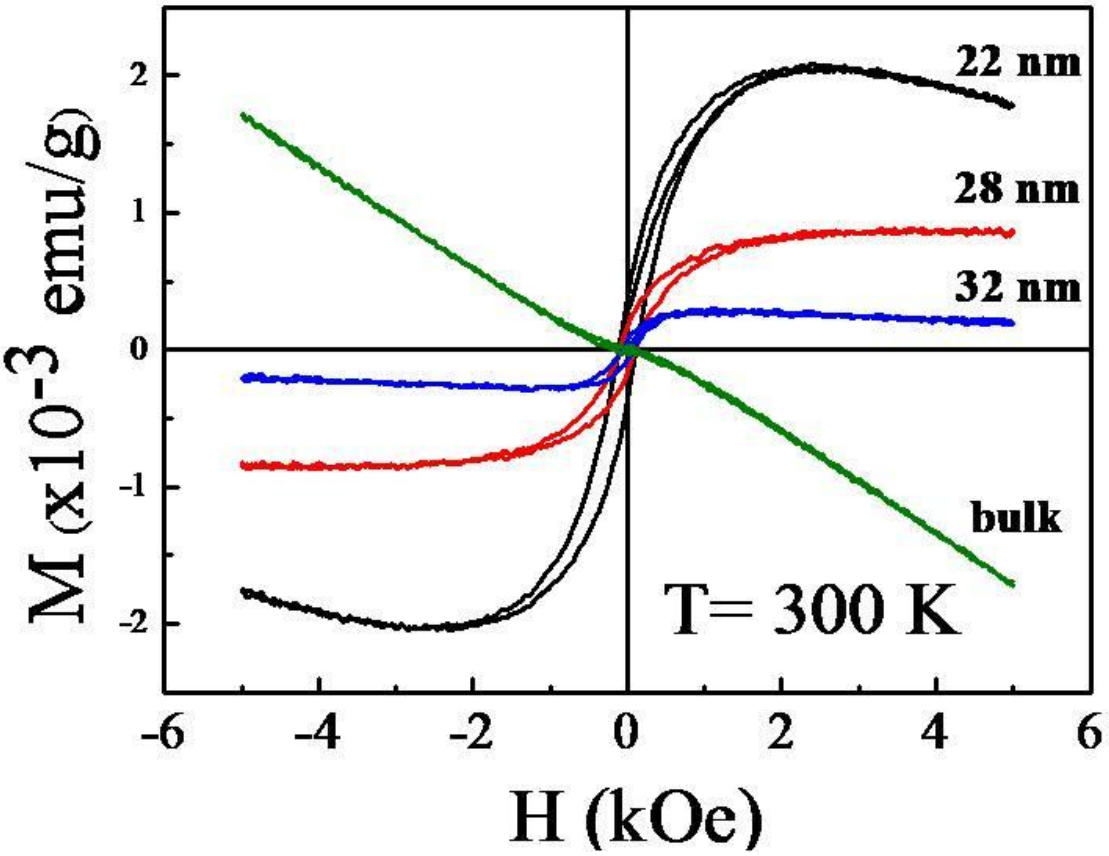

Figure 9 Ferromagnetic hysteresis loops of MgO nanoparticles of size 22, 28, 32 nm and bulk.

The bulk sample which was heated at 1450^{o}C shows diamagnetic behaviour as expected. In all the curves for nanoparticles samples diamagnetic contribution is subtracted. Diamagnetic contribution essentially comes from the bulk of the nanoparticles, brown tape and sample holder. Diamagnetic correction can be made by subtracting the bulk sample magnetic contribution performed with almost equal amount of brown tape.

Optical properties of nanomaterials provide important information about the surface states. It is known that nanocrystals of MgO show a broad photoluminescence (PL) spectrum in the blue region due to low coordinated surface ions or defects.[19-22] It should be noted that bulk MgO does not show such luminescence spectrum consistent with relatively low concentration of surface defects.

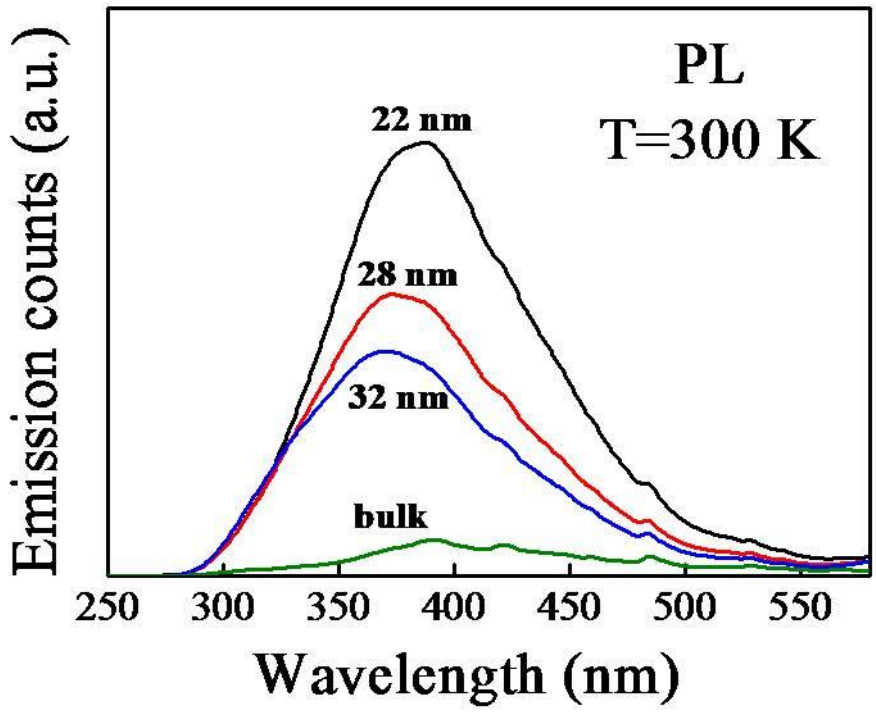

Figure 10. PL spectra of MgO nanoparticles of size 22, 28, 32 nm and ulk

Figure 10 shows PL spectra of the three nanoparticles and the bulk sample excited at the wavelength 225 nm. It can be seen that there is a broad peak centered around 370 nm whose intensity decreases with increase of particle size. Such a broad PL peak has already been reported in the literature and has been attributed to defects. In the present work, the observation that the peak intensity decreases with increase of particle size suggests the concentration of surface defect decreases with increasing particle size.

In order to find the nature of defect and estimate its concentration, positron annihilation spectroscopy has been used. Table 1 shows the value of positron lifetimes, their corresponding intensities and finally the defect concentrations of 22 nm particles and bulk sample. The free fitting of all the positron lifetime spectra for both the samples (bulk and sample annealed at 650^{o}C) are found to be best fitted (variance of fit is less than 1 per channel) with three lifetime

components (Figure 11) yielding a very long lifetime component (τ_3) with intensity (I_3) of 5 ± 0.2 %. This component is due to the formation of orthopositronium and its subsequent decay as parapositronium by pick-off annihilation processes.

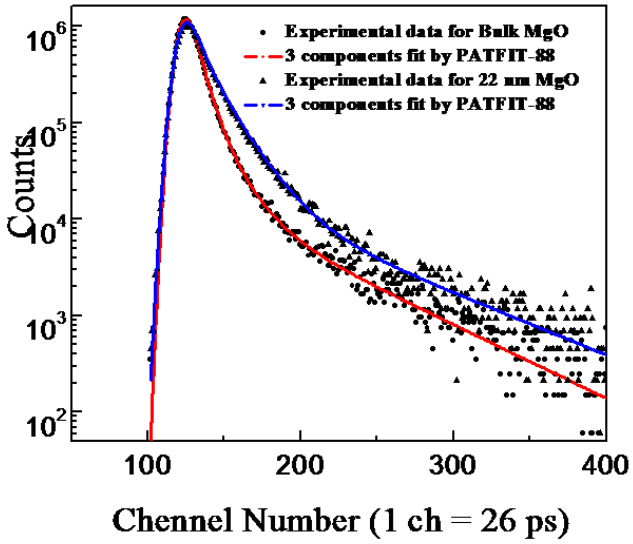

Figure 11 Positron lifetime spectra of nanoparticle and bulk sample.

Sample MgO	τ_1 (ps)	I_1 (%)	τ_2 (ps)	I_2 (%)	τ_3 (ps)	I_3 (%)	V_{Mg}
Bulk	161± 4	70±1	385±10	25±1	1610±50	5±0.2	1.6×10^{16}
22 nm	168±4	38±1	400±10	57±1	1730±50	5±0.2	3.4×10^{16}

Table 1. Positron lifetimes and corresponding intensities of 22 nm particles and bulk MgO.

Positronium formation is always favourable in polycrystalline samples due to the presence of microvoids. The short lifetime component (τ_1) of 161±4 ps and 168±4 ps for bulk and the 22 nm MgO sample respectively is generally attributed to the free annihilation of positrons. Theoretically calculated free positron lifetime in bulk MgO is 166 ps which is in agreement with the presently observed values. The most important lifetime component is the intermediate one, τ_2, which arises from the annihilation of positrons at defect sites. In the present case τ_2 is found to be ~ 385 ps and 400 ps for the bulk and nanocrystalline MgO,

respectively, which is coming from the annihilation of positron in the Mg vacancy type defect or Mg vacancy clusters.

One can have an idea about the defect concentration from I_2, the intensity of the intermediate lifetime component. It obvious from table 1, that I_2 which is a measure of defect concentration is higher in nanoparticles (57 %) than that in the bulk sample (25 %). As the grain size decreases more positrons diffuse towards the grain surfaces and trapped in the defect sites present on the surface. Assuming a specific trapping coefficient of $\mu_v \sim 3 \times 10^{15}$ sec^{-1} at 300 K, similar to the Ga vacancy in GaN , the Mg vacancy in MgO has been calculated by the relation $[V_{Mg}] = N_{at}\mu_v^{-1}\tau_B^{-1}(\tau_{ave} - \tau_B) / (\tau_2 - \tau_{ave})$, where τ_B = bulk positron lifetime, τ_{ave} = average positron lifetime, τ_2 = positron lifetime at defect site, N_{at} is the atomic density, in case of MgO it is $\sim 5 \times 10^{22}$ cm^{-3}.[23] The Mg vacancy in bulk MgO and nano-crystalline MgO comes out to be $(V_{Mg})_{Bulk} \sim 1.6 \times 10^{16}$ cm^{-3} ; $(V_{Mg})_{Nano} \sim 3.4 \times 10^{16}$ cm^{-3}, respectively. Therefore, the suppression of magnetization with increase of particle size is in agreement with the decrease of defect concentration, since $(V_{Mg})_{Nano} / (V_{Mg})_{Bulk} \sim 2$.

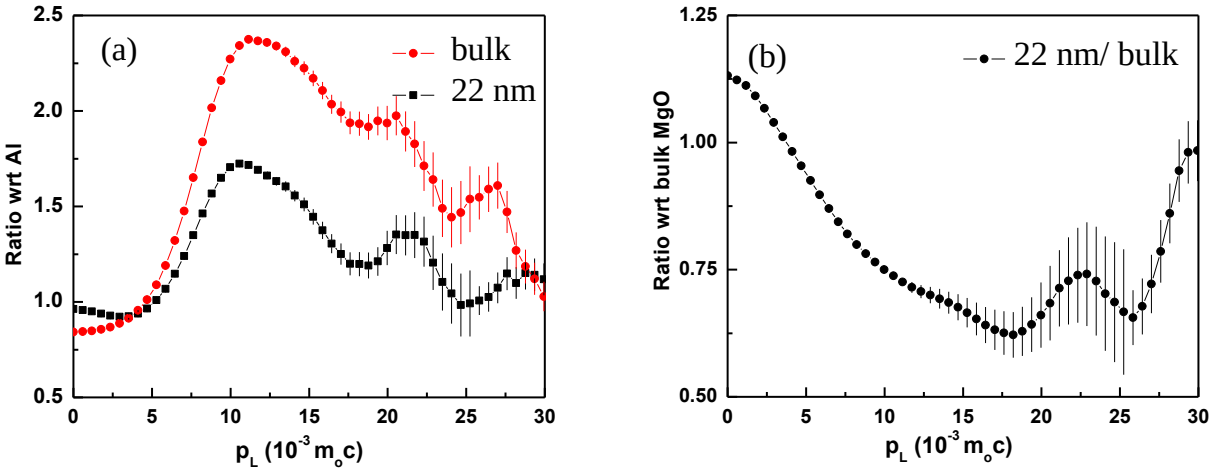

Figure 12 Area normalized ratio curves of 22 nm and bulk MgO CDBAR spectra with respect to defects free 99.9999 % purity Al CDBAR spectrum. (b) Area normalized ratio curve of 22 nm MgO CDBAR spectrum with respect to bulk MgO CDBAR spectrum.

Figure 12(a) shows the area normalized ratio curve of bulk and nanocrystalline MgO CDBAR spectra with respect to CDBAR spectrum of defects free 99.9999% purity Al sample.[24-27] Both the ratio curves (Figure 12(a)) show a major peak at ~ 11×10^{-3} $m_o c$, which is extended upto 30×10^{-3} $m_o c$.

In general, the peak at momentum value ~ 11×10^{-3} $m_o c$ in the ratio-curve with respect to Al is mainly coming from the annihilation of positrons with the 2p electrons of Oxygen and some contributions coming from the annihilations of core electrons of Mg while the higher momentum region solely represents the annihilation of positrons with the core electrons of Mg.[25] The most significant part of the Figure 12(a) is that throughout the momentum range (5×10^{-3} $m_o c$ to 30×10^{-3} $m_o c$) the ratio-curve for the nano-crystalline MgO is significantly less than that for bulk MgO. This picture is much clear in Figure 12(b) where a ratio curve has been constructed between the CDBAR spectrum of nano-crystalline MgO with respect to the CDBAR spectrum of bulk MgO. Figure 12(b) shows a prominent dip in the momentum value 17×10^{-3} $m_o c$, which indicates less annihilation of positrons with the core electrons of Mg in nano-crystalline MgO with respect to the bulk MgO. This indicates the presence of a significant amount of Mg vacancy in nano-crystalline MgO. Our results are consistent with the theoretical calculations on MgO which showed that neutral Mg vacancies induce large magnetic moment on neighboring oxygen ions similar to that reported earlier.[1-5] They have also suggested that above a critical concentration of Mg vacancies (6.25%) these magnetic moments results in collective ferromagnetism.

2.8 Effect of Li Doping in MgO Nanoparticles:

Doping cation or anion of different valancy creates vacancies which can be controlled by varying the amount of dopant. However, doping anion in controlled amount is tedious task

for example doping nitrogen in oxide materials. In contrast, cation doping with controlled stoichiometry can be achieved easily. In this respect MgO is a good candidate as a parent material due to its simple rock salt type structure and highly ionic character. MgO is known to have cation vacancies at the surface. Ferromagnetism in MgO nanoparticles has been shown to be due to neutral metal vacancies which can create holes in the 2p orbital of oxygen. Replacing Mg^{2+} with Li^{+} can be an alternative way to create holes in the 2p orbital of oxygen. We have compared the magnetic properties of undoped and 10 % Li doped MgO nanoparticles.

Figure 13 shows XRD patterns of undoped and 10 % Li doped nanoparticles. Both the samples are well crystalline. No considerable shift in the peak positions due to Li doping could be seen. Peaks of undoped sample are broader which indicates that lithium doping helps in grain growth which has also been reported earlier.[28]

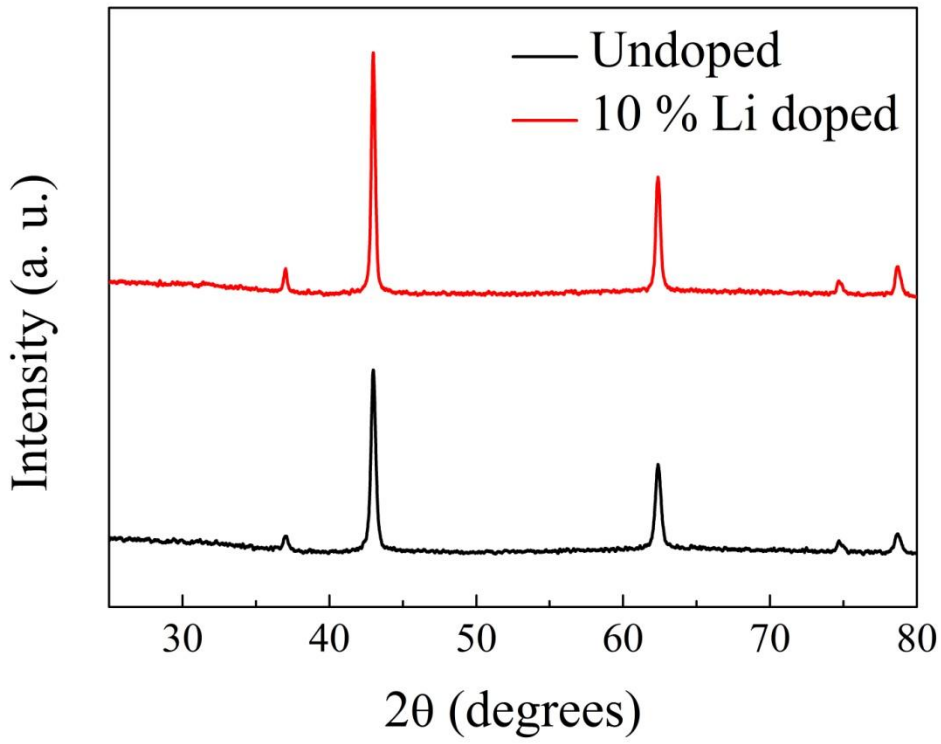

Figure 13 XRD pattern of undoped and 10 % Li doped nanoparticles.

Figure 14 shows the TEM image of 10 % Li doped nanoparticles. Individual grains can be seen in the TEM image with average particle size of around 60 nm. The particles are agglomerated. Inset of Figure 14 shows continuous rings in the electron diffraction pattern which confirms the crystalline nature of sample.

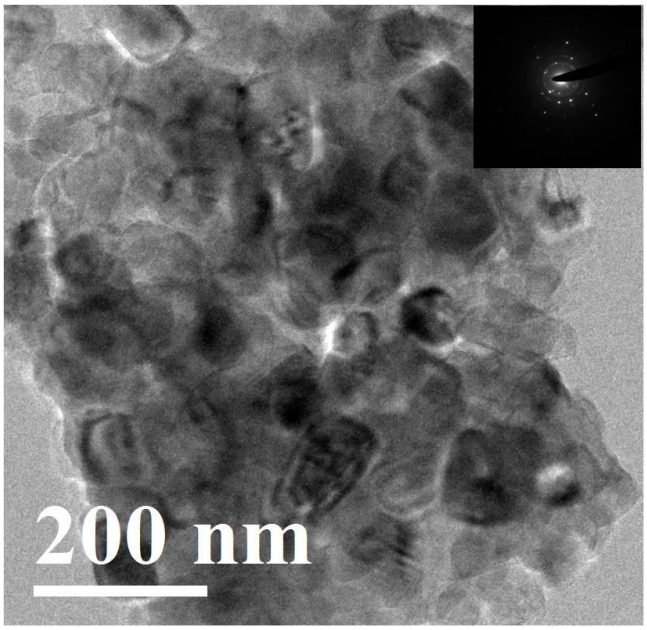

Figure 14 TEM image of 10 % doped Li doped MgO nanoparticles. Inset shows electron diffraction pattern.

Figure 15 shows room temperature magnetization plots for undoped and 10 % Li doped samples. Both the samples show ferromagnetic loops with saturation magnetization of Li doped sample (9 x 10^{-3} emu/g) being double than that of undoped sample (4.7 x 10^{-3} emu/g). Ferromagnetism in MgO nanoparticles has been shown to be due to neutral vacancies present at the surface. These neutral vacancies create holes in oxygen 2p orbitals resulting in the spin polarization near Fermi level.[7-9] In addition to this, substitution of Li^{+} at Mg^{2+} sites may create extra holes in oxygen 2p orbitals. Hence, the magnetization gets enhanced.

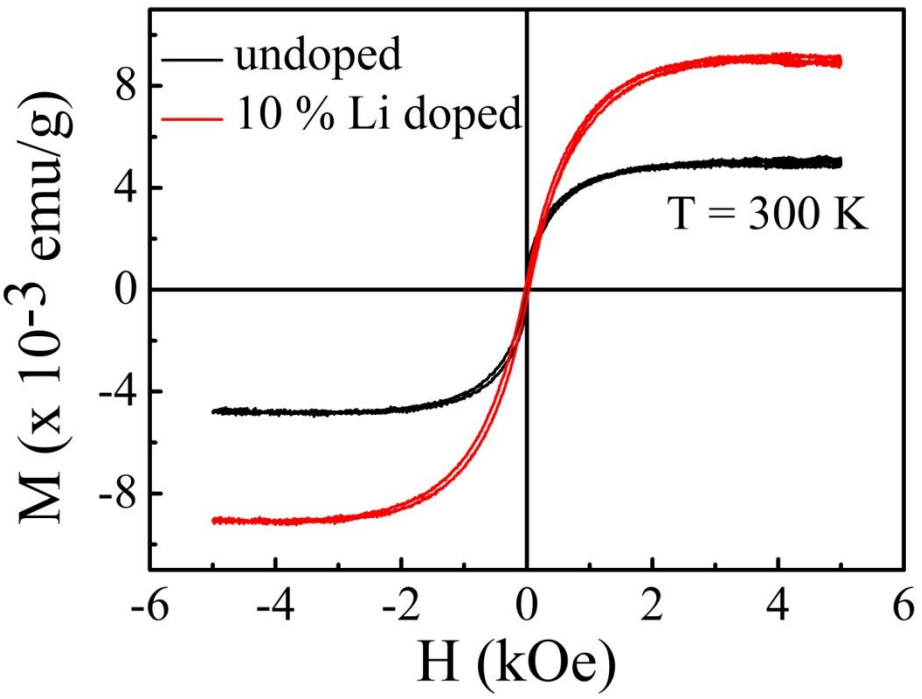

Figure 15 Manetization curves of undoped and 10 % Li doped nanoparticles at room tempeature.

Figure 16 shows photoluminescence spectra of undoped and 10 % Li doped samples. When excited by a light of wavelength 240 nm both doped and undoped samples give a broad luminescent band in the blue region as shown in Figure 16(a). It is interesting to note that luminescent band is red shifted in the case of doped sample as compared to

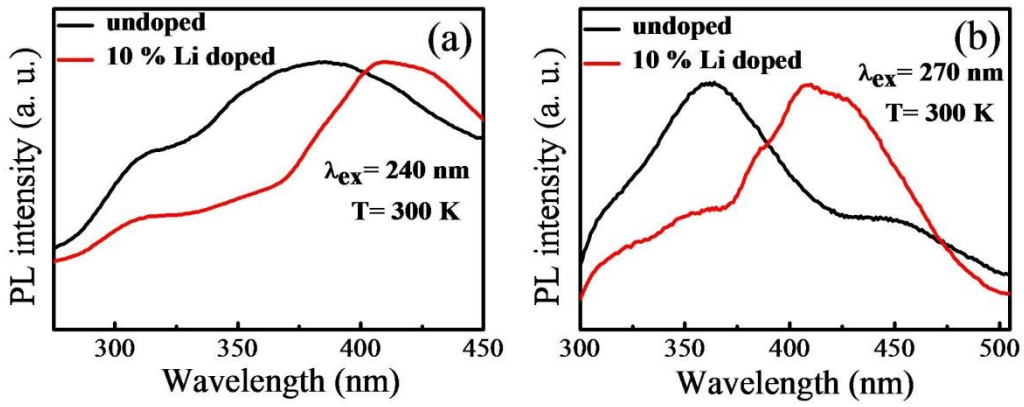

Figure 16 PL spectra of undoped and 10 % Li doped MgO nanoparticles at excitation wavelength of (a) 240 nm and (b) 270 nm.

This kind of band in pure MgO is known for four-fold co-ordinated oxygen atoms. A shift in the doped sample indicates that the defect band is situated lower in energy than that of the undoped sample.

Figure 16(b) shows PL emission band at an excitation wavelength of 270 nm. In pure MgO this band is attributed to three-fold co-ordinated oxygen atoms. The red shift of the band in case of doped sample is even more evident in this case.

2.9 Conclusion:

We studied the nature and concentration of defects using photoluminescence and positron annihilation spectroscopy in ferromagnetic MgO nanoparticles and compared with that of the bulk MgO. The intensity of photoluminescence which is a measure of defect concentration correlates with the decrease of saturation magnetization. Positron annihilation spectroscopy revealed the presence of Mg vacancies whose concentration decrease with increasing particle size.

10 % Li was doped in MgO nanoparticles to study the effect on the magnetic properties. We observed that on doping 10 % Li in MgO nanoparticles, the saturation magnetization becomes double than that of the undoped sample. Shift of defect band towards the lower energy has been observed in photoluminescence spectra.

2.10 References:

(1) Elfimov, I.S.; Yunoki, S.; Sawatzky, G.A. *Phys. Rev. Lett.* **2002**, *89*, 216403.

(2) Osorio-Guille´n, J.; Lany, S.; Barabash, S.V.; Zunger, A. *Phys. Rev. Lett.* **2006**, *96*, 107203.

(3) Gao, F.; Hu, J.; Yang, C.; Zheng, Y.; Qin, H.; Sun, L.; Kong, X.; Jiang, M. *Solid State Commun.* **2009**, *149*, 855.

(4) Wang, F.; Pang, Z.; Lin, L.; Fang, S.; Dai, Y.; Han, S. *Phys. Rev. B* **2009**, *80*, 144424.

(5) Droghetti, A.; Pemmaraju, C. D.; Sanvito, S. *Phys. Rev. B* **2010**, *81*, 092403.

(6) Dirac, P.M.A.; *Proc. Roy. Soc.* **1928**, *117*, 610.

(7) Procházka, I. *Mat. Str*. **2001**, 8, 55.

(8) Puska, J.M.; Nieminen, R.M.; *Rev. Mod. Phys.* **1994**, 66, 841.

(9) Dupasquier, A.; Kögel, G.; Somoza, A. *Acta Mater*. **2004**, *52*, 4707.

(10) Subramania, A.; Kumar, G. V.; Priya, A. R. S.; Vasudevan, T. *Nanotechnology* **2007**, *18*, 225601.

(11) Sanyal, D.; Banerjee, D.; De, U. *Phys. Rev. B* **1998**, *58*, 15226.

(12) Sanyal, D.; Roy, T. K.; Chakrabarti, M.; Dechoudhury, S.; Bhowmick, D.; Chakrabarti A. *J. of Phys. C* **2008**, *20*, 045217.

(13) Mangalam, R. V. K.; Chakrabrati, M.; Sanyal, D.; Chakrabarti, A.; and Sundaresan, A. *J. Phys.: Condens. Matter* **2009**, *21***,** 445902.

(14) Kirkegaard, P.; Pedersen, N. J.; Eldroup, M. *Report of Riso National Lab* **1989**(Riso-M-2740).

(15) Lynn, K. G.; Goland, A. N. *Solid State Commun.* **1976**, *18*, 1549.

(16) Sanyal, D.; Chakrabarti, M.; Roy, T. K.; Chakrabarti, A. *Phys. Lett. A* **2007**, *371*, 482.

(17) Dutta, S.; Chakrabarti, M.; Chattopadhyay, S.; Jana, D.; Sanyal, D.; Sarkar, A. *J. Appl. Phys.* **2005**, *98*, 053513.

(18) Sundaresan, A.; Bhargavi, R.; Rangarajan, N.; Siddesh, U.; Rao, C. N. R. *Phys. Rev. B* **2006**, *74*, 16106.

(19) Stankic, S.; Muller, M.; Diwald, O.; Sterrer, M.; Knozinger, E.; Bernardi, J. *Angew. Chem. Int. Ed.* **2005**, *44*, 4917.

(20) Maclean, S. G.; Duley, W. W. *J. Phys. Chem. Solids* **1984**, *45*, 227.

(21) Anpo, M.; Yamada, Y.; Kubokawa, Y,; Coluccia, S.; Zecchina, A.; Che, M. *J. Chem. SOC., Faraday Trans. I* **1988**, *84*, 751.

(22) Chizallet, C.; Costentin, G.; Pernot, H. L.; Krafft, J. M.; Che, M.; Delbecq, F.; Sautet, P. *J. Phys. Chem. C* **2008**, *112*, 16629.

(23) Saarinen, K.; Suski, T.; Grzegory, I.; Look, D. C.; *Phys. Rev. B* **2001**, *64*, 233201.

(24) Kumar, P. A.; Alatalo, M.; Ghosh, V. J.; Kruseman, A. C.; Nielsen, B.; Lynn, K. G. *Phys. Rev. Lett.* **1996**, *77*, 2097.

(25) Brusa, R. S.; Deng, W.; Karwasz, G. P.; Zecca, A. *Nucl. Instrum. Methods B* **2002**, *194*, 519.

(26) Chakrabarti, M.; Sarkar, A.; Sanyal, D.; Karwasz, G. P.; Zecca, A. *Phys. Lett. A* **2004**, *321*, 376.

(27) Dutta, S.; Chattopadhyay, S.; Sarkar, A.; Chakrabarti, M.; Sanyal, D.; Jana, D. *Prog. Mater. Sci.* **2008**, *54*, 89.

(28) Aritani *et al. J. Phys. Chem. B*, **2000**, *104*, 10133.

CHAPTER 3

Ferromagnetism in Inorganic Hollow Spheres

Summary*

In this chapter, the magnetic properties of inorganic hollow spheres of GaN, $ZnAl_2O_4$ and MgO synthesized using glucose derived amorphous carbon spheres as templates are discussed. Magnetic measurements indicate the presence of ferromagnetism at room temperature in these three types of hollow spheres with especially high value of coercive field in MgO hollow spheres. Photoluminescence (PL) measurements show defect band due to magnesium vacancy in MgO and oxygen vacancy in $ZnAl_2O_4$ hollow spheres which support our prediction of universal ferromagnetism in otherwise nonmagnetic inorganic nanomaterials.

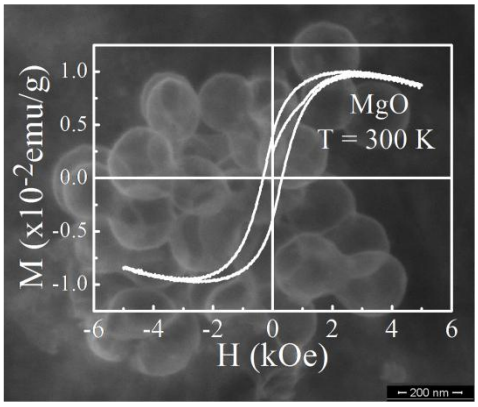

* A paper related to this work has been ***submitted***.

3.1 Introduction:

The fate of future technology relies on the advancement of materials science. Materials with improved properties and applicability are certainly going to fulfil this huge demand. Hollow sphere is one such kind of material which can find its applicability in many emerging fields like gas storage,[1] catalyst support,[2] and drug delivery.[3] Several methods have been employed in order to synthesize inorganic hollow spheres of diverse types in the past. They can broadly be divided into two types: use of hard templates like anodic alumina membrane, amorphous carbon spheres, mesoporous silica etc and soft templates like non-ionic surfactant, polymers, organic ligands etc to synthesize inorganic hollow spheres.[4-14] In addition to these two methods template free synthesis of inorganic hollow spheres is also very popular among chemists which mainly involves Ostwald ripening mechanism.[15-22]

In recent years use of templates is gaining popularity particularly due to the fact that different shapes and sizes of hollow morphologies can be made by choosing appropriate templates. Highly controlled synthesis of templates can be done in labs however, most of them are available commercially. Amorphous carbon spheres as template is unique in a way that after coating with desired material the core can be thermally decomposed into carbon dioxide in the presence of oxygen. The exothermic nature of this reaction provides the required thermal annealing which is very important for high crystallinity, especially for oxide materials. Owing to this fact a range of metal oxides like Fe_2O_3, NiO, Co_3O_4, CeO_2, ZnO, Ga_2O_3, SnO_2, have been prepared in recent past using carbon spheres as template.[23-27]

3.2 Scope of the Present Work:

Surface ferromagnetism in nanoparticles and thin films of otherwise non-magnetic oxide of have been investigated in the recent past. The main disadvantage in such systems is the small value of saturation magnetization. The overall magnetization depends on the defect concentration at the surface. The problem of agglomeration is well known in crystalline oxide materials resulting in the decrease in the concentration of defect sites. In the case of conventional thin films grown on substrates only one side is agglomeration free. Hollow spheres are better option in a way that the inner as well as outer wall is free from agglomeration and thus can be considered as a thin film without any substrate support. Magnetism of such materials will be interesting compared to thin films and nanoparticles owing to the presence of more number of defects.

3.3 Strategy of Carbon Spheres Synthesis:

Carbohydrates like glucose, fructose, sucrose, maltose, cyclodextrin, starch and cellulose as precursors for the synthesis of carbon spheres are used due to their low cost and high abundance in nature.[28-32] The synthesis requires heating of aqueous solution of

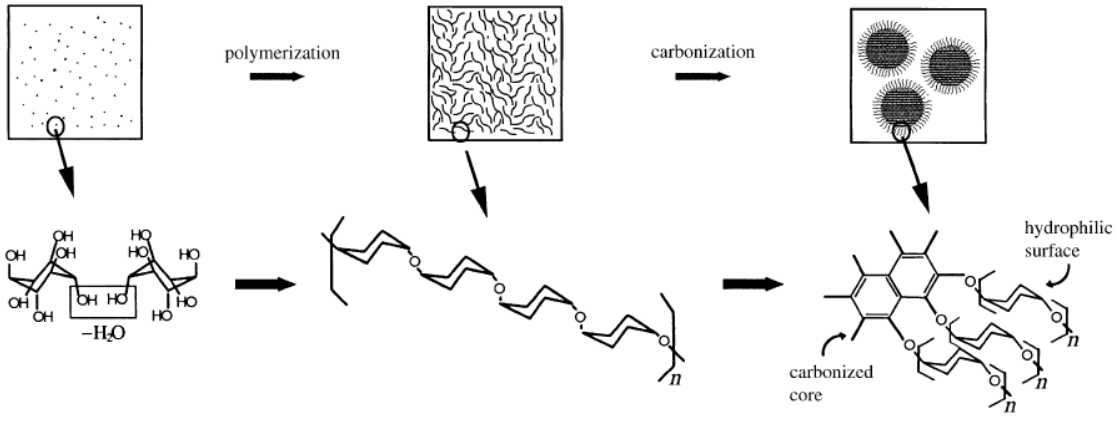

Figure 1 Schematic for the processes involved in carbon spheres synthesis from glucose.

carbohydrates in closed containers at 160 to 180 ^{o}C for 6 to 24 hours. When the reaction temperature is kept higher than glycosidation temperature then first polymerization of carbohydrate takes place followed by carbonization. These processes result in the condensation of functional groups in the core while the surface still retains these groups due to the incomplete polymerization.

Strategy for the synthesis of metal oxide using carbon spheres as template involves mainly two steps:

- Adsorption of metal ions on the surface of carbon spheres. A large amount of metal ions can be adsorbed on the surface because of the presence of oxygen containing functional groups. The amount of metal ions determines the thickness of hollow sphere.
- Calcination of the composite spheres in oxygen to remove the carbon core, which results in oxide hollow spheres.

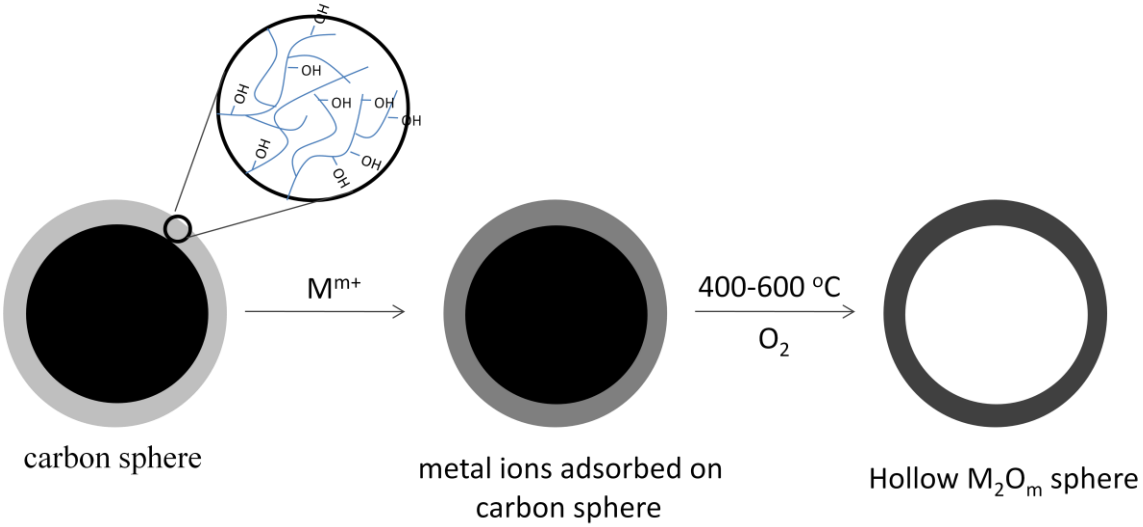

Figure 2 Strategy for the formation of metal oxide hollow spheres

3.4 Experimental Procedure:

3.4.1 Materials:

Anhydrous D (+) Glucose (Dextrose, Corn Sugar) and Gallium Oxide were purchased from Sigma-Aldrich. Analytical grade $Zn(NO_3).6H_2O$, $Al(NO_3)_3.9H_2O$, $Mg(NO_3)_2.6H_2O$ and 30% aq. NH_3 solution were purchased from Qualigens. All the chemicals mentioned above were used directly without further purification. The water used in the experiments was obtained from Millipore purification system and had a resistivity as high as 18 MΩ-cm. Calcination was done on an alumina boat in a muffle furnace (Elite Thermal Systems, UK). Tube furnace (Elite Thermal Systems, UK) was used for heating the sample in gaseous NH_3 (99.99% purchased from Chemix gases, India).

3.4.2 Synthesis of Carbon Spheres:

5 g of glucose was dissolved in 50 mL of water to form a clear solution. It was placed in a 60 mL Teflon sealed stainless steel container and heated at 180 ^oC for 12 h. The brown product was isolated and purified by repeated washing with ethanol after which the samples were dried at 80^oC for 4 h. The as-synthesized carbon spheres were used as templates to synthesize the inorganic hollow spheres.

3.4.3 Synthesis of $ZnAl_2O_4$ hollow spheres:

4.65 g of $Zn(NO_3)_2.6H_2O$ and 11.63 g of $Al(NO_3)_3.9H_2O$ were dissolved in 30 mL of water. The carbon spheres (0.25 g) were added to the above solution and the whole mixture was sonicated for 15 min, followed by 12 h of aging. The supernatant solution

was decanted out and the black residue obtained was centrifuged five times with water and ethanol. The pH was adjusted to 8-10 by adding 30% aqueous NH_3 solution. The mixture was transferred to a 20 mL teflon lined stainless steel autoclave and maintained at 180 ^oC for 20 h after which it was allowed to air cool to room temperature. The supernatant was decanted out and the residue obtained was washed with ethanol and dried at 80 ^oC for 3 h. The template was finally removed by heating at 600 ^oC for 5 h in air.

3.4.4 Synthesis of GaN hollow spheres:

GaN hollow spheres were synthesized according to a reported procedure.[26] The precursor of gallium was $GaCl_3$ which was prepared by dissolving 0.4 g of Ga_2O_3 in 10 mL of hot HCl. 0.25 g of carbon spheres was soaked in the HCl solution for over 12 h. This was followed by washing the sample twice in water followed by drying at 80 ^oC for 4 h. The gallium adsorbed carbon spheres was finally calcined at 500 ^oC for 5 h. The as prepared Ga_2O_3 hollow spheres were heated in the presence of NH_3 at 800 ^oC for 3 h.

3.4.5 Synthesis of MgO hollow spheres:

12.84 g of $Mg(NO_3)_2$.6H2O was dissolved in 50 mL water. 1.2 g of carbon spheres was added to this solution. The resultant mixture was sonicated for 1 hour followed by 24 hours of aging. The content was centrifuged and washed with water. Final washing was done with ethanol followed by drying at 80 ^oC for 4 h. Magnesium adsorbed carbon spheres was heated at 500 ^oC for 4 hours in oxygen atmosphere to get MgO hollow spheres.

3.4.6 Characterization:

The morphology was analyzed using a Field emission scanning electron microscope (FESEM) Nova nano (The Netherlands) in high vacuum mode by dispersing the samples in ethanol. Transmission electron microscope (TEM) images were recorded with a JEOL JEM 3010 instrument (Japan) operated with an accelerating voltage of 300 kV. X-ray diffraction (XRD) characterization was done at 25 ^{o}C with Bruker D8 instrument (Germany) diffractometer employing Cu K_{α} radiation. Magnetic measurements were carried out using a physical property measurements system (Quatnum Design, USA). The magnetic moment measurements were performed at 300 K over a field range of 2 T. PL spectra were recorded in PERKIN–ELMER LS 55 Luminescence Spectrometer in solid mode.

3.5 Results and Discussions:

3.5.1 Morphology:

Figure 3 shows FESEM image of carbon spheres. Diameters are marked for selected spheres. Average diameter of carbon spheres is ~700 nm.

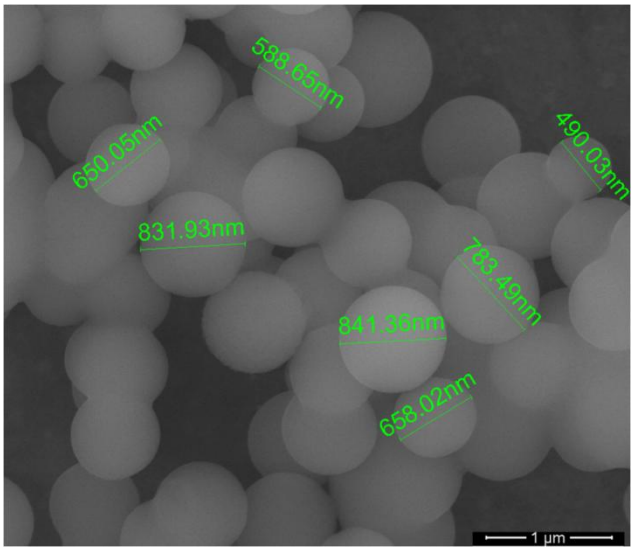

Figure 3 FESEM image of carbon spheres

Figure 4 (a) shows the TEM image of GaN hollow spheres. Enlarged image of an individual sphere is shown in Figure 4(b). Average diameter of GaN hollow spheres is ~ 300 nm with the wall thickness of around 20 nm. It is clear from these images that the spheres are polycrystalline in nature. Nanoparticles are actually connected in two dimensions to form hollow spheres.

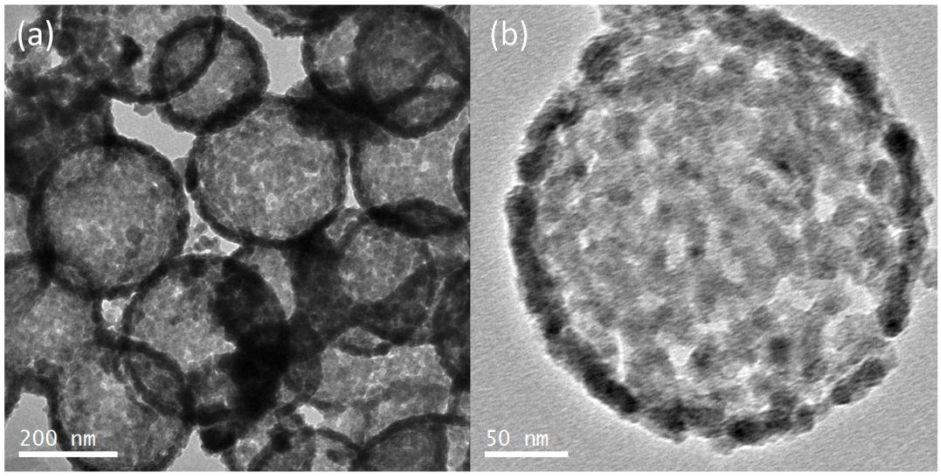

Figure 4(a) TEM images of GaN hollow spheres, (b) TEM image of an individual GaN hollow sphere.

TEM images of $ZnAl_2O_4$ hollow spheres are shown in fig. 5(a) and (b). Like GaN hollow spheres these are polycrystalline in nature but not as porous as in the case of GaN. Average diameter is ~ 120 nm while the wall thickness is around 20 nm.

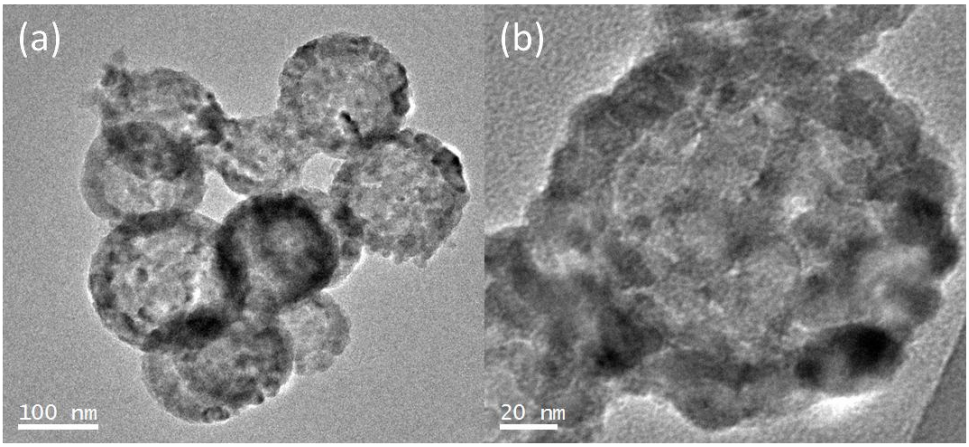

Figure 5(a) TEM image of $ZnAl_2O_4$ hollow spheres, (b) TEM image of an individual hollow sphere.

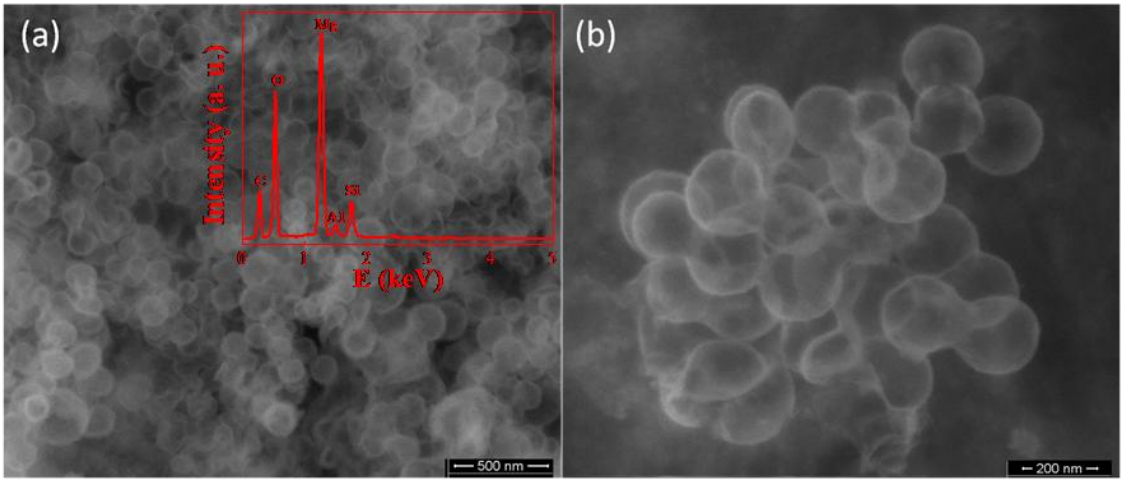

Figure 6(a) FESEM image of MgO hollow spheres with EDAX in the inset, (b)Higher resolution FESEM image of MgO hollow spheres.

Figure 6(a) shows FESEM image of MgO hollow spheres with EDAX shown in inset. The more magnified image is shown in figure 6(b). As can be seen clearly, that

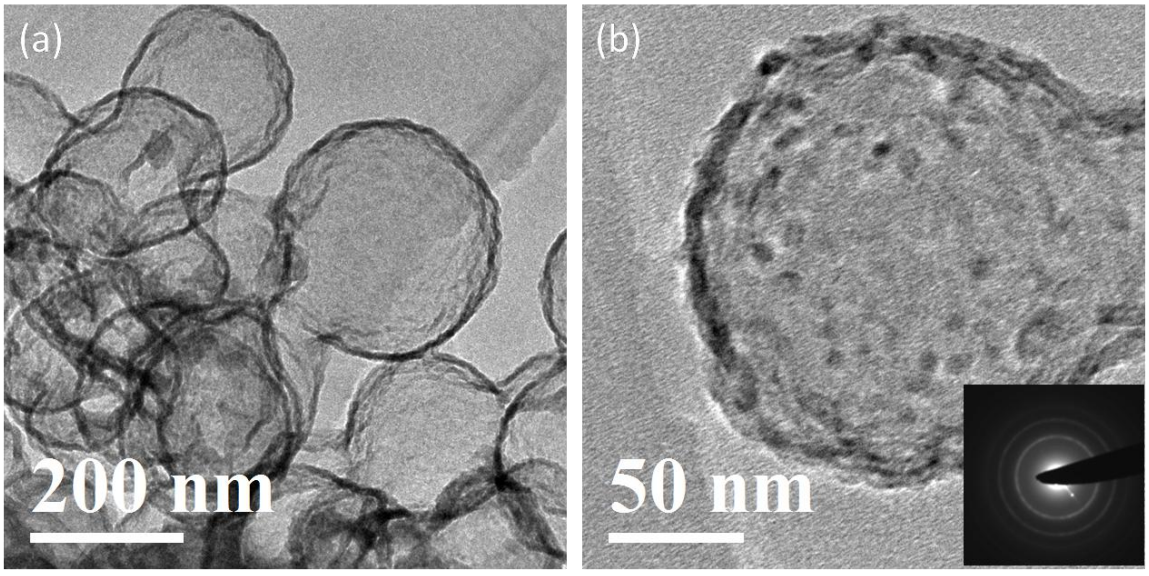

Figure 7(a) TEM image of MgO hollow spheres, (b) TEM image of an individual MgO hollow sphere. Inset shows electron diffraction pattern.

thickness of the wall is very less. Exact thickness of these hollow spheres can be predicted from TEM images shown in Figure 7(a) and (b). Thickness of MgO spheres is around 8 nm. Figure 7(b) shows enlarged image of an individual sphere where small grains can easily be seen. Electron diffraction pattern shown in the inset of Figure 5(b)

contains continuous rings which further indicate the polycrystalline nature of MgO hollow spheres.

3.5.2 XRD Analysis:

Figure 8(a) shows XRD image of GaN prepared at 800 ^{o}C. Asterisk marked peaks are of β Ga_2O_3 impurity phase which exist along with the desired hexagonal phase of GaN. The absence of any peak due to impurity phase for the sample prepared at 850 ^{o}C indicates the fact that the formation of GaN hollow spheres is complete at this temperature which is shown in Figure 8(b). The pattern matches with the hexagonal phase (space group $P6_3mc$.)

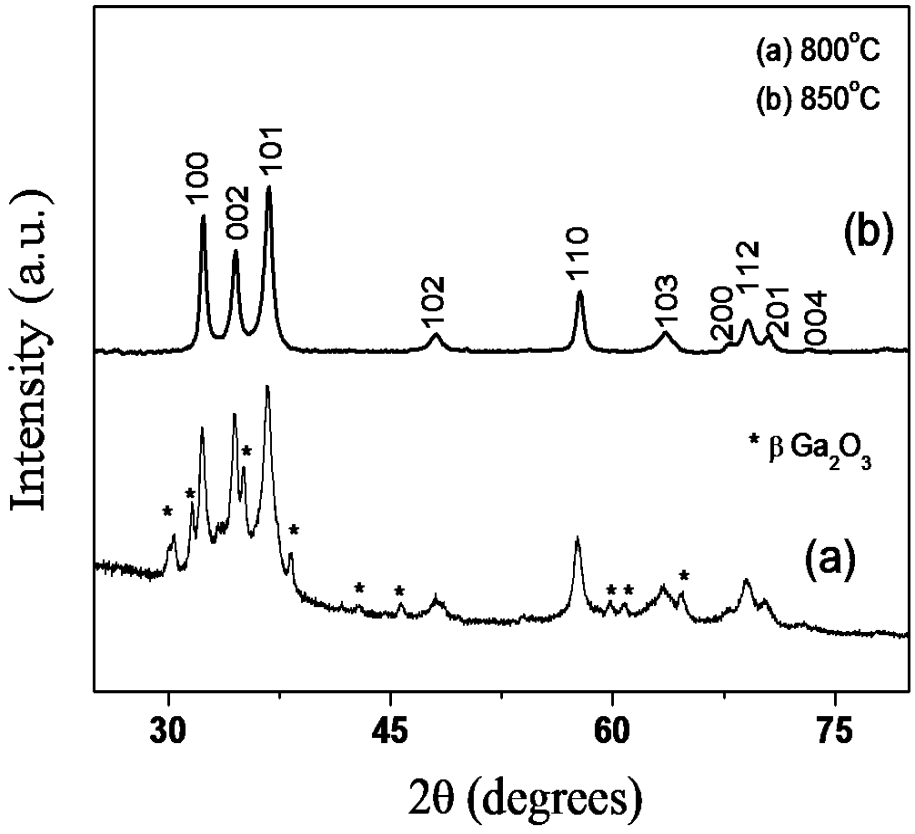

Figure 8(a) XRD pattern of GaN hollow spheres heated at 800 ^{o}C and (b) 850 ^{o}C

XRD pattern of MgO hollow spheres is shown in Figure 9. Broadening of the peaks can be attributed to the small crystallite size of MgO which has been seen in the TEM images.

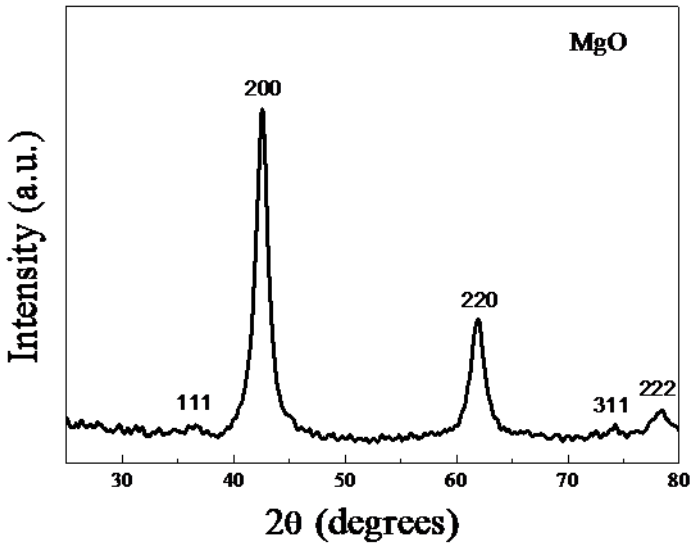

Figure 9 XRD pattern of MgO hollow spheres.

It crystallizes in rock salt structure with cubic space group Fm-3m.

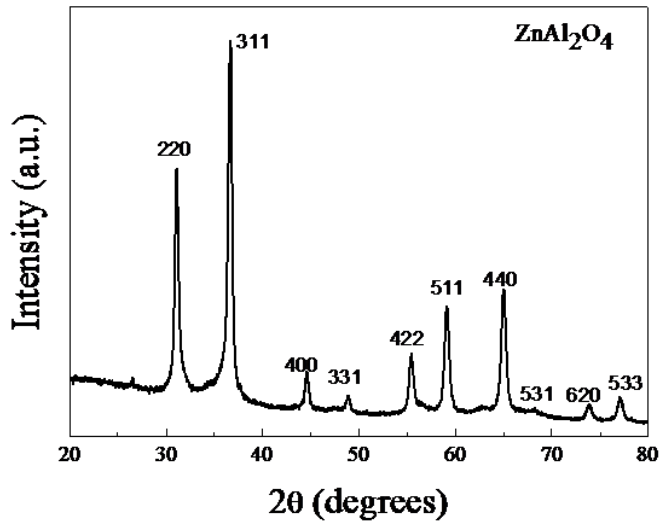

Figure 6 XRD pattern of $ZnAl_2O_4$ hollow spheres.

XRD pattern of $ZnAl_2O_4$ shown in Figure 10 is consistent with cubic phase (space group Fd-3m) without any Al_2O_3 or ZnO impurity phase. $ZnAl_2O_4$ has normal spinel structure with Zn^{2+} being at the tetrahedral sites, while all the Al^{3+} at the octahedral sites.

3.5.3 Magnetic Properties:

Figure 11 shows magnetization as a function of magnetic field at room temperature for GaN hollow spheres. The sample shows a ferromagnetic hysteresis loop with large saturation magnetization value of 0.032 emu/g, that is one order higher than the previous report[33] of ferromagnetism in GaN nanoparticles. The plot has been corrected for the diamagnetic behaviour of the core of the nanoparticles as well as for background diamagnetism.

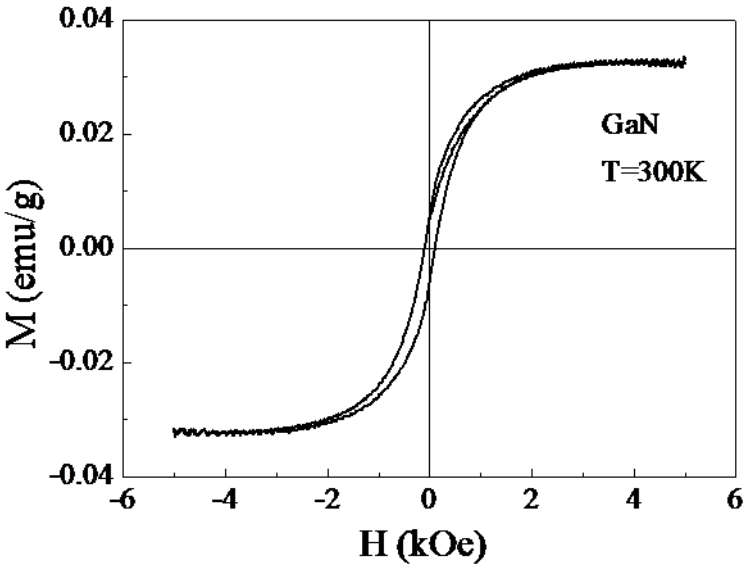

Figure 11 Room temperature magnetization of GaN hollow spheres.

This high value of saturation magnetization can be attributed to the fact that the crystallites in hollow spheres are at least not agglomerated from two sides. It has been shown earlier that agglomeration leads to the reduction of surface ferromagnetism due to

the decrease in the concentration of defect sites.[34] The value of coercive field is more or less same as compared to the nanocrystalline GaN powder indicating the fact that there is not much interaction among grains constituting the hollow sphere. DFT calculations have shown that Ga vacancies are actually responsible for magnetization in GaN.[35] The report further claims that Ga vacancies not only create local magnetic moments but also lead to long range magnetic ordering.

Figure 12 shows the ferromagnetic hysteresis loop of $ZnAl_2O_4$ hollow spheres. Bulk $ZnAl_2O_4$ is diamagnetic as there are no magnetic ions present in the compound. Magnetic properties of $ZnAl_2O_4$ in any form have not been reported earlier. After diamagnetic correction it shows a saturation magnetization value of 4.67 emu/g.

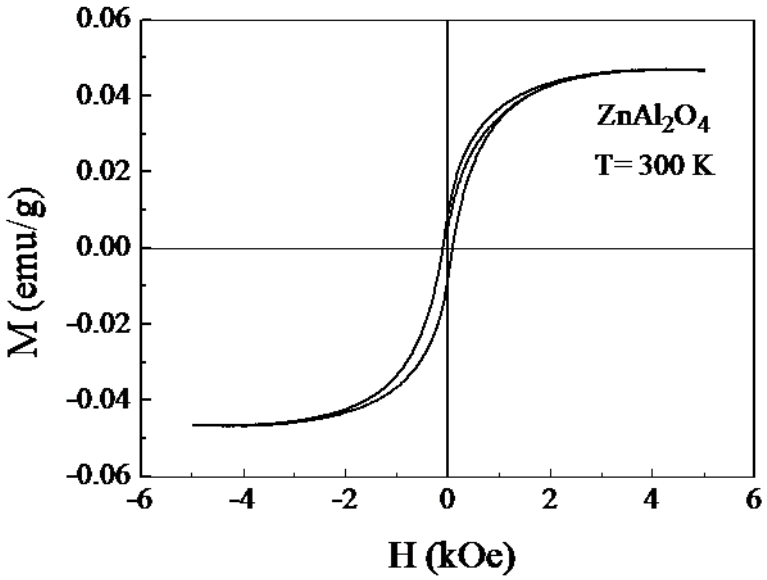

Figure 12 Room temperature magnetization of ZnAl2O4 hollow spheres.

In a very similar spinel nanoparticles system of $MgAl_2O_4$ it has been shown using ^{27}Al NMR that concentration of five and three fold coordinated Al at the surface increases

with decrease in particle size.[36] A similar kind of mechanism in $ZnAl_2O_4$ might play an important role in imparting ferromagnetism.

Hysteresis loop of MgO hollow spheres at room temperature is shown in Figure 13. The coercive field of 300 Oe is significantly higher than the previously reported ferromagnetism in MgO nanoparticles.[34] The large value of coercive field may be attributed to magnetic anisotropy due to the shape of the hollow spheres.

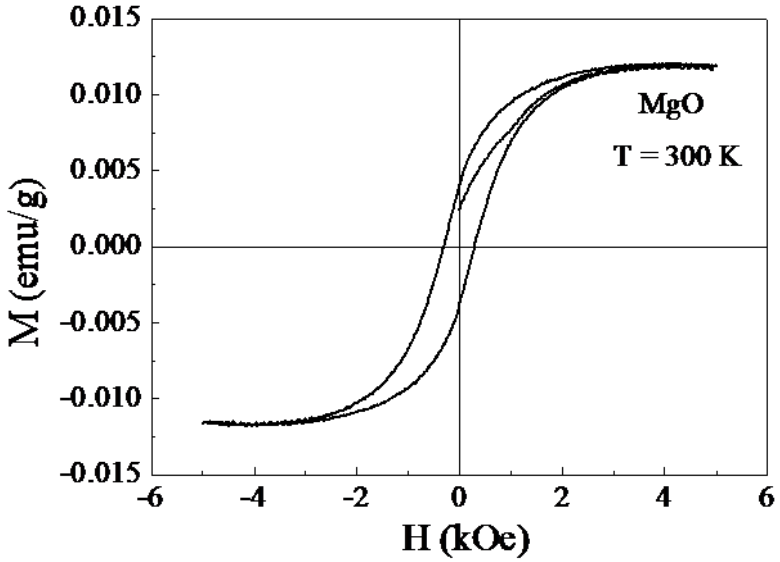

Figure 13 Room temperature magnetization of MgO Hollow spheres.

MgO vacancies at the surface of nanocrystallites give rise to ferromagnetism at room temperature. This has been supported experimentally by positron annihilation and photoluminescence spectroscopy[34] in the recent past. First principle based calculations[37, 38] show that the magnetic moments in MgO arise from spin polarization of 2p orbitals of oxygen surrounding neutral Mg vacancies.

3.5.4 Photoluminescence Spectroscopy:

Photoluminescence spectroscopy is a very useful tool to identify defects. Figure 14(a) and (b) show PL spectra of MgO hollow spheres at two excitations 240 nm and and 270 nm respectively. These are the energies much less than the band gap (7.8 eV) of MgO. Broad spectra concentrated in the blue region (around 410 nm) can then be attributed to the emission from the defect levels in MgO. In the literature peaks corresponding to 240 nm and 270 nm excitations have been attributed to four coordinated oxygen at the edge and three coordinated oxygen at the corners respectively in MgO lattice.[39]

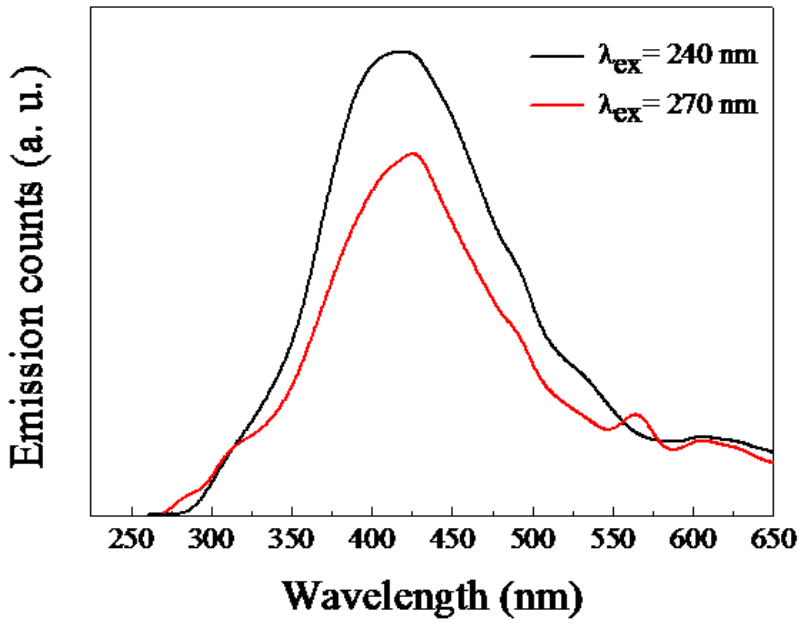

Figure 14 PL spectra of MgO hollow spheres

Figure 15 shows PL spectrum of $ZnAl_2O_4$ hollow spheres. A broad peak at 500 nm is observed when excited by light of wavelength 360 nm which is less than its band gap (3.8 eV). Such kind of PL spectra for $ZnAl_2O_4$ nanoparticles have been observed earlier and have been attributed to oxygen vacancies.[40]

.

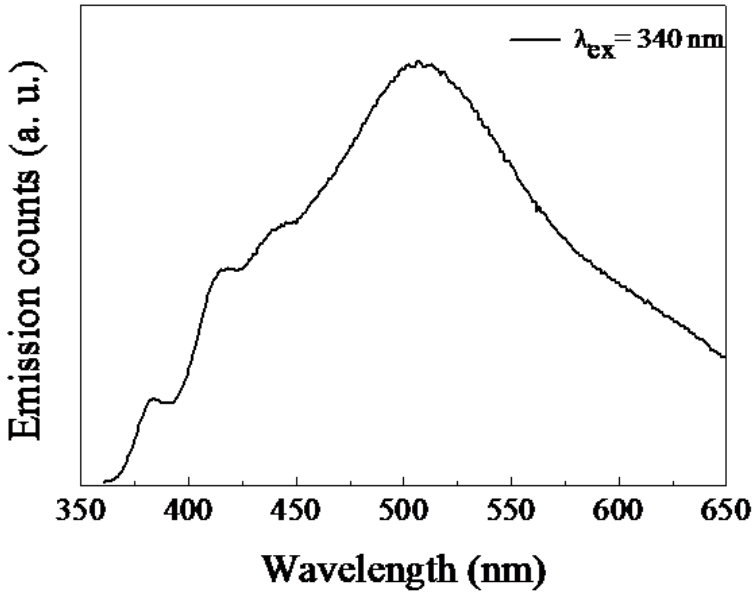

Figure 15 PL spectrum of $ZnAl_2O_4$ hollow spheres.

PL spectrum of GaN hollow spheres is shown in Figure 16 with 325 nm excitation. The emission spectrum shows a broad peak corresponding to band edge absorption. The broadening is due to the fact that GaN crystallites are not mono-disperse and it is well known that band gap of large band gap semiconductors does depend on crystallite size. In addition to this a broad band corresponding to yellow emission (~ 560 nm) has been observed in epitaxial thin films and nanoparticles.[41, 42] The origin of this band is not is not clear but there are evidences of extended defects like dislocations and stacking fault contributing towards this. On the other hand theory suggests that ferromagnetism in GaN should come from Ga vacancy. Hence in our GaN hollow spheres PL measurements are not providing any further support to the ferromagnetism observed.

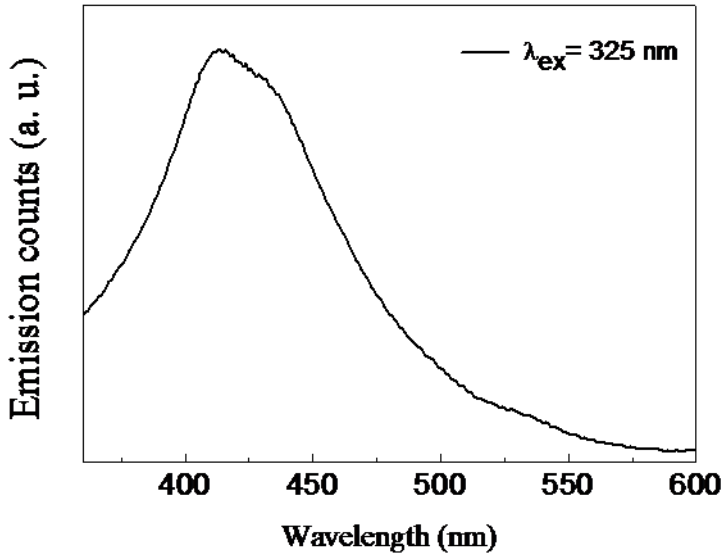

Figure 16 PL spectrum of GaN hollow spheres.

3.6 Conclusions:

We synthesized polycrystalline hollow spheres of GaN, $ZnAl_2O_4$ and MgO using carbon spheres as template. TEM and XRD analysis were carried out in order to characterize the hollow spheres systematically. GaN hollow spheres show enhanced magnetic property in terms of large value of saturation magnetization when compared to the previous report in GaN nanoparticles. We attribute this property to the fact that these hollow spheres are agglomeration free from at least two sides. Hollow spheres of $ZnAl_2O_4$ show a nice ferromagnetic hysteresis loop with large saturation magnetization possibly due to the point defect sites at the surface. Hysteresis loop of MgO hollow spheres show a large coercive field which indicates an increase in anisotropy coming due to its shape. PL measurements support point defects related origin of ferromagnetism in MgO and $ZnAl_2O_4$ hollow spheres while in the case of GaN hollow spheres PL

measurements are not sufficient enough to show Ga vacancy, which has been shown to be the origin of ferromagnetism in GaN using first principle calculations.

3.7 References:

(1) Jiang, J.; Gao, Q.; Zheng, Z. Xia, K.; Hu, J. *Int. J. Hydrogen Energy* **2010**, *35*, 2106.

(2) Li, J.; Xu, Y.; Wu, D.; Sun, Y. *Catalysis Today*, **2010**, *148*, 148.

(3) Zhao, W.; Chen, H.; Li, Y.; Li, A.; Lang, M.; Shi, J. *Adv. Funct. Mater.* **2008**, *18*, 278088.

(4) Caruso, F.; Caruso, R. A.; Möhwald, H. *Science,* **1998**, *282*, 1111.

(5) Kobayashi, S.; Hamasaki, N.; Suzuki, M.; Kimura, M.; Shirai, H.; Hanabusa, K. *J. Am. Chem. Soc.*, **2002**, *124*, 6550.

(6) Göltner, C. G. *Angew. Chem. Int. Ed*., **1999**, *38*, 3155.

(7) Sun Y.; Xia, Y. *Science*, **2002**, *298*, 2176.

(8) Sun, Y.; Mayers, B.; Xia Y. *Adv. Mater.*, **2003**, *15*, 641.

(9) Nakashima, T.; Kimizuka, N. *J. Am. Chem. Soc.*, **2003**, *125*, 6386.

(10) Guo, C.-W.; Cao, Y.; Xie, S.-H.; Dai, W.-L.; Fan, K.-N. *Chem. Commun.*, **2003**, 700.

(11) Dinsmore, A. D.; Hsu, M. F.; Nikolaides, M. G.; Marquez, M.; Bausch, A.R. Weitz, D. A. *Science*, **2002**, *298*, 1006.

(12) Caruso, R. A.; Schattka, J. H.; Greiner, A. *Adv. Mater.*, **2001**, *13*, 1577.

(13) Yang, Z.; Niu, Z.; Lu, Y.; Hu, Z.; Han, C. C. *Angew. Chem. Int. Ed.*, **2003**, *42*, 1943.

(14) Zhu, J. J.; Xu, S.; Wang, H.; Zhu, J. M.; Chen, H. Y. *Adv. Mater.*,**2003**, *15*, 156.

(15) Yin, Y.; Rioux, R. M.; Erdonmez, C. K.; Hughes, S.; Somorjai, G. A.; Alivisatos, A. P. *Science*, **2004**, *304*, 711.

(16) Liu, B.; Zeng, H. C. *J. Am. Chem. Soc.*, **2004**, *126*, 16744.

(17) Chang, Y.; Lye, M. L.; Zeng, H. C. *Langmuir*, **2005**, *21*, 3746.

(18) Yang, H. G.; Zeng, H. C. *J. Phys. Chem. B*, **2004**, *108*, 3492.

(19) Liu, B.; Zeng, H. C. *Small*, **2005**, *1*, 566.

(20) Chang, Y.; Teo, J. J.; Zeng, H. C. *Langmuir*, **2005**, *21*, 1074.

(21) Teo, J. J.; Chang, Y.; Zeng, H.C. *Langmuir*, **2006**, *22*, 7369.

(22) Li, J.; Xu, Y.; Wu, D.; Sun, Y. *Catalysis Today*, **2010**, *148*, 148.

(23) Jagadeesan, D.; Mansoori, U.; Mandal, P.; Sundaresan, A.; Eswaramoorthy, M. *Angew. Chem. Int. Ed.* **2008**, *47*, 7685.

(24) Titirici, M. M.; Antonietti, M.; Thomas, A. *Chem. Mater.* **2006,** *18*, 3808.

(25) Wang, X.; Hu, P.; Fangli, Y.; Yu, L. *J. Phys. Chem. C* **2007**, *111*, 6706.

(26) Sun, X.; Li, Y. *Angew. Chem. Int. Ed.* **2004**, *43*, 3827.

(27) Yin, X. M.; Li, C. C.; Zhang, M.; Hao, Q. Y.; Liu, S.; Li, Q. H.; Chen, L. B.; Wang, T. H. *Nanotechnology* **2009**, *20*, 455503.

(28) Wan, W.; Min, Y. L.; Yu, S. H. *Langmuir* **2008**, *24*, 5024.

(29) Yu, S. H.; Cui, X.; Li, L.; Li, K.; Yu, B.; Antoneitti, M.; Colfen, H. *Adv. Mater.* **2004**, *16*, 1636.

(30) Zheng, M.; Cao, J.; Chang, X.; Wang, J.; Liu, J.; Ma, X. *Mater. Lett.* **2006**, *60*, 2991.

(31) Yao, C.; Shin, Y.; Wang, L. Q.; Windisch, C. F.; Samuels, W. D.; Arey, B. W.; Wang, C.; Risen Jr, W. M.; Exarhos, G. J. *J. Phys. Chem. C* **2007**, *111*, 15141.

(32) Dinesh, J.; Eswaramoorthy, M. *Chem. Asian J.* **2010**, *5*, 232.

(33) Madhu, C.; Sundaresan, A.; Rao, C.N.R. *Phys. Rev. B* **2008**, *77*, *201*,306.

(34) Kumar, N.; Sanyal, D.; Sundaresan, A. *Chem. Phys. Lett.* **2009**, 477, 360.

(35) Dev, P.; Xue, Y.; Zhang, P. *Phys. Rev. Lett.* **2008**, 100, 117204.

(36) Sreeja, V.; Smitha, T. S.; Nand, D.; Ajithkumar, T. G.; Joy, P. A. *J. Phys. Chem. C* **2008**, 112, 14737.

(37) Gaoa, F.; Hu, J.; Yang, C.; Zheng, Y.; Qin, H.; Sun, L.; Kong, X.; Jiang, M. *Solid State Commun.* **2009**, *149*, 855.

(38) Wang, F.; Pang, Z.; Lin, L.; Fang, S.; Dai, Y.; Han, S. *Phys. Rev. B* **2009**, *80*, 144424.

(39) Stankic, S.; Muller, M.; Diwald, O.; Sterrer, M.; Knozinger, E.; Bernardi, J. *Angew. Chem. Int. Ed.* **2005**, 44, 4917.

(40) Da Silva, A. A.; Goncalves, A. S.; Davolos, M. R. *J Sol-Gel Sci. Technol.* **2009**, 49, 101.

(41) Liu, R.; Bell, A.; Ponce, F. A.; Chen, C. Q.; Yang, J. W.; Khan, M. A. *Appl. Phys. Lett.* **2005**, 86, 021908.

(42) Ponce, F. A.; Cherns, D.; Young, W. T.; Steeds, J. W. *Appl. Phys. Lett.* **1996**, 69, 770.

CHAPTER 4

Multiferroic Properties of $Bi_4Ti_3O_{12}$ Nanoparticles

Summary

The chapter deals with the multiferroic property of bismuth titanate ($Bi_4Ti_3O_{12}$) nanoparticles. Core of the nanoparticles remains ferroelectric while the surface due to the presence of point defects exhibit ferromagnetism. Ferromagnetic as well as ferroelectric hysteresis loops have been observed at room temperature. Decay of ferromagnetism with increase in particle size has also been discussed.

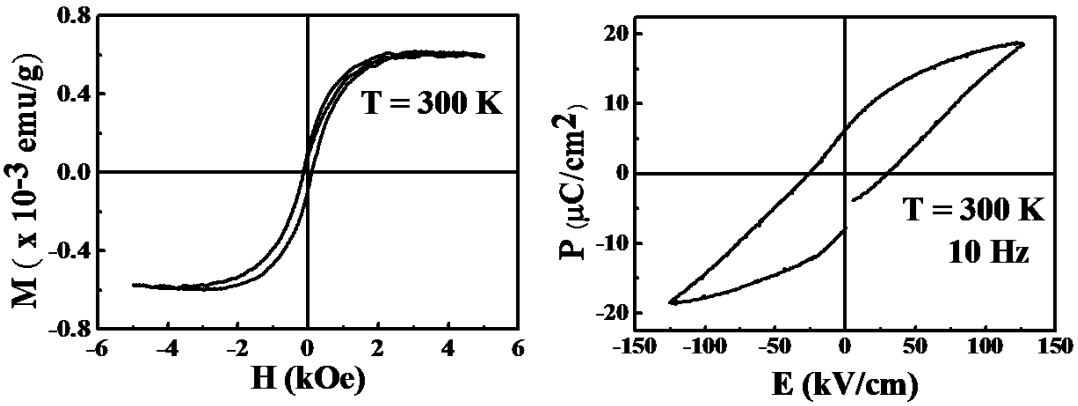

4.1 Introduction:

Multiferroics is a fascinating subject not only because it entails rich physics but mainly due to its wide variey of applications in memory cells, transducers, actuators, highly sensitive magnetoelectric sensors, spintronics devices, robotics, and devices for medicine applications.[1-18] A multiferroic material should have at least two of the ferroic properties coupled to each other namely ferro- or antiferromagnetism, ferroelectricity and ferroelasticity. Among them, the class of multiferroic materials with coupled magnetic and electrical properties are most important. Such materials find many applications because magnetic property can be manipulated by changing the electrical variables and vice –versa.

In the classical case, for a substance to have ferroelectricity its d orbital should be empty whereas partially filled d orbital is a prerequisite for magnetism. Hence, it is very difficult to find both the properties in a single material.[19] The recent surge in this field is mainly driven by the quest to search materials with ferroelectricity due to some mechanism other than d^0 ness. $BiFeO_3$ is an interesting example the only one known at room temperature where ferroelectricity appears due to stereo-chemical activity of Bi lone electron pair.[19-22] In recent years ferroelectricity due to spiral spin ordering has also been exploited for designing multiferroic materials such as $TbMnO_3$, $CoCr_2O_4$ *etc.*[23-35]

The other way of dealing with this subject is to find alternative route for magnetism. In the past few years surface magnetism in nanoparticles of otherwise nonmagnetic materials have been investigated with great interest. Such kind of magnetism, although weak compared to conventional magnetism, has been tapped to come up with new types of multiferroic materials. $BaTiO_3$ which is known to be

ferroelectric has been shown to exhibit multiferroic property with positive magnetocapacitance near ferroelectric transition temperature.[36]

4.2 Scope of the Present Work:

Bismuth titanate ($Bi_4Ti_3O_{12}$) as a ferroelectric material is interesting because of its very high ferroelectric transition temperature (675 ^oC). $Bi_4Ti_3O_{12}$ is a member of the Aurivillius family of bismuth layer structure perovskites, which consist of layers of perovskite-like units sandwiched between bismuth oxide ($(Bi_2O_2)^{2+}$) layers.[38] This crystal structure promotes a plate like morphology with the $(Bi_2O_2)^{2+}$ layers in the *ab*-plane, parallel to the plane of the platelets.

Present work deals with the multiferroic behaviour of $Bi_4Ti_3O_4$ nanoparticles which is otherwise only ferroelectric in the bulk form. Magnetic part of the ferroelectric comes from the defects present on the surface of nanoparticles.

4.3 Experimental Procedure:

The $Bi_4Ti_3O_{12}$ nanoparticles were synthesized by following a reported procedure at room temperature by chemical coprecipitation.[39] Titanium iso-propoxide ($(C_4H_9O)_4Ti$ Sigma-Aldrich, 97 %) was added into de-ionized water to synthesize the H_2TiO_3 compound. Then plenty of aqueous ammonia (28 wt.% of NH_4OH) was added to H_2TiO_3 and stirred for 20 minutes to form $(NH_4)_2TiO_4$ solution. H_2O_2 was used as oxidant to make the H_2TiO_3 powders resolve. The obtained $(NH_4)_2TiO_4$ solution was slowly poured into the acidic $Bi(NO_3)_3$ solution which was prepared by dissolving Bi_2O_3 (Sigma-Aldrich, 99.9 %) in concentrated HNO_3 (and the mixture was vigorously stirred until the reaction was over. Finally, the resulting precipitate was centrifuged and repeatedly

washed with deionized water, followed by drying at 80 ^{o}C. The dry as prepared sample was then annealed at various temperatures in oxygen atmosphere for 2 h. Bulk sample was prepared by sintering a well palletized disk in air at 1100 ^{o}C for 24 h. For ferroelectric measurements the nanoparticles sample was palletized and heated at 900 ^{o}C for 20 minutes.

4.4 Characterization:

For X-ray diffraction (XRD), samples were properly ground and levelled on a quartz sample holder in order to avoid any height mismatch within the sample space. XRD patterns were recorded with a Rigaku-99 Miniflex II diffractometer using Cu Ka radiation (k = 1.5406 Å).

Particle size and morphology were analyzed by Field Emission Scanning Electron Microscopy (FESEM) using NOVA NANOSEM 600 (FEI, Netherlands). For FESEM, small amount of sample was dispersed in alcohol and drops of this dispersion were taken on aluminium stub and then evaporated before irradiating it with electron beam. High vacuum mode was used for taking FESEM images to prevent air scattering.

Magnetic measurements were carried out with vibrating sample magnetometer in Physical Properties Measurement System (PPMS, Quantum Design, USA). Rectangular pellets of dimension 6 mm x 3 mm were hydraulically pressed. The pellet was mounted in quartz sample holder and wrapped with brown tape both provided by Quantum Design. For background correction magnetic measurement of sample holder and brown tape only were carried out.

Ferroelectric measurements were done using Radiant Technologies Precision Workststion. Electrodes were given by polishing the pellet with silver on both sides.

4.5 Results and Discussion:

Figure 1 shows XRD patterns of $Bi_4Ti_3O_{12}$ particles prepared by heating the as prepared sample at different temperatures. The sample heated at 450 ^oC shows broad XRD peaks, characteristic of nanoparticles (shown in Figure 1(a)). At this temperature $Bi_4Ti_3O_{12}$ crystallizes in tetragonal structure (space group I4/mmm) because of the surface energy of nanoparticles. However, in the bulk form orthorhombic structure (ferroelectric phase) is more favourable structure (space group B2cb). When the bulk sample heated, at 675 ^oC the structure transforms to paraelectric tetragonal structure.

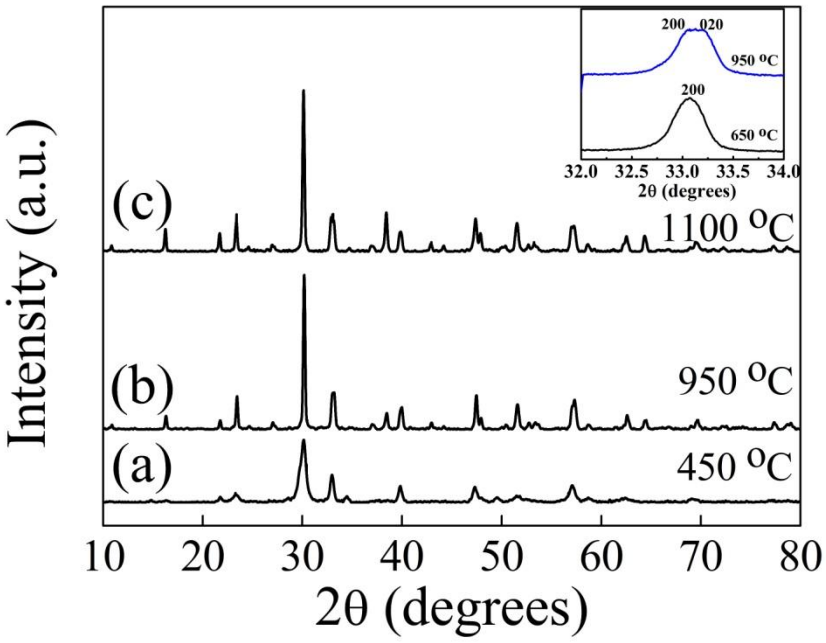

Figure 1 XRD patterns of $Bi_4Ti_3O_{12}$ samples heated at temperature (a) 450 ^oC, (b) 900 ^oC and (c) 1100 ^oC.

Figure 1(b) shows XRD pattern of sample heated at 900 ^oC in air for 20 minutes. Inset shows the splitting of 200 peak into 200 and 020. This indicates that the structure transforms to orthorhombic from a tetragonal structure. It is well known in the case of $Bi_4Ti_3O_{12}$ that as the annealing temperature is increased orthorhombic phase becomes

more stable.[39] Figure 1(c) shows XRD pattern of sample heated at 1100 ^{o}C in air for 24 h. Relative sharper peaks is indicative of large grains size.

Figure 1(a) shows FESEM image of nanoparticles prepared by heating the as prepared sample at 450 ^{o}C for two hours in oxygen atmosphere. It is clear from the image that the particles are well separated with almost uniform size distribution. The average particle size is around 40 nm. FESEM image of sample prepared at 800 ^{o}C for 2 h in

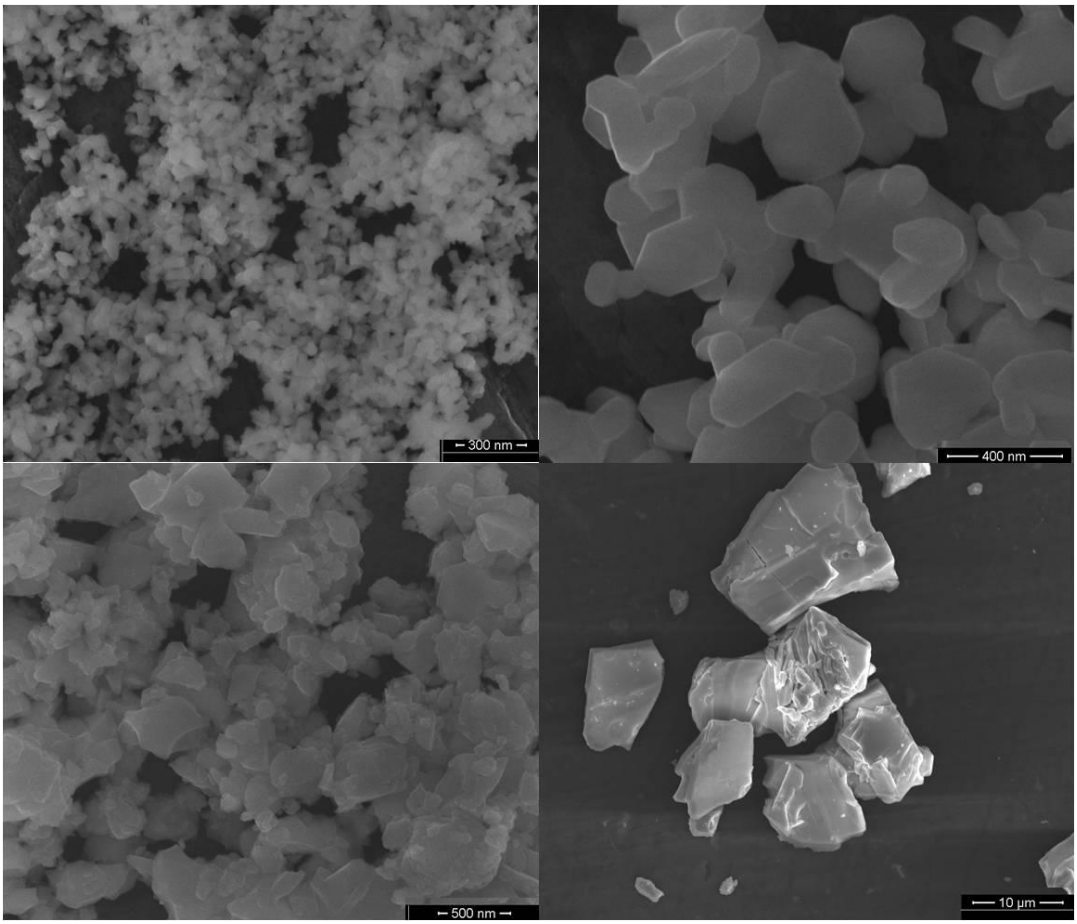

Figure 2 FESEM image of $Bi_4Ti_3O_{12}$ samples heated at temperature (a) 450 ^{o}C, (b) 800 ^{o}C, (c) 900 ^{o}C and (d) 1100 ^{o}C.

oxygen atmosphere is shown in Figure 2(b). The particle size is not uniform and varies from 80 to 350 nm. Figure 2(c) shows FESEM image of pelletized sample heated at 900 ^{o}C for 20 minutes in air. Particles have grown in size compared to the sample heated at 450 ^{o}C but are still of the order 300-400 nm. FESEM image of the bulk sample heated at

1100 ^{o}C in air for 24 h is shown in Figure 2(d). Particles have grown to micron size. Figure 3 shows room temperature magnetization plots for $Bi_4Ti_3O_{12}$ samples prepared at different conditions. Nanoparticle sample prepared at 450 ^{o}C shows highest saturation magnetization value. For samples of bigger sizes the saturation magnetization values are lower in value than that of nanoparticles. The above trend is expected because as the

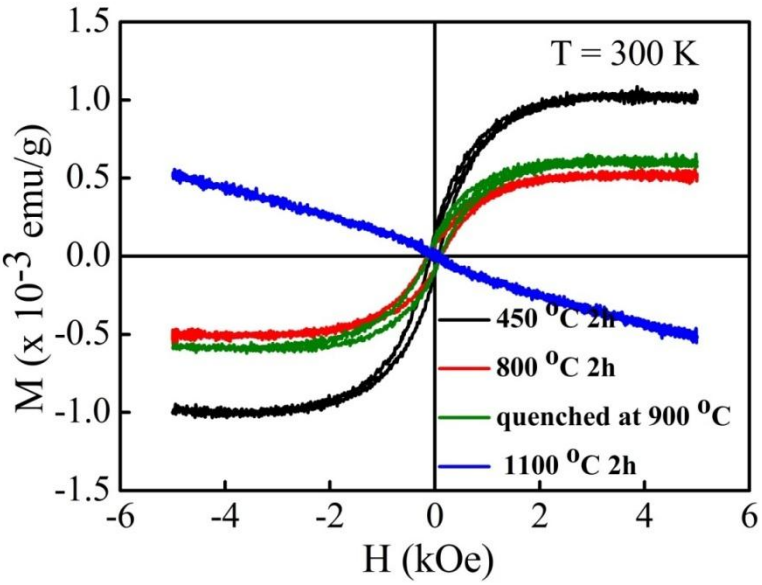

Figure 3 Room temperature magnetization curves for nanoparticles as well as bulk sample

particle size increases the number of defect concentration at the surface of particles decreases. Bulk sample shows perfect diamagnetic behaviour.

Figure 4 shows room temperature polarization versus electric field curve for the sample quenched at 900 ^{o}C for 20 minutes in air measured at a frequency of 10 Hz. A ferroelectric hysteresis loop was observed with remanent polarization (P_r) of 6.3 μC/cm^2, maximum polarization (P_{Max}) of 18 μC/cm^2 and coercive field (E_c) value of 30 kV/cm. Quenching of the sample at high temperature for small time sinters the sample but still retains the size of the grains in nanometer range. This makes possible the observation of ferroelectric loop in nanoparticles which otherwise shows leaky curve in unsintered form.

As the grain size in the nanometer range ferromagnetism due to the surface defects can still be seen in such samples. Magnetoelectric coupling could not be observed because of the high ferroelectric transition temperature of $Bi_4Ti_3O_{12}$.

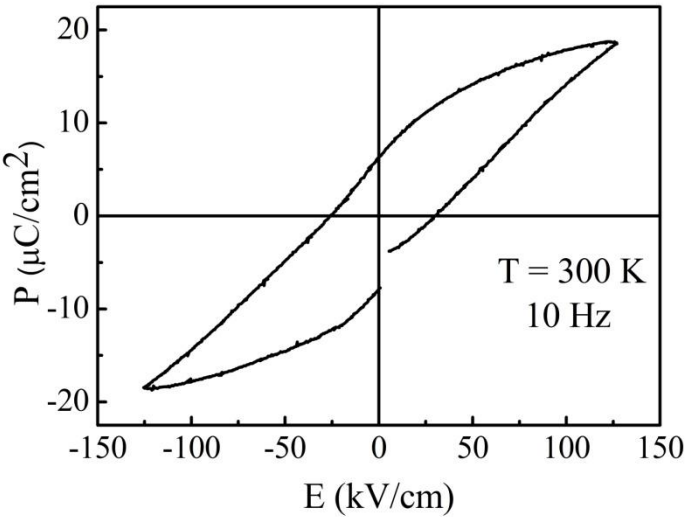

Figure 4 Room temperature polarization against electric field curve for bismuth titanate nanoparticles.

4.6 Conclusion:

$Bi_4Ti_3O_{12}$ nanoparticles show both ferroelectric as well as ferromagnetic hysteresis loops at room temperature. The core of the nanoparticles behaves as ferroelectric material while the surface due to defects gives magnetic ordering. Ferromagnetism has been found to decrease with the increase of particle size, which supports our prediction of defect mediated surface ferromagnetism.

4.7 References:

(1) Dong, S.; Li, J. F.; Viehland, D. *Appl. Phys. Lett.* **2003,** *83*, 2265.

(2) Eerenstein, W.; Mathur, N. D.; Scott, J. F. *Nature* **2006**, *4472*, 759.

(3) Cheong, S.W.; Mostovoy, M. *Nature Mater*. **2006**, *6*, 13.

(4) Ramesh, R.; Spaldin, N. A.; *Nature Mater*. **2007**, *6*, 21 (2007).

(5) Fiebig, M. *J. Phys. D: Appl. Phys.* **2005**, *38*, R123.

(6) Teague, J. R.; Gerson, R.; James, W. *Solid State Commun.* **1970**, *8*, 1073.

(7) Redfern, S. A. T.; Wang, C.; Hong, J. W.; Catalan, G.; Scott, J. F. *arXiv: 0806.3241v2* **2008**.

(8) Zvezdin, A. K.; Pyatakov, A. P. *Phys. Usp.* **2004**, *47*, 416.

(9) Fillippetti, A.; Hill, N. A. *Phys. Rev. B* **2002**, *65*, 195120.

(10) Ravindran, P.; Vidya, R.; Kjekshus, A.; Fjellvag, V.; Eriksson, O. *Phys. Rev. B* **2006**, *74*, 224412.

(11) Kamba, S.; Nuzhnyy, V.; Savinov, M.; Sebek, J.; Petzelt, J.; Prokleska, J.; Haumont, R.; Kreisel, J. *Phys. Rev. B* **2007**, *75*, 024403.

(12) Tutuneu, H. M.; Srivastava, G. P. *Phys. Rev. B* **2008**, *78*, 235709.

(13) Ray, N.; Waghmare, U. *Phys. Rev. B* **2008**, 77, 134112.

(14) Zapata, J. ; Narvdez, J.; Lopera, W.; Gomez, M. E.; Mendoze, G. A.; Prieto, P. V.; *IEEE Trans. Magnetics* **2008**, *44*, 2895.

(15) Ramesh, R. *et al. Nature Mater.* **2008**, *7*, 478.

(16) Su, W. N.; Wang, D. H.; Cao, Q. Q.; Han, C. D.; Yin, J.; Zhang, J. R.; Da, Y. W. *Appl. Phys. Lett.* **2007**, *91*, 092905.

(17) Ederer, C.; Spaldin, N. A. *Phys. Rev. B* **2005**, *71*, 224103.

(18) Wang, N.; Chang, J.; Pyatakov, A.; Zvezdin, A. K.; Li, J. F.; Cross, L. E.; Viehland, D. *Phys. Rev. B* **2005**, *72*, 104434.

(19) Kubel, F.; Schmid, H. *Acta Cryst.* **1990**, *B46*, 698.

(20) Moreau, J. M.; Michel, C.; Gerson, R.; James, W. J.; *J. Phys. Chem. Solids* **1971**, *32*, 1315.

(21) Teague, J. R.; Gerson, R.; James, W. J. *Solid State Commun.* **1970**, *8*, 1073.

(22) Ramesh, R. *Science* **2003**, *299*, 1719.

(23) Katsura, H.; Nagaosa, N.; Balatsky, A. V.; *Phys. Rev. Lett.* **2005**, *95*, 057205.

(24) Sergienko, I. A.; Dagotto, E. *Phys. Rev. B* **2006**, *73*, 094434.

(25) Mostovoy, M. *Phys. Rev. Lett.* **2006**, *96*, 067601.

(26) Harris, A. B. *Phys. Rev. B* **2007**, *76*, 054447.

(27) Newnham, R. E.; Kramer, J. J.; Schulze, W. A.; Cross, L. E. *J. Appl. Phys.* **1978**, *49*, 6088.

(28) Kenzelmann, M.; Harris, A. B.; Jonas, S.; Broholm, C.; Schefer, J. et al. *Phys. Rev. Lett.* **2005**, *95*, 087206.

(29) Lawes, G.; Harris, A. B.; Kimura, T.; Rogado, N.; Cava, R. J.; *et al. Phys. Rev. Lett.* **2005**, *95*, 087205.

(30) Kimura, T.; Lawes, G.; Ramirez, A. P. *Phys. Rev. Lett.* **2005**, *94*, 137201.

(31) Kimura, T.; Lashley, J. C.; Ramirez, A. P. *Phys. Rev. B* **2006,** *73*, 220401.

(32) Yamasaki, Y.; Miyasaka, S.; Kaneko, Y.; He, J. P.; Arima, T.; Tokura, Y. *Phys. Rev. Lett.* **2006**, *96*, 207204.

(33) Taniguchi, K.; Abe, N.; Takenobu, T.; Iwasa, Y.; Arima T. *Phys. Rev. Lett.* **2006**, *97*, 97203.

(34) Heyer, O.; Hollmann, N.; Klassen, I.; Jodlauk, S.; Bohat´y, L.; *et al.* 2006. *J. Phys. Condens. Matter* **2006**, *18*, L471.

(35) Arkenbout, A. H.; Palstra, T. T. M.; Siegrist, T.; Kimura, T. *Phys. Rev. B* **2006**, *74*, 184431.

(36) Mangalam, R. V .K.; Ray, N.; Waghmare, U.; Sundaresan, A.; Rao, C. N. R. *Solid State Commun.* **2009,** *149*, 1.

(37) Bhattacharya, S.; Datta, A.; Chakravorty, D. *Appl. Phys. Lett.* **2010**, *96*, 09310

(38) Aurivillius, B. *Ark. Kemi*. **1950**, *1*, 499.

(39) Du, Y,; Fang, J.; Zhang, M.; Hong, J.; Yin, Z.; Zhang, Q. *Mater. Lett.* **2002**, *57*, 802.

Chapter 5

Ferromagnetism in CaF_2 Nanoparticles

Summary

In this chapter magnetic properties of CaF_2 nanoparticles have been reported which is the first such study in any halide system. Nanoparticles prepared by two different methods show ferromagnetic hysteresis loop at room temperature. The values of saturation magnetization suggest that it is dependent on the method of preparation. Photoluminescence spectrum gives a broad defect band in the blue region.

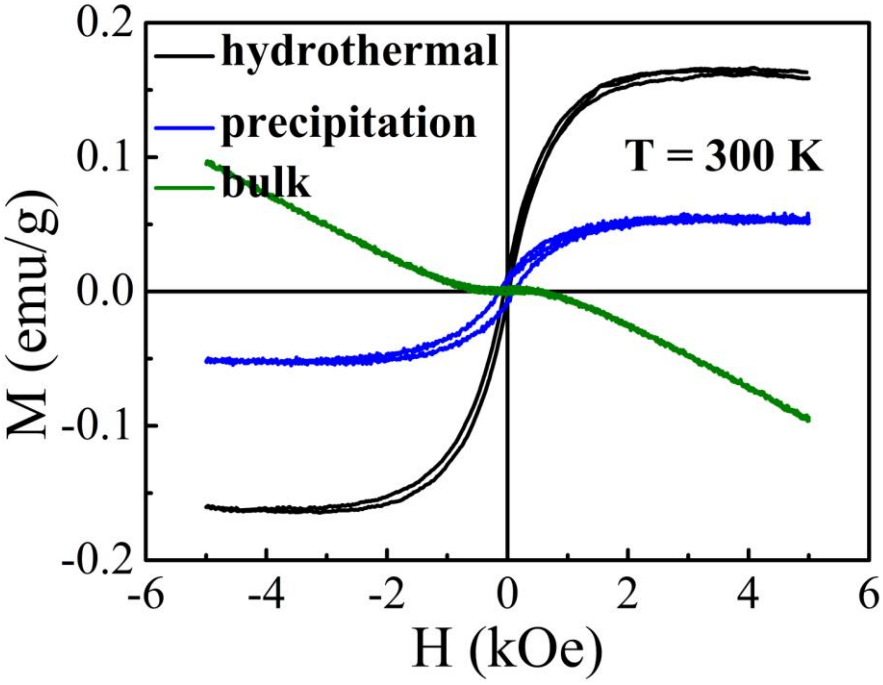

5.1 Introduction:

Alkaline earth metal fluorides are mainly known for their high optical transparency due to low energy phonons and high iconicity.[1] Surface ferromagnetism in nanoparticles of oxides, sulphides and nitrides of otherwise nonmagnetic materials has been studied in the recent past but there is no report of such magnetism in halide systems. We have studied magnetic properties of calcium fluoride prepared by direct precipitation methods (CF1) as well as by hydrothermal method (CF2).

5.2 Experimental Procedure:

In direct precipitation method[2], 2 g of $CaCl_2.2H_2O$ was dissolved in 180 ml of ethanol to get a colourless transparent solution. A slight excess of NH_4F was added to this solution and a white suspension formed upon stirring. After the mixture was stirred for 12 h, a white suspension was obtained which was centrifugation and washed first with distilled water and then by ethanol. The product obtained was dried at 80 ^oC for 4 h. The as prepared powder was heated at 400 ^oC in argon atmosphere.

Both $CaCl_2$ and NH_4F can dissolve significantly in water. But the CaF_2 is insoluble water, which will precipitate from an aqueous solution. Thus, the solid CaF_2 precipitation can be obtained easily by the reaction of the Ca^{2+} and F^- ions that formed by the dissociation of $CaCl_2$ and NH_4F in an aqueous solution. However, it is difficult to control particle growth of CaF_2 crystals because high Ca^{2+} and F^- ion concentration in an aqueous solution results in significant reaction rates. Therefore, the reactions to synthesize CaF_2 nanoparticles were carried out in an ethanol solution under ambient pressure. When mixture of $CaCl_2$ and NH_4F powders was stirred in an ethanol solution, only very low F^- ion concentration can be formed because the solubility of NH_4F in

ethanol solution is much smaller than that in an aqueous solution. Thus, the particle growth of the precipitated CaF_2 solid is very limited due to very small F^- ion concentrations in ethanol solution. The CaF_2 nanoparticles could be obtained by the combination of the Ca^{2+} and F^- ions in ethanol solution. With the proceeding of precipitation to form CaF_2 nanoparticles, the F^- ion concentrations in the ethanol solution will decrease gradually. Thus, more F^- ions will be released stepwise by the dissociation of the NH_4F in order to maintain the equilibrium concentrations of the F^- ion in the ethanol solution. The released F^- ions will continue to combine with the Ca^{2+} ions to form more CaF_2 nanoparticles.

In hydrothermal method, 0.25 g of of $CaCl_2.2H_2O$ was taken in 50 ml of distilled water. A slight excess of NH_4F was added to this solution to get a white precipitate. The mixture was stirred for 10 minutes and then transferred to a teflon lined hydrothermal bomb. The bomb was kept at 120 ^oC for 10 hours. After that it was allowed to cool to down to room temperature. The product was centrifuged and washed first with distilled water and then with ethanol.

5.3 Results and Discussion:

Figure 1 shows XRD pattern of CaF1 and CF2 sample. For CF2 sample, prepared by hydrothermal method, XRD peaks are very sharp indicating the high crystallinity of the sample. On the other hand, relatively broader peaks were obtained for CF2 sample.

Figure 2(a) shows FESEM image of CF1 sample. A TEM image of sample CF2 is shown in Figure 2(b).

.

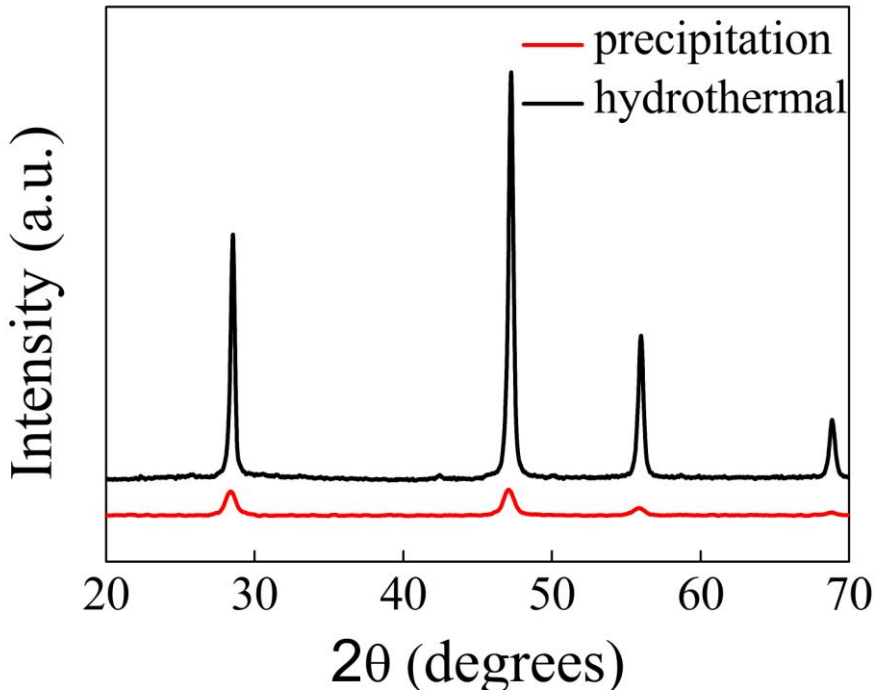

Figure 1 XRD patterns of the samples prepared by direct precipitation and hydrothermal method.

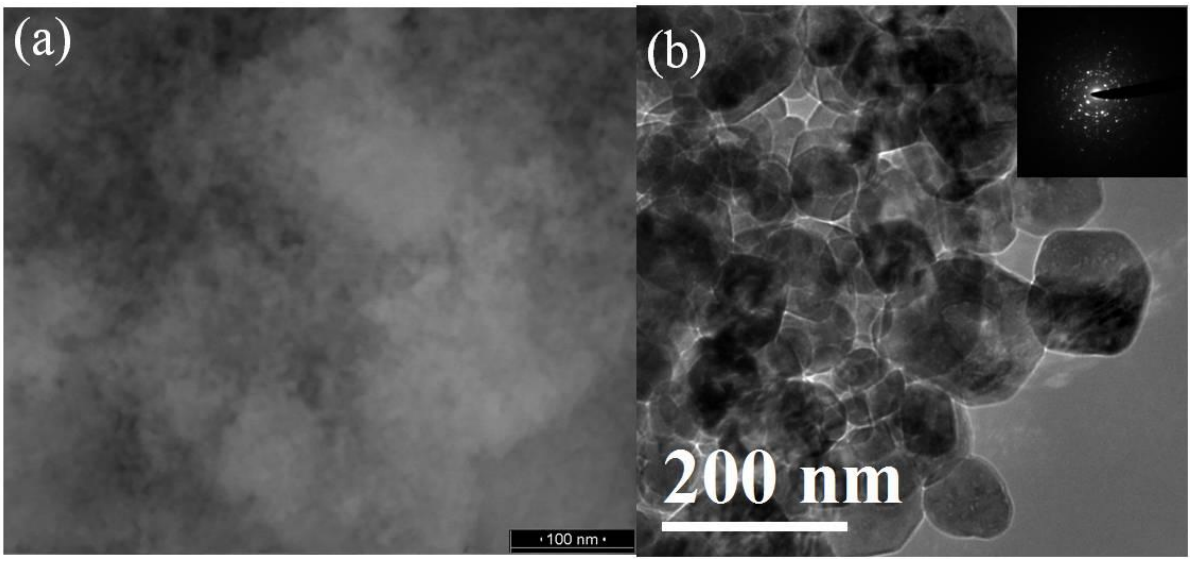

Figure 2(a) FESEM image of nanoparticles prepared by direct precipitation method, (b) by hydrothermal method.

The average particle size of CF1 sample is around 15 nm. CF2 sample which was prepared by hydrothermal method contains single crystalline particles which is clear from the ED pattern shown in the inset of Figure 2.

Magnetic properties of samples are shown in Figure 3.

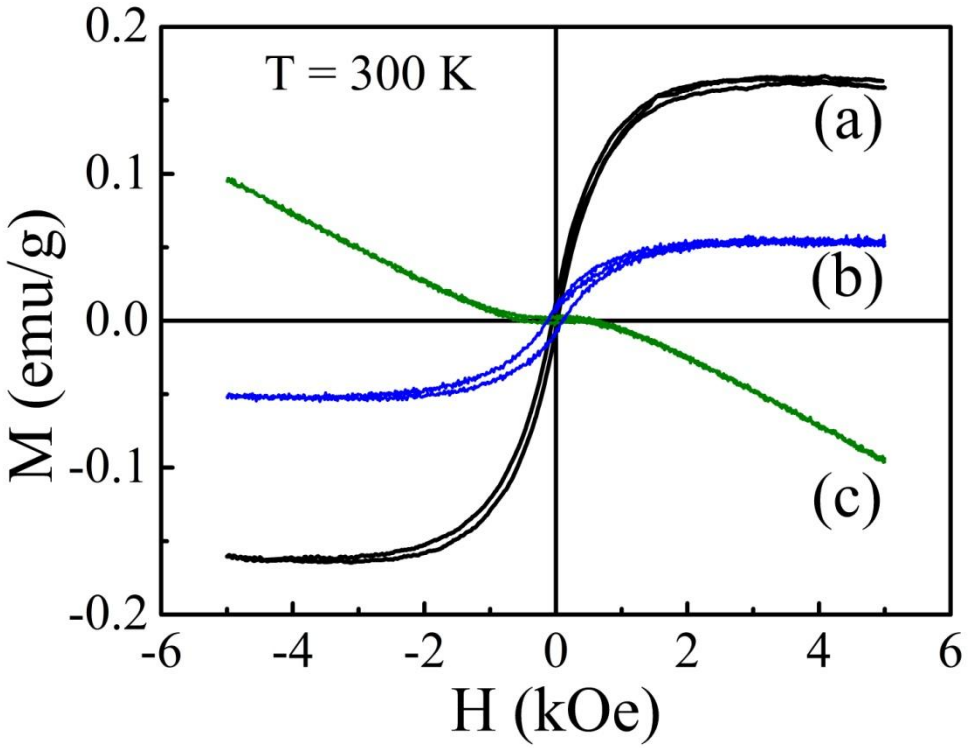

Figure 3 Room temperature magnetization curves for (a) CF2, (b) CF1 and (c) bulk samples.

CF1 and CF2 samples show ferromagnetic hysteresis loop at room temperature. Saturation magnetization of sample CF2, which was prepared by hydrothermal method, was relatively higher than sample CF1. This indicates the fact fact that magnetization value depends on the meyhod of synthesis which governs the defect concentration at the surface of the nanoparticles. Bulk CaF_2 shows diamagnetic behaviour.

Figure 3 shows the PL spectra of sample CF2 at room temperature. The spectra shows a broad beak in the blue region when excited by a light of wavelength 370 nm.

This broad emission band may be attributed to the defects present mainly on the surface of the nanoparticles because bulk CaF_2 is known to be optically transparent in this region.

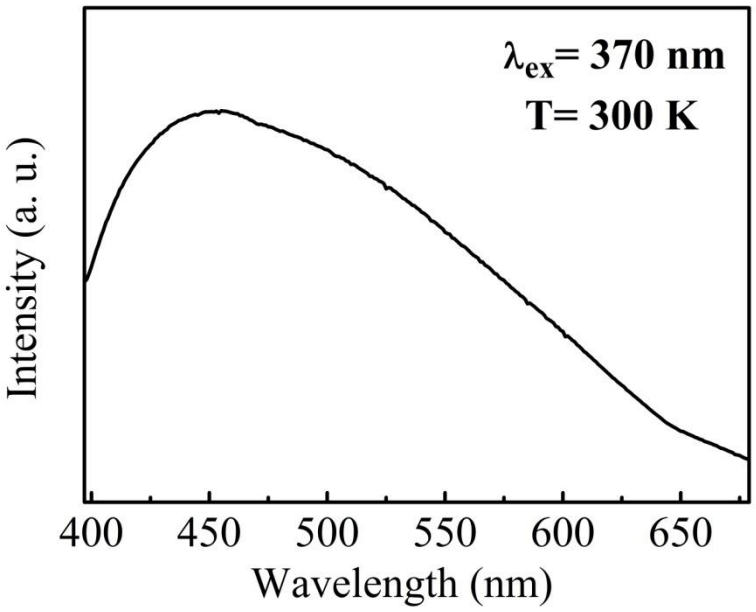

Figure 4 PL spectrum of CF2 sample.

5.4 Conclusion:

CaF_2 were prepared by direct precipitation and hydrothermal method. The more crystalline particles in the case of sample prepared by hydrothermal method show a larger value of saturation magnetization This indicates that magnetization values depend on the method of synthesis. PL spectrum shows a broad emission band in blue region and has been attributed to defects on the surface of the nanoparticles.

5.5 References:

(1) Joubert, M. F.; Guyot, Y.; Jacquier, B.; Chaminade, J.P.; Garcia, A. *J. Fluorine Chem.* **2001**, *107*, 235.

(2) Wang, F.; Fan, X.; Pi, D.; Wan, M. *Solid State Commun.* **2005**, *133*, 775.

MISCELLANEOUS

Negative magnetization in Zero Field Cooled (ZFC) Conditions: Is it Intrinsic?

Summary*

In this chapter problems associated with the measurement of zero-field-cooled (ZFC) magnetization and its interpretation in the light of negative magnetization reported in materials such as $CoCr_2O_4$ have been addressed. The negative magnetization is also seen in other spinel systems like $CoFe_2O_4$ and CoCr2-xFexO4 (0 < x >1). We demonstrate that the negative magnetization in ZFC conditions is an artefact arising from a small negative trapped field in the sample space as well as large coercive fields. The problem is commonly encountered while working with magnetometers and a superconducting magnet where the sign of the trapped field can be positive or negative depending on the way the field is reduced to zero.

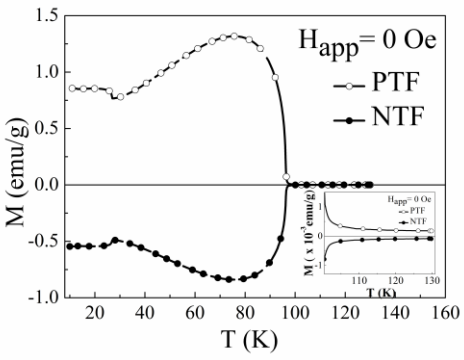

* The paper based on this work has been published in *Solid State Commun.* ***2010***, *doi:10.1016/j.ssc.2010.03.016*

M.1 Introduction:

Magnetism is fascinating because of various magnetic phenomena and understanding of their physical principles involved often leads to applications in real world. Negative magnetization, which may find its application in data storage, but its origin is not yet fully understood even after its early prediction by Néel in 1948.[1] According to him, certain ferrimagnetic materials will exhibit spontaneous magnetization that changes sign with temperature or magnetic field due to different temperature dependence of sublattice magnetization associated with two different crystallographic sites. This phenomenon was indeed experimentally observed in mixed spinels, for example, in $Li_{0.5}Fe_{2.5-x}Cr_xO_4$ and Co_2VO_4[2, 3] Later, many other ferrimagnetic systems such as garnets, molecular magnets and even antiferromagnetic materials were shown to exhibit negative magnetization below a compensation temperature (temperature at which the magnetization changes sign).[4, 7] In the case of orthovanadates RVO_3 (R=La, Nd, Sm, Gd, Er and Y), various models including antisymmetric Dzyaloshinsky-Moriya interactions have been proposed to account for the negative magnetization[8]. The term 'negative magnetization' here should not be confused with diamagnetism. Unlike diamagnetic materials, they are still in the magnetically ordered state in the temperature range where they show negative magnetization even after applying positive magnetic field.

M.1.1 Ferrimagnetism:

The word ferrimagnetism was first introduced by Néel[1] in order to describe the properties of those substances which below a certain temperature exhibit spontaneous

magnetization arising from a non-parallel alignment of atomic magnetic moments. In his original paper Néel envisaged a partitioning of the moments into two sub-lattices, which because of their mutual interaction are aligned antiparallel to each other, thus producing a total magnetic moment equal to the difference between their individual magnitudes. This difference can arise in several ways, and some of these are shown diagrammatically in Figure 1.

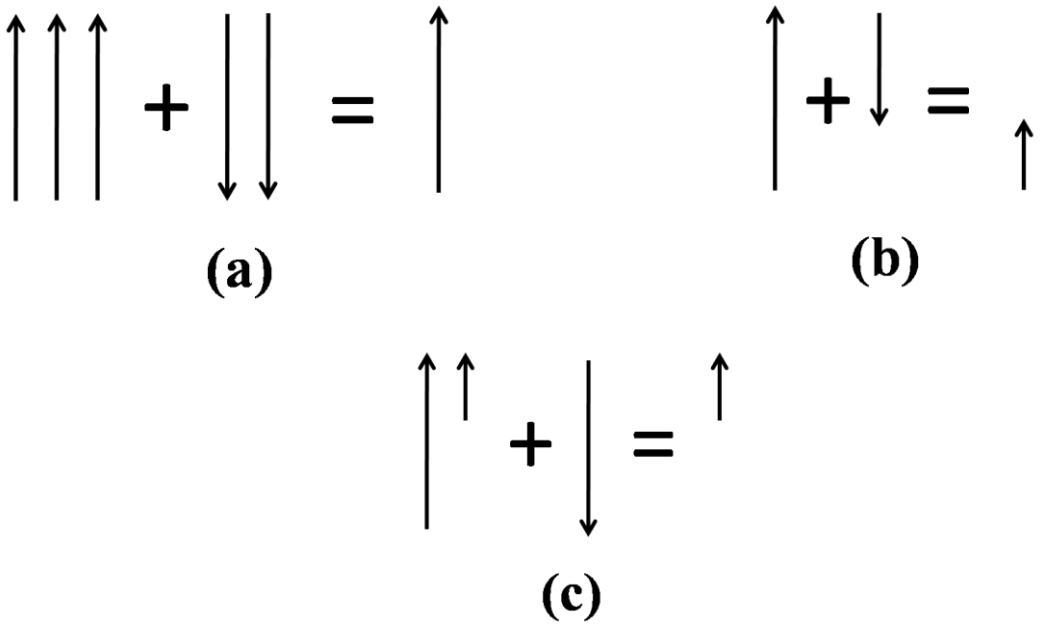

Figure 1 Arrangement of spins in two sublattices in ferrimagnetic materials.

Figure 1(a) shows the case in which there are different numbers of similar magnetic moments in the sub-lattices. In some respects this arrangement resembles that of a normal antiferromagnetic substance with unequal partitioning of the sublattices, but many of the properties of such a substance are similar to those of a ferromagnet with a reduced number of magnetic moments. Figure l(b) shows the case of equal numbers of dissimilar moments. The dissimilarity can arise either because the magnetic ions are chemically different, or because a different local environment leads to different effective magnetic moments in ions having the same spin. A third type of arrangement is shown in

Figure l(c). This is the case originally considered by Néel and it represents a very large number of substances, including most of the ferrites. In this arrangement one sub-lattice contains two different types of magnetic moment, one of which also occurs in equal numbers on the second sub-lattice, so that the net effect is that of just the one type of moment.

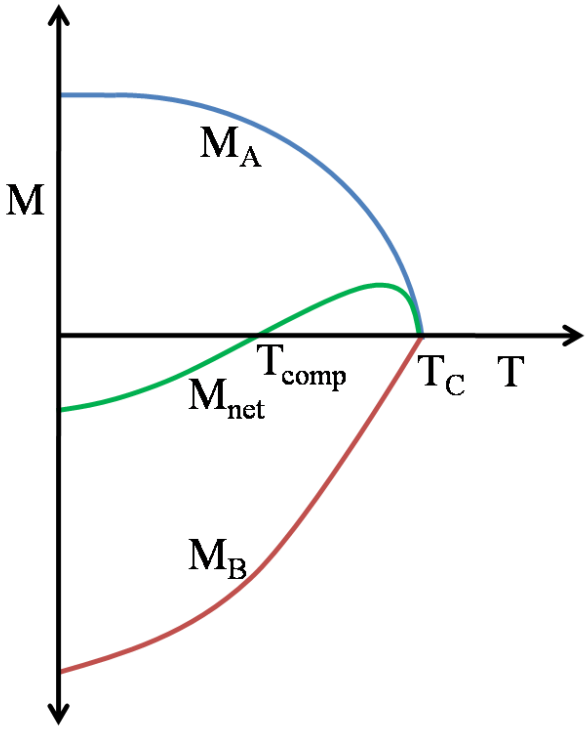

Figure 2 A ferrimagnetic with two sulattices showing compensation temperature.

M_A = Magnetization of sublattice A

M_B = Magnetization of sublattice B

M_{net} = Net magnetization

T_{comp} = Compensation temperature

Figure 2 shows a schematic of a ferromagnetic material with one compensation temperature (T_{comp}). The net magnetization (M_{net}), which is the difference of magnetization of sublattice A (M_A) and B (M_B), is negative below the compensation temperature. It is important to note that a material can have one or more than one compensation temperatures below its transition temperature (T_C) depending on how the magnetizations of individual sublattices vary with temperature.

M.1.2 Spinels:

The spinel structure is based on a cubic close packed array of anions, especially oxides. Such a close-packed array has both octahedral and tetrahedral interstices. In spinels, one half of the octahedral sites, and one eighth of the tetrahedral sites, are usually occupied, giving a stoichiometry AB_2O_4, where A and B are generally either divalent and trivalent, respectively (the so-called 2,3 spinels) or tetravalent and divalent (the 4, 2 spinels).

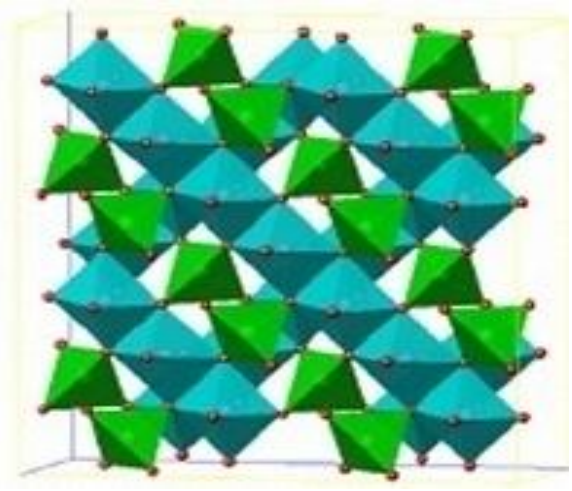

Figure 3 A model showing tetrahedral and octahedral sites in spinel structure.

The cation distribution is said to be a ***normal*** if all the A cations are on tetrahedral sites with all the B on octrahedral sites, or ***inverse*** if all the sites are occupied by B cations with the sites occupied by the A and the rest of the B cations.[9, 10] If we define an inversion parameter, λ, to be the fraction of the B cations occupying tetrahedral sites, then for a normal distribution, λ = 0; for an inverse distribution, λ = 0.5. $MgAl_2O_4$ and $CoFe_2O_4$ are examples of normal and inverse spinel respectively. The distribution is called ***mixed*** when λ takes value other than 1 or 0.5.

M.2 Scope of the Present Work:

Recently, there has been a lot of interest in the ferrimagnetic (T_C ~ 93 K) spinel $CoCr_2O_4$ because of its multiferroic properties with a magnetoelectric coupling below the spiral magnetic ordering at ~ 26 K.[11, 12] A few reports of magnetization studies on bulk and nanoparticles of $CoCr_2O_4$ have shown that these samples exhibit negative magnetization just below T_C under ZFC measurement condition with low applied field (~ 100 Oe), while the magnetization remains positive in the case of FC measurement condition for the same applied field.[13, 14] This behaviour is remarkably different from what is seen in the above mentioned materials that change sign at the compensation temperature which lies well below the magnetic ordering temperature. The observed negative magnetization in $CoCr_2O_4$ has been attributed to uncompensated spins at the grain boundaries.[13] But, it is difficult to conceive the negative magnetization based on the uncompensated spins. It is most likely that there could be a small trapped field in the superconducting magnet during cooling that can affect the magnetization drastically under ZFC condition as observed in RVO_3 system.[15, 16] However, if the origin of negative magnetization is intrinsic, such studies would be interesting from physics point of view as well as possibility of exploiting the phenomenon for device applications such as magnetic memory and switching. It is for these reasons, we have reinvestigated the magnetic properties of $CoCr_2O_4$ and demonstrate that the observed negative magnetization under ZFC condition is an artefact due to trapped field in the superconducting magnet. Although we have shown that the trapped fields can influence the magnetization behaviour of $CoCr_2O_4$, it is common to ferro- and ferrimagnetic materials, particularly with significant magnetic anisotropy and coercive field.

M.3 Zero Field Cooled (ZFC) and Field Cooled (FC) Magnetization:

Conventionally there are two ways of doing magnetization measurements with respect to temperature. In the first magnetization process the sample is cooled in the absence of field to the lowest temperature followed by applying magnetic field and measuring the magnetization while warming up the sample. This process is called ZFC.In the second process the sample is cooled in the presence of applied magnetic field and the magnetization is measured while cooling or warming. This process is called FC

M.4 Experimental Procedure:

$CoCr_2O_4$, $CoFe_2O_4$ and solid solutions of intermediate compositions were prepared by solid state reaction of thoroughly mixed powders of stoichiometric amount of Co_3O_4 (Aldrich), Fe_2O_3 (Alfa-Aesar, 99.5 %) and Cr_2O_3 (Sigma-Aldrich, 99.9 %) at 1350^oC in air for several hours with intermittent grindings. Co_3O_4 powder was preheated at 900 ^oC for 12 h in air before use.

M.5 Characterization:

Phase purity of the samples were checked by the analysis of powder X-ray diffraction (XRD) pattern recorded with a Bruker D8 Discover diffractometer. Profile matching of XRD patterns wes done using the program *Fullprof.*[17] Magnetic measurements were carried out with Vibrating Sample Magnetometer (VSM) option in Physical Properties Measurement System (PPMS), Quantum Design, USA.

M.6 Results and Discussion:

Analysis of XRD pattern of $CoCr_2O_4$ by pattern matching confirmed that the sample was single phase having the normal spinel structure (space group Fd3m) with lattice parameter, a = 8.3343(1) Å. $CoFe_2O_4$ also has the same space group with inverse spinel structure. XRD patterns of $CoCr_2O_4$ and $CoFe_2O_4$ are shown in Figure 4(a) and (b) respectively with pattern matching. Observed intensity (I_{obs}) and calculated intensity (I_{cal}) match with each other very nicely.

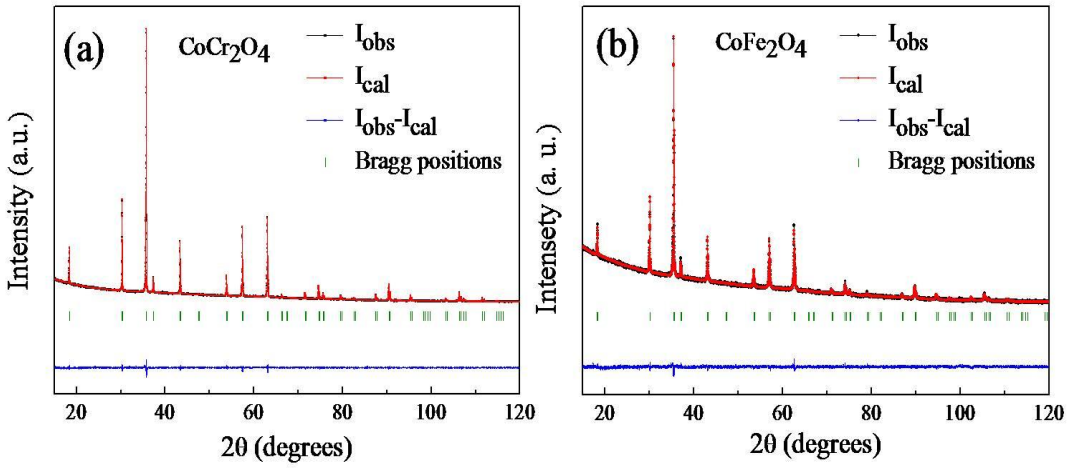

Figure 4(a) and (b) are XRD patterns of $CoCr_2O_4$ and $CoFe_2O_4$ respectively with pattern matching.

Figure 5 shows the magnetization as a function of temperature measured under ZFC and FC conditions with an applied field of 100 Oe. The observed magnetization behaviour is very similar to what is reported earlier.[12, 13]There are two magnetic anomalies, one at 97 K which corresponds to ferrimagnetic ordering and the other at 27 K is due to noncollinear conical spiral ordering. More importantly, just below T_C, the ZFC curve shows a peak in magnetization below which it crosses zero magnetization and becomes negative at low temperatures. With increasing applied magnetic field, the peak in magnetization moves to low temperature and becomes broad. Further, the negative magnetization observed at lower fields become positive at large enough fields as shown

in the inset of Figure 5. It is evident from the inset that even an applied field of 100 Oe also is not sufficient enough to make the magnetization positive at 5 K.

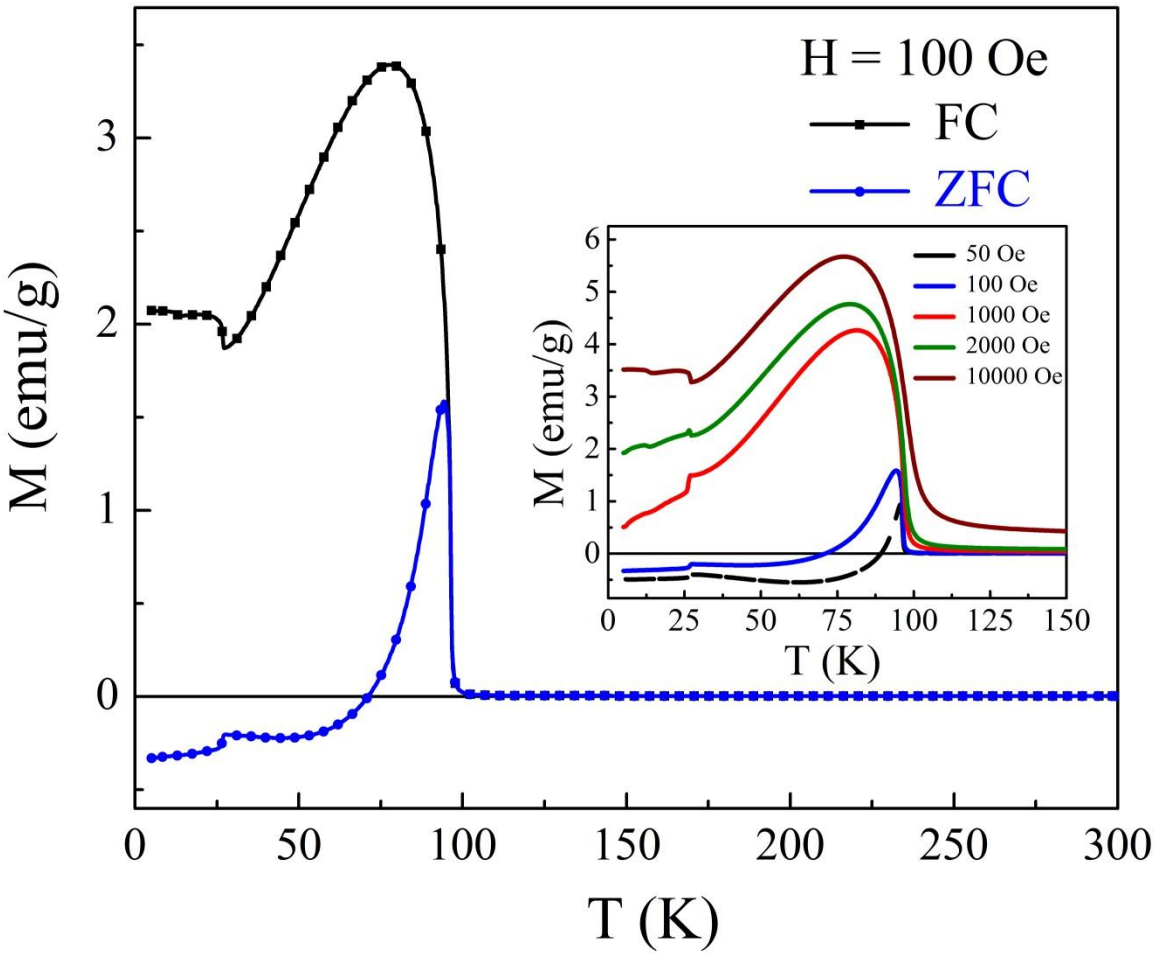

Figure 5 ZFC and FC magnetization versus temperature curves of $CoCr_2O_4$ measured with an applied field of 100 Oe. Inset shows ZFC curves at different applied fields.

To know the exact value of applied field, at which the magnetization changes sign from negative to positive, magnetization versus applied magnetic field was recorded at 5 K which is shown in Figure 6. The plot shows a hysteresis loop typical for a ferrimagnetic material below its Curie temperature. Inset of Figure 6 shows a magnified view near origin in order to see the behaviour at small values of applied field. The hysteresis loop starts from a negative value of magnetization and remains negative till ~ 550 Oe.

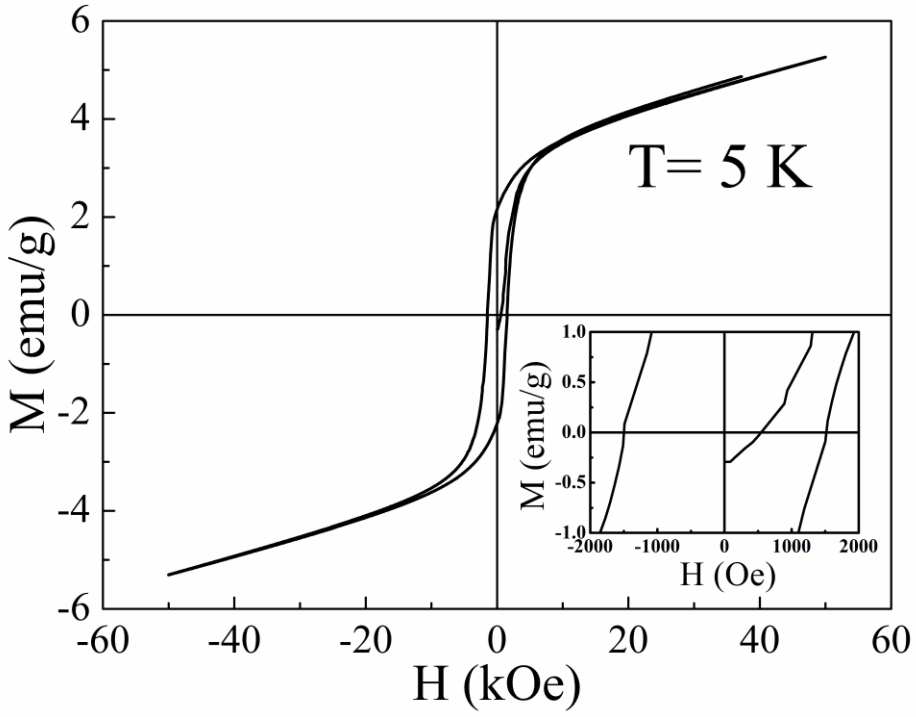

Figure 6 Magnetization vs. applied magnetic field plot for CoCr2O4 at 5 K. Inset shows magnified view near origin.

In order to understand this magnetization behaviour, it is important to rule out extrinsic origin of such unusual magnetism. In this respect, it is essential to look at the history of the superconducting magnet just before doing the magnetization measurement because the ZFC measurements are very sensitive to the remanent field present in most of the magnetometers.

Shown in Figure 7 is a schematic which shows how a small remanent field remains trapped when the applied field is set to zero from a large value, in linear mode.[18] As illustrated in the table and the accompanying figure, a magnet is originally in its virgin state (1) in which no flux is pinned inside it. Upon connecting the magnet to the power supply and passing current in the windings (2), a positive field is generated in the sample

space at the center. After removing the current in the magnet and setting the magnet persistent (3), some flux remains pinned in magnet and has the same sign as the original field because it resulted

Step	magnet state	magnet mode	I_{magnet}	B_{sample}
1	virgin	persistent	0	0
2	charged	driven	$I_2 > 0$	$B_2 > 0$
3	remanent	persistent	$I_3 = 0$	$B_3 < 0$

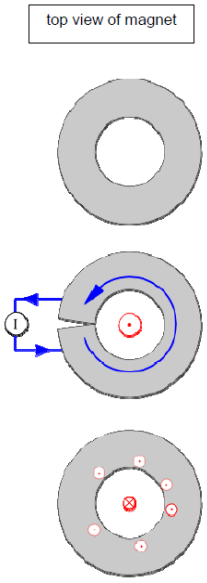

Figure 7 Schematic to show remanent field in the sample space after setting the field zero.*(ref 18)*

from field lines penetrating the magnet at positive fields. However, the stray fields from these “dipoles” are of course of the opposite sign, hence the negative initial remanent field stays at the sample space after discharging from positive fields.

As our PPMS is not equipped with low-field option to reduce the magnitude of the remanent field below 0.1 Oe, we normally minimize the remanence down to a few Oersteds by setting the field to zero (from an initial field > 1 T) in oscillation mode. This small field is the result of trapped magnetic flux inside the superconducting material. Consequently, in the ZFC measurement, the sample was cooled under the trapped field.

The other important parameter is the sign of the trapped field that is opposite in sign when reducing the field to zero from a positive or negative field. In the present case, the field was reduced from a positive value and therefore the trapped field is negative. Thus, the sample was field cooled (FC) under negative trapped field (NTF) to the lowest temperature and then a positive field of 100 Oe was applied and the magnetization was measured while warming. During cooling, the NTF forces the moments to align in the negative direction and the applied positive field (100 Oe) could not change the magnetization direction to positive presumably because of magnetic anisotropy and large coercive field. With increase of temperature, the magnetization changes its sign from negative to positive because of decrease in magnetic anisotropic constant and coercive field which results in rotation of spins towards applied field direction. This explains the observed negative magnetization in ZFC measurement. In order to confirm this, we measured magnetization under NTF *without applying* any external magnetic field and the results are shown in Figure 8. It is seen that the magnetization in the entire temperature range including the paramagnetic state is negative. Similarly, we measured the magnetization under positive trapped field (PTF) after reducing the field to zero from a large negative field in oscillation mode. As expected, the magnetization in the entire temperature range is positive and mirror image of that measured under NTF. The positive and negative values of magnetization in the paramagnetic state are clearly seen in the inset of Figure 8. The values of NTF and PTF obtained by equating the susceptibility values in the paramagnetic state are -2.1 Oe and 3.6 Oe, respectively. These results further confirm that the negative magnetization observed in $CoCr_2O_4$ under ZFC condition is an artefact arising from the trapped magnetic field in the superconducting magnet.

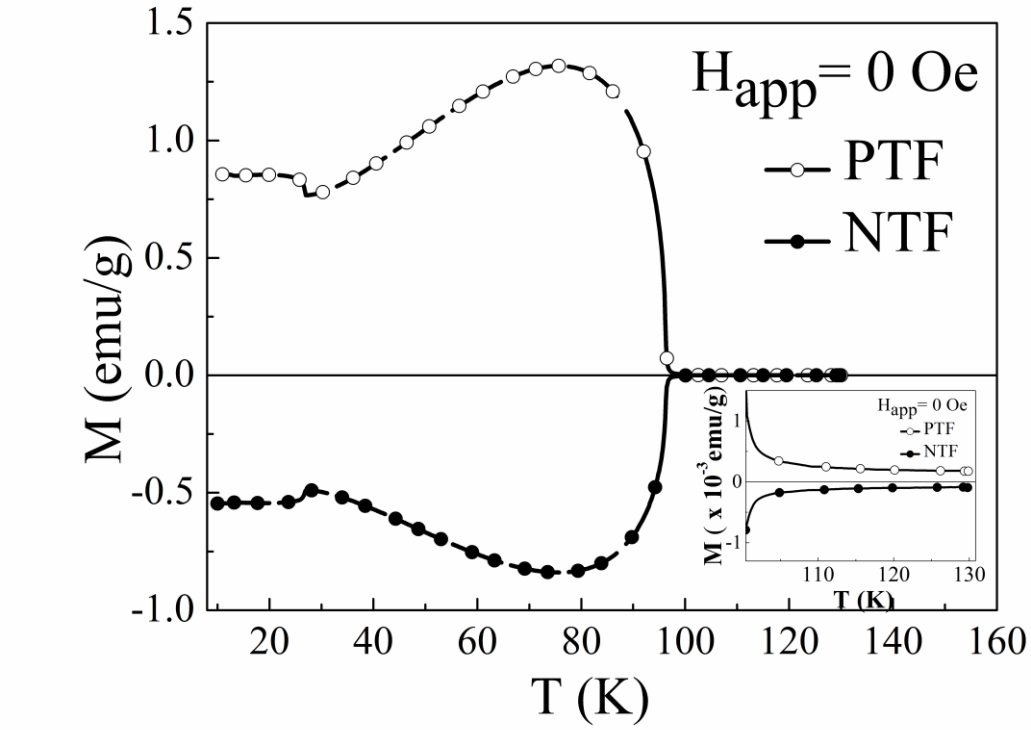

Figure 8 Magnetization as a function of temperature measured under positive trapped field and negative trapped field. Inset shows positive and negative magnetization in the paramagnetic region.

Similar behaviour has been observed in $CoFe_2O_4$, $CoFeCrO_4$ and other intermediate compositions under ZFC condition with NTF, which supports the non intrinsic characteristic of negative magnetization in some spinel systems. Figure 9 shows ZFC plots of $CoCr_2O_4$, $CoFe_2O_4$ and other intermediate compositions at an applied magnetic field of 50 Oe under NTF condition. All compositions show negative magnetization under NTC condition. The compensation temperature and magnetization value at the lowest measured temperature do not follow any pattern. This can be attributed to the fact that the value of negative stray field is different every time the

applied magnetic field is reduced to zero from a large positive value even in the oscillation mode.

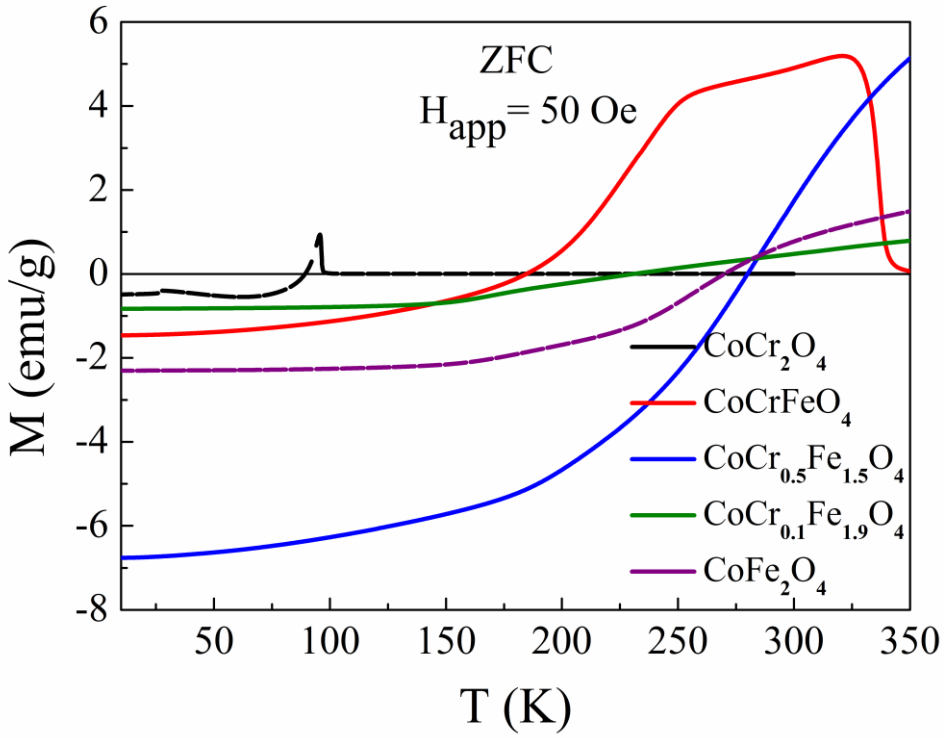

Figure 9 ZFC magnetization of $CoCr_2O_4$, $CoFe_2O_4$ and intermediate compositions at an applied magnetic field of 50 Oe under NTF condition.

In fact, it was shown earlier that even earth's magnetic field can influence the magnetization behaviour of certain magnetic materials.[19] It is noteworthy that even in the case of materials which exhibit intrinsic negative magnetization, the ZFC magnetization measured under negative trapped field does not represent the intrinsic magnetic property of the material.[9, 20] Therefore, we suggest that one has to be cautious while measuring and interpreting magnetization under ZFC condition. Unless the trapped field is removed completely by some means, the magnetization behaviour will be dominated by the trapped fields depending on the intrinsic magnetic properties of the material. In order to observe intrinsic negative magnetization under ZFC condition, the field should be

reduced to zero from a negative field in oscillation mode so that the trapped field is positive.[16] Since this measurement condition is nothing but field cooling under small positive trapped field, the ZFC magnetization will resemble the behaviour of FC magnetization.[16] We also suggest that the negative trapped field should be avoided for all magnetic measurements.

M.7 Conclusion:

Magnetic measurements on $CoCr_2O_4$, $CoFe_2O_4$ and other intermediate compositions suggest the fact that negative magnetization in such systems in ZFC conditions is not intrinsic and can be attributed to negative remanent field in the sample space. We confirmed this observation for $CoCr_2O_4$ by measuring magnetization against temperature in the presence of trapped fields (NTF and PTF), without applying any external field. In NTF condition, magnetization in the whole range remained negative. To avoid getting negative magnetization which is not intrinsic property of the sample we further suggest that ZFC magnetization should be carried out in PTF conditions if absolute zero field at the sample space cannot be ensured.

M.8 References:

(1) Néel, L.**;** *Ann. phys.* **1948**, *3*, 137.

(2) Gorter, E. W.; Schulkes, J. A.; van Wieringen, J. S. *Phys. Rev.* **1953**, *89*, 487.

(3) Menyuk, N.; Dwight, K.; Wickham, D. G. *Phys. Rev. Lett.* **1960**, *4*, 119.

(4) Néel, L.; Pauthenet, R.; Dreyfus, B. *Prog. Low temp. Phys.* **1965**, *4*, North Holland Publishing Company, Amsterdam, 344.

(5) Ohkoshi, S.; Abe, Y.; Fujishima, A.; Hashimoto, K. *Phys. Rev. Lett.* **1999**, *82*, 1285.

(6) Kumar, A.; Yusuf, S. M.; Keller, L.; Yakhmi, J. V. *Phys. Rev. Lett.* **2008**, *101*, 207206.

(7) Kageyama, H.; Khomskii, D. I.; Levitin, R. Z.; Vasil'ev, A. N. *Phys. Rev. B* **2003**, *67*, 224422.

(8) Ren, Y.; Palstra, T. T. M.; Khomskii, D. I.; Nugroho, A. A.; Menovsky, A. A.; Sawatzky, G. A. *Phys. Rev. B* **2000**, *62*, 6577.

(9) Dunitz, J. D.; Orgel, L. E. *J. Phys. Chem. Solids* **1957**, *3*, 318.

(10) Burdett, J. K.; Price, G. D.; Price, S. L. *J. Am. Them. Sot.* **1982**, *104*, 92.

(11) Yamasaki, Y.; Miyasaka, S.; Kaneko, Y.; He, J. P.; Arima, T.; Tokura, Y. *Phys. Rev. Lett.* **2006**, *96*, 207204.

(12) Choi, Y. J.; Okamoto, J.; Huang, D. J.; Chao, K. S.; Lin, H. J.; Chen, C. T.; Veenendaal, M. V.; Kaplan, T. A.; Cheong, S. W. *Phys. Rev. Lett.* **2009**, *102*, 067601.

(13) Lawes, Melot, B.; Page, K.; Ederer, C.; Hayward, M. A.; Proffen, T.; Seshadri, R *Phys. Rev. B* **2006**, *74*, 024413.

(14) Dutta, D. P.; Manjanna' J.; Tyagi, A. K.; *J. Appl. Phys.* **2009**, *106*, 043915.

(15) Tung, L. D.; *Phys. Rev. B* **2006**, *73*, 024428.

(16) Tung, L. D., Lees, M. R.; Balakrishnan, G.; Paul, D. M. *Phys. Rev. B* **2007**, *75*, 104404.

(17) Rodriguez-Carvajal, J. *Physica B.* **1993**, *192*, 55.

(18) Quantum Design, Application 1070-207, Rev. A0, **2009**.

(19) Rao, T. V. C.; Raj, P.; Yusuf, S. M.; Rao, L. M.; Sathyamoorthy, A.; Sahni, V. C. *Phil. Mag. B* **1996**, *74*, 275.

(20) Singh, R. P.; Tomy, C. V.; *J. ,Condens. Matter.* **2008**, *20*, 235209.